Seismo-Tectonics of the Alborz Mountains from the analysis of local earthquake data

Sara Rezaei

Master of Science, Geodynamics

Department of Earth Science

University of Bergen

January 2015

Abstract

The Alborz range is part of the Alpine-Himalayan Orogenic belt, located in northern Iran, between the South Caspian block and the Central Iranian Block.

In this thesis I have chosen an area in Alborz range which has experienced a surprising earthquake (the Rudbar earthquake) that occurred on a fault that was not previously mapped. It could mean that there are other unidentified active faults in Alborz Mountains; therefore I did a comprehensive study of the earthquake activity in this area.

For this purpose I went to Iran and got the local seismic data from IIEES and did the following research:

- I identified the first P-waves and Sg-phases on my waveforms and I used four different velocity models to locate events in my data set, using single earthquake location method.
- I used the travel times of the phases to comparison of existing models and conclusion on crustal thickness. This comparison shows that the velocity model which represents the Moho at a depth of 58±2 km describes structures in the Alborz Mountains better compared to other velocity models.
- I also used the travel times of the phases to develop velocity models by improving the existing velocity model, using joint hypocenter and velocity model inversion method. In this thesis I improved the three initial models, but I could not introduce a new model that works better for this study area.
- I read amplitudes on vertical- and horizontal components and made vertical to horizontal comparison which shows horizontal components are 1.48 larger than amplitudes on vertical components on average. I used the amplitudes to compute magnitudes and develop a magnitude scale for the study area.
- I made the required observations (polarities and amplitude ratios) to determine mechanisms, using FOCMEC and HASH programs. I also used Moment tensor inversion as the third method for calculating the focal mechanisms where full waveforms were used.

I used all the above to get an understanding of tectonic setting in study area which represented a complicated tectonic activity in Alborz Mountains.

Acknowledgements

This master's thesis has been done at the Department of Earth Science, University of Bergen under guidance of Lars Ottemøller, Henk Keers and Mohammad Raeesi. It was a great pleasure to work under their consideration and I really appreciate their concern, comment and advice.

I would like to give special thanks to Lars Ottemøller and Henk Keers for all help, guidance and encouragement during the past two years.

I would also like to thank Mehdi Zare for helping me to get access to the data set for this master's thesis, the useful discussions and inviting me to interesting conferences in Tehran, Iran, about the seismic hazard in Tehran and the 2003 Bam earthquake.

I would also like to thank Zoya Zarifi for helping me to achieve fault map and topographic map for the study area.

I would also like to thank Mohammad Tatar, Alireza Ashari and Mostafa Ghasemi from IIEES for answering my questions.

I would also like to give special thanks to my family, especially Mom and Dad, for the continuous support and encouragement over the years and for allowing me to follow my dreams.

Finally I would like to thank my husband, Arad, for supporting me all the way like he always did. You have been very important for me when I have been writing my thesis.

January 2015

Sara Rezaei

Contents

1 Introduction

An earthquake occurs when a large amount of energy is released as the result of a sudden movement or rupture of a new or preexisting fault. It happens when tectonic stresses build up until that exceed the rocks strength [*Wolf*, 2002].

Accumulation and release of the energy on the fault can be explained by the elastic rebound theory. As rocks on each side of the fault move relative to each other, the friction along the fault or rock strength prevents any motion which leads to accumulation of energy. Once the accumulated energy exceeds the resistance force, a sudden movement occurs along the fault which releases energy. This process takes place irregularly but repeatedly on faults in the tectonic active areas [*Stein and Wysession*, 2009]. Part of the released energy converts to seismic waves. These waves propagate in all directions from the source (fault) through the Earth and can be recorded by seismographs. As seismic waves propagate, they carry some information from the source that generated them and the structure they have passed through. This information will be registered on seismograms as a convolution of the source, structure, and instrument signals in time domain; therefore we can gain knowledge about the tectonic processes causing earthquakes and Earth's structure by studying the seismograms [*Stein and Wysession*, 2009].

In this thesis I study seismograms for a set of local earthquakes that occurred in an area inside the Alborz Mountain range, Northern Iran, to get a picture of the tectonic processes and develop a new velocity model and magnitude scale.

The Alborz range is part of the Alpine-Himalayan Orogenic belt, located in northern Iran, between the South Caspian block and the Central Iranian Block [*Sodoudi et al.*, 2009]. Alborz range is full of folds and faults [*M Allen et al.*, 2003] which are a result of movement of the Central Iranian Block towards the South Caspian block and southwest movement of the South Caspian block relative to Iran [*Ritz et al.*, 2006].

Devastating and deadly earthquakes in history in the selected area [*Ambraseys and Melville*, 2005] confirm that the area is under deformation.

The Rudbar earthquake of 20 June 1990 with Mw =7.3 was one of those devastating earthquakes. It was a surprising earthquake that occurred on a fault that was not previously mapped and it is possible that there are other unidentified active faults in Alborz Mountains. In addition there is a high density of thrust and strike-slip faults in Alborz Mountains where movement along a fault can reactivate adjacent fault. [*Berberian and Walker*, 2010].

The importance of studying this area is that it includes the capital city of Iran, Tehran. It has a high population of 12 million inhabitants [*De Martini et al.*, 1998] and any strong earthquake around Tehran can cause a disaster in terms of loss of life and damage to infrastructure; therefore I do a comprehensive study of the earthquake activity in this area.

To do so, I needed to derive some information from seismograms:

- The arrival time of seismic waves: We use the arrival time of seismic waves at different seismometer to find the earthquake location. In this way, we can identify active faults that have been the source of earthquakes even if they cannot be observed on the surface [*Stein and Wysession*, 2009].

  There are various techniques to find the location of earthquakes. I used inversion for single earthquake location and joint hypocenter and velocity model inversion.

- Amplitude of the seismic waves: By measuring the amplitude of the seismic waves, we can say how strong earthquakes are in an area [*Stein and Wysession*, 2009]. I used the amplitude of the seismic waves to determine the magnitude of events and developed a local magnitude scale for study area using magnitude inversion technique.

- Geometry of faults: By geometry of fault we mean the direction of movement along the faults (slip angle) and the orientations of the fault planes (strike angle and dip angle). We use the amplitude and shape of seismic waves on the seismograms to find the geometry of faults. Knowledge about geometry of faults helps us to determine the direction of tectonic stresses in an area [*Stein and Wysession*, 2009]. To find geometry of faults I have used FOCMEC Program [*Snoke*, 2003], HASH Program [*Hardebeck and Shearer*, 2008] and Moment tensor inversion using Time-Domain Moment Tensor Inverse Code [*Dreger*, 2002].

Data for this thesis were obtained from the IIEES in Tehran where I visited for two weeks in early 2014. IIEES stands for International Institute of Earthquake Engineering and Seismology and was established in 1989 with the aim of reducing seismic risk in Iran. It therefore does research in all earthquake related fields in Iran such as assessing seismic hazard, assessing seismic risk and preventing earthquake disasters by e.g. designing building codes and retrofitting of weak buildings. Installation of seismic stations and recording of seismic waves in different parts of the country are also part of the IIEES tasks.

The data was processed using the SEISAN software [*Ottemöller et al.*, 2011] which I started to get to know in January 2014. The processing was done in a number of steps: Reading phases, locating events, developing a new velocity model, reading the amplitude of the waves, calculating the magnitude of events, making magnitude scale for Iran, determining the polarity of the first P-wave, making amplitude ratio and calculating the focal mechanisms. All processing steps were done by me.

2 Background

2.1 Tectonics of Iran

Iran is surrounded by the rigid South Caspian block in the north, the Turan shield in the northeast, Arabian plate in west–southwest and Helmand block in east (Figure 2-1) [*Sodoudi et al.*, 2009].

The tectonic setting of Iran is strongly influenced by the movement of Arabian plate towards Eurasia (North). As the Arabian plate moves to the north, Iran squeezes and deforms between adjacent lithospheric plates/blocks which leads to crustal shortening and thickening and mountain building in Iran [*Sodoudi et al.*, 2009].

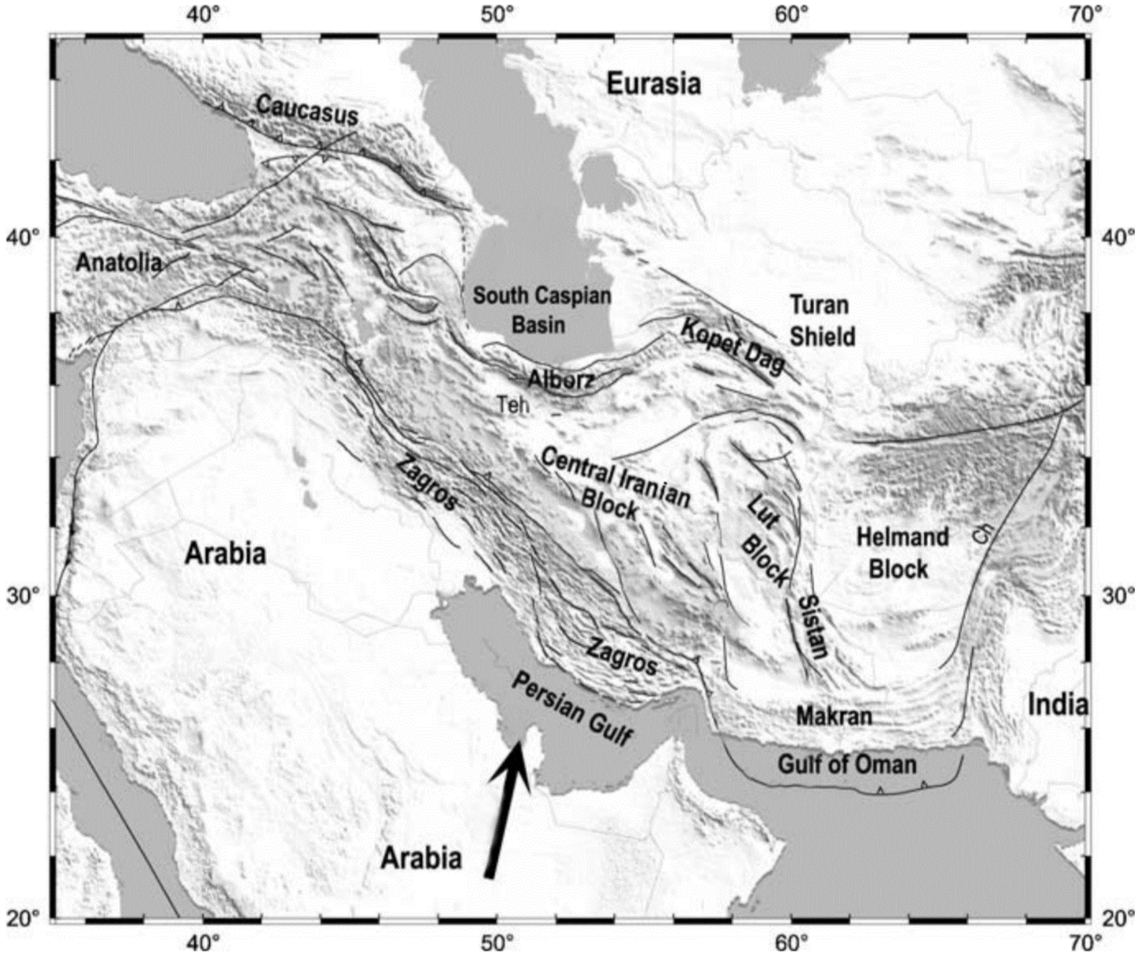

Figure 2-1: Tectonic map of Iran modified from Vernant et al., 2004b. The black arrow shows the direction of the Arabian-Eurasia convergence.

The rate of Arabian-Eurasia convergence is about 16-22 mm/yr. (Figure 2-2) which gives a total continental shortening of about 150 km in Iran. 57-87 km of this is placed in the Zagros Mountains, about 75 km is placed in Kopet Dag Mountains and 30 km is placed in the Alborz Mountains [*Guest et al.*, 2006].

Deformation and shortening along these mountains is confirmed by local topography and concentration of seismic activities [*Vernant et al.*, 2004b].

The Alborz and Kopet Dag Mountains are located in the north and northeast of Iran, respectively. Formation of these mountains is because the Helmand block acts as a barrier to eastward deformation; therefore two rigid blocks, the Central Iranian block and Lut block, transfer deformation from southwest to the north and northeast of Iran, respectively [*Vernant et al.*, 2004a; *Vernant et al.*, 2004b]

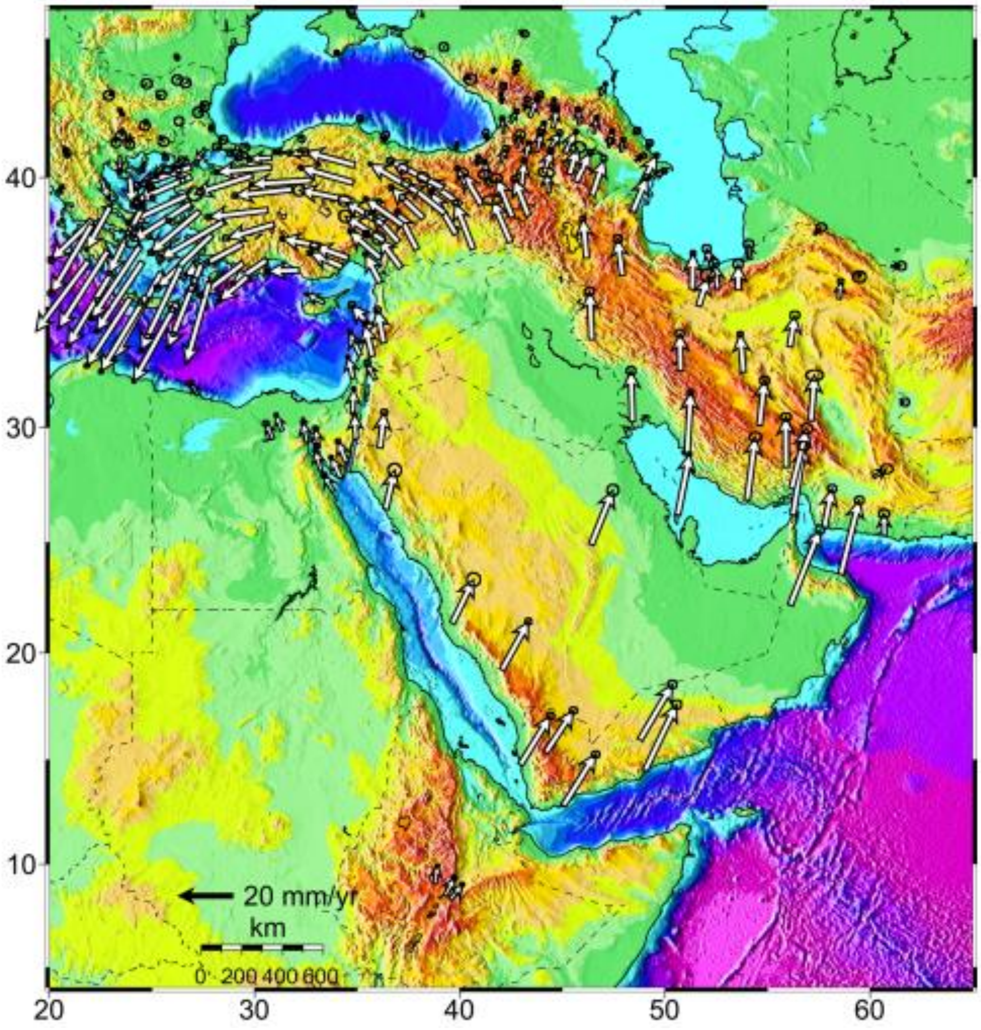

Figure 2-2: GPS velocity vectors and error ellipses relative to Eurasia [Reilinger et al., 2006]

2.2 Tectonic of Alborz Mountains, northern Iran

The Alborz mountain range is 100 km wide and 3000 m high and located in northern Iran [*Vernant et al.*, 2004a]. Several surveys denote these mountains are isostatically unbalanced as with the relatively high topography they are missing a crustal root (Sodoudi, Yuan et al. 2009, Radjaee, Rham et al. 2010).

The Alborz is a narrow seismically active range between two rigid aseismic blocks, the South Caspian block and the Central Iranian Block [*Radjaee et al.*, 2010; *Sodoudi et al.*, 2009; *Vernant et al.*, 2004b]. Structures of the Alborz Mountains are controlled by the movement of these two blocks.

Northward movement of the Central Iranian Block leads to a North–South shortening at 5 ± 2 mm/ yr. in Alborz area. This movement began in the Miocene (23.03 Ma year ago) [*Vernant et al.*, 2004a].

In the Pliocene (3-5 Ma), the South Caspian block started to move to the southwest relative to Iran at a rate of 13-17 mm/ yr. [*Jackson et al.*, 2002] which causes an East-West motion at a rate of 4 ± 2 mm/ yr. inside the range [*Vernant et al.*, 2004a].

Combination of N-S shortening and E-W motion in the Alborz mountains led to form a transpressional (oblique shortening) regime along the range where shortening occurs by thrusting and range-parallel left-lateral strike-slip faulting [*M B Allen et al.*, 2003; *Vernant et al.*, 2004a].

2.3 The Rudbar earthquake

The Rudbar earthquake of 20 June 1990 with Mw =7.3 and Ms= 7.7 was the largest earthquake that has occurred in Alborz Mountains during the instrumental period. This earthquake occurred on the Rudbar fault which was previously unknown [*Berberian and Walker*, 2010].

The Rudbar fault is a range-parallel left-lateral strike slip with a length of ~80 km. It consists of three discontinuous segments (Baklor-, Kabateh - and Zardgeli segments), (Figure 2-3). These three segments are arranged in a right-stepping en-echelon pattern [*Berberian and Walker*, 2010].

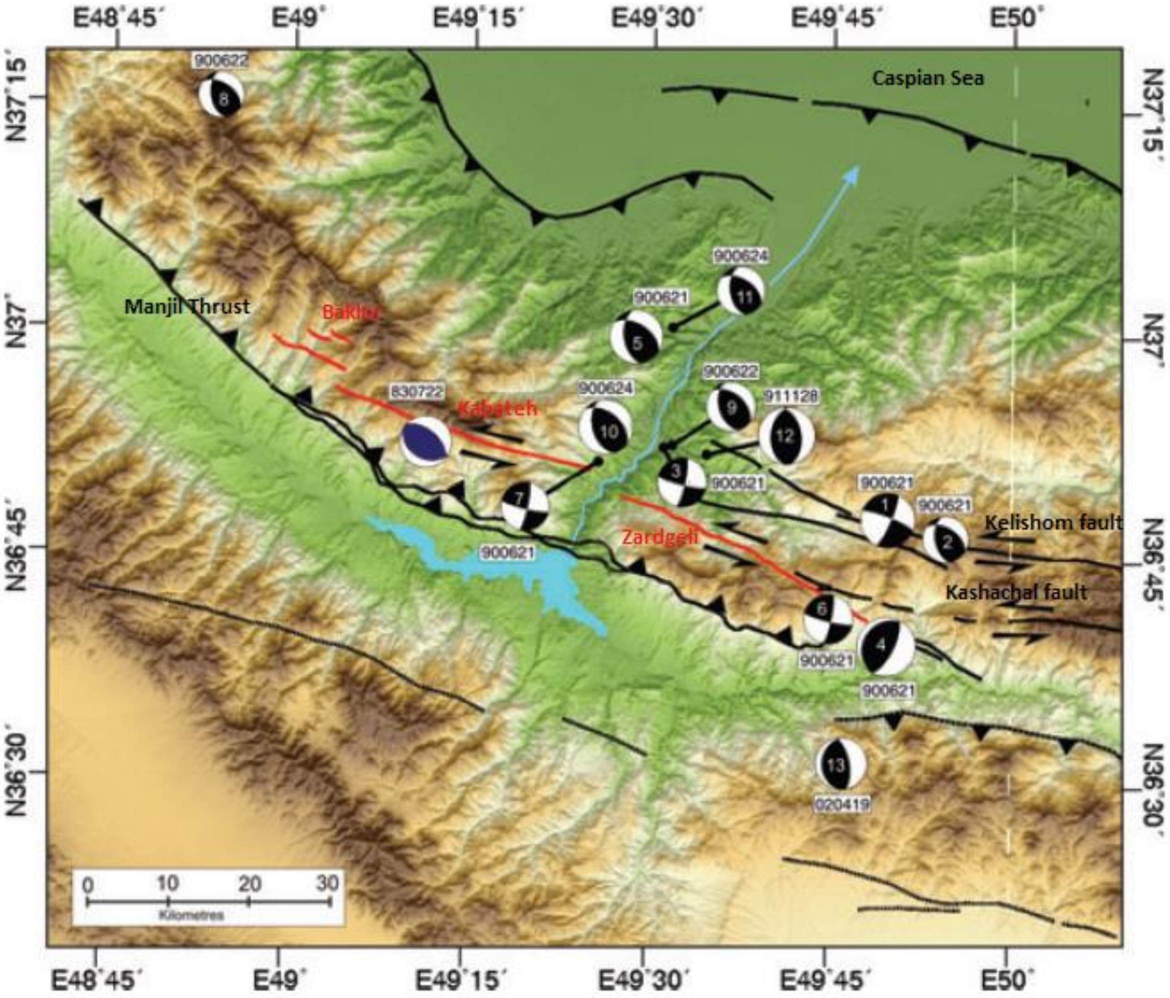

Figure 2-3: The Rudbar fault is a range-parallel left-lateral strike slip with a length of ~80 km. It consists of Baklor-, Kabateh - and Zardgeli segments. Focal mechanism of the 1983 Charazeh earthquake (blue) and focal mechanisms of the 1990 Rudbar aftershocks (black) are also shown (Modified from Berberian and Walker, 2010).

The Rudbar earthquake of 20 June 1990 was followed by a number of aftershocks with a mixture of thrust and left-lateral strike slip mechanisms (Figure 2-3). Most of the aftershocks have occurred in the unbroken part of Rudbar fault, located between the Kabateh and Zardgeli segments where there was a positive Coulomb stress change after the mainshock (Figure 2-4) [*Sarkarinejad and Ansari*, 2014].

The 1990 Rudbar mainshock has caused an increasing of Coulomb stress on parts of the adjacent faults such as Kelishom and Kashachal left-lateral strike-slip faults and Manjil Thrust (Figure 2-4)[*Sarkarinejad and Ansari*, 2014].

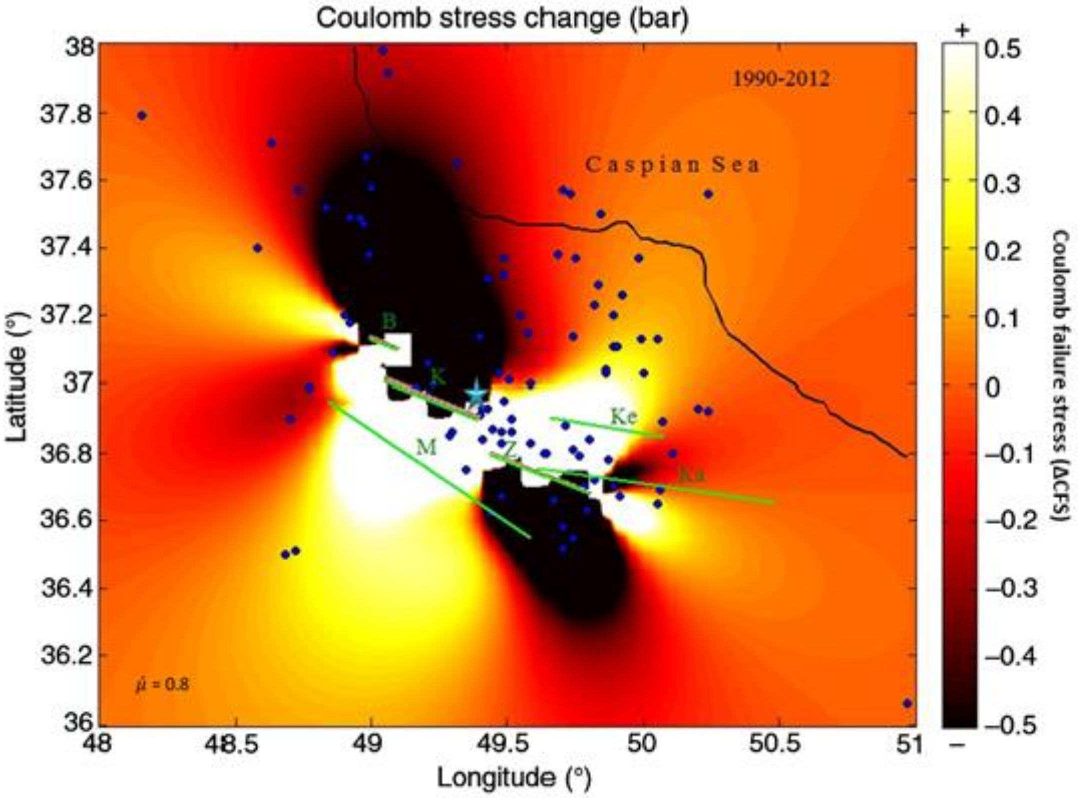

Figure 2-4: Coulomb stress distribution after the 1990 Rudbar mainshock (the blue star). The positive Coulomb failure stress shows the area which brought closer to failure. Blue dots are showing earthquake distribution. B=Baklor, K=Kabateh, Z=Zardgeli, M=Manjil thrust, Ke=Kelishom and Ka=Kashachal [Sarkarinejad and Ansari, 2014].

Kelishom and Kashachal faults are two active faults in the Rudbar region which show 0.4 -1.5 km and 150-200 m left-lateral displacement, respectively. Therefore they can be considered as potential eastward continuation of the Rudbar fault [*Berberian and Walker*, 2010].

3 Earthquake Data

In this thesis I used data from 409 local earthquakes recorded between 2004 and 2013. I took waveform data and reprocessed everything completely; but I also had routine locations for comparison. The data are located in the area as outlined in Figure 3-1 and Figure 3-2 with latitude range 35.5°-37° and longitude range 48°-52°. As shown in Figure 3-1 the data set included few earthquakes outside of my study area, but because of they were close to my study area and there were a few of them I kept them in my data set.

Data are taken from IIEES in Tehran. The number of installed stations by IIEES has increased from 2004 to 2012; therefore the amount of data has also increased. For this study a total of 27 3-component stations were used (Table 3-1).

I should mention also I could not obtain a copy of continuous data to search for additional events.

As shown in Figure 3-1 the stations are spread throughout Iran. I mostly used the stations that are close to the study area and ignored more distant recordings as they would not help much for the purpose of this study.

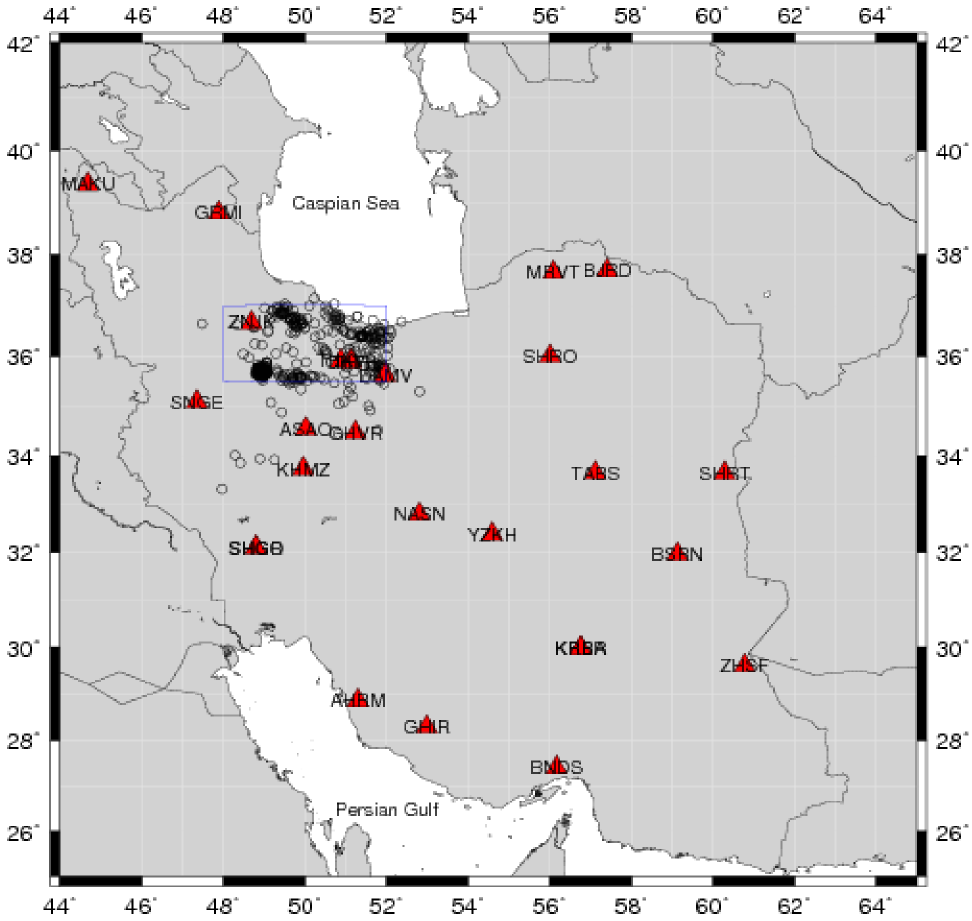

Figure 3-1: It is showing the study area, locations of events (Circles) and stations (Triangles).

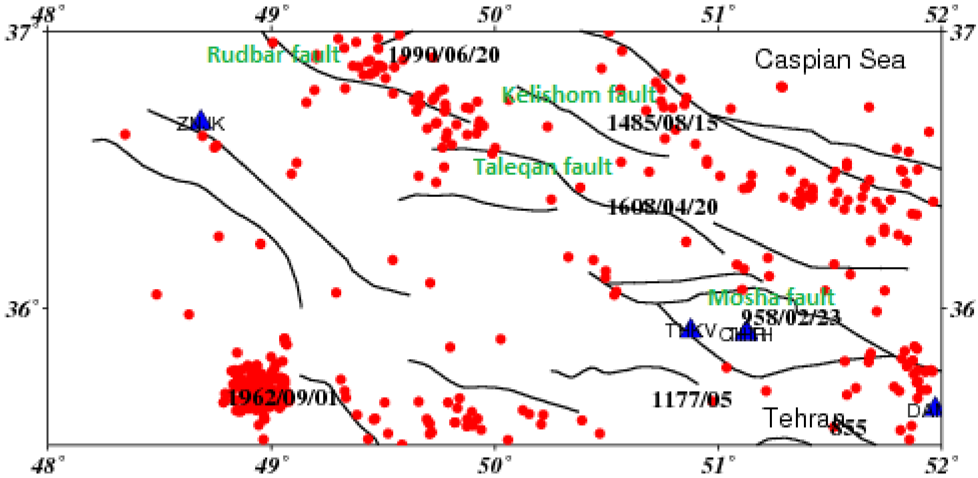

Figure 3-2: The study area, locations of events (Circles) and stations (Triangles). The large earthquakes in the course of history are also shown [Ambraseys and Melville, 2005]. Faults are from "Geological survey of Iran database" and labeled by me, using Berberian and Walker, 2010.

Figure 3-3 shows the number of recorded events with time. Figure 3-4 shows number of recorded events as a function of magnitude. Figure 3-5 and Figure 3-6 show magnitude and depth distribution of events as a function of time, respectively. Figure 3-4 and Figure 3-5 are the results of the magnitude estimation of these events in section 5, using the Hutton and Boore (1987) scale. Figure 3-1 and Figure 3-6 are the results of locating the events in section 4, using IIEES velocity model.

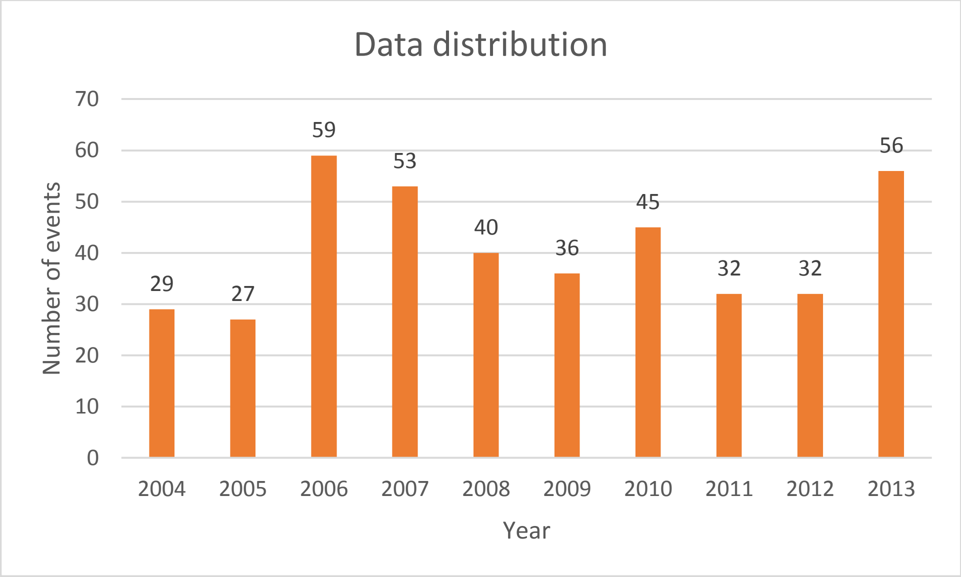

Figure 3-3: Number of recorded events in each year

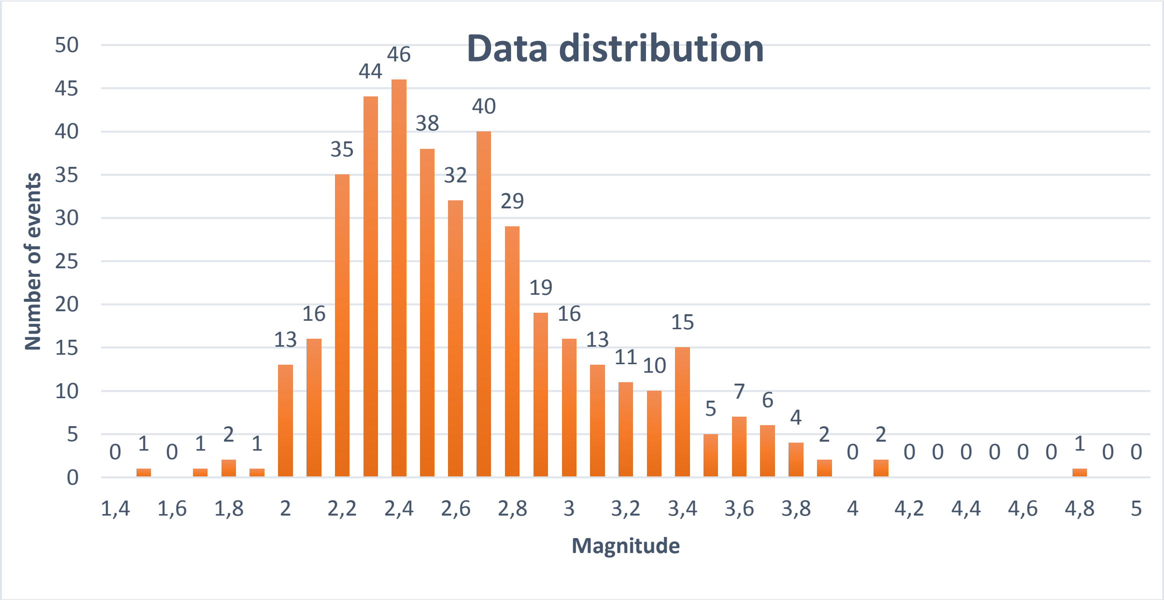

Figure 3-4: Number of recorded events as a function of magnitude.

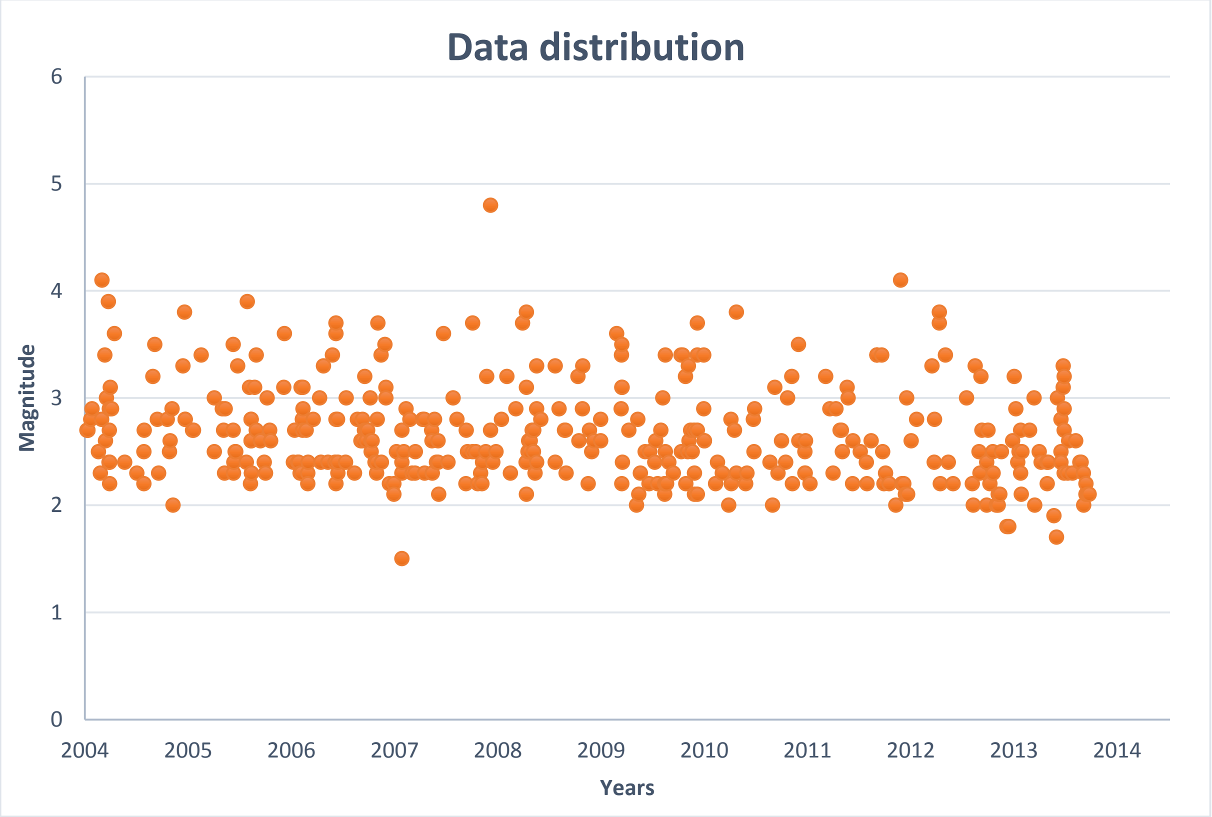

Figure 3-5: Magnitude distribution as a function of time.

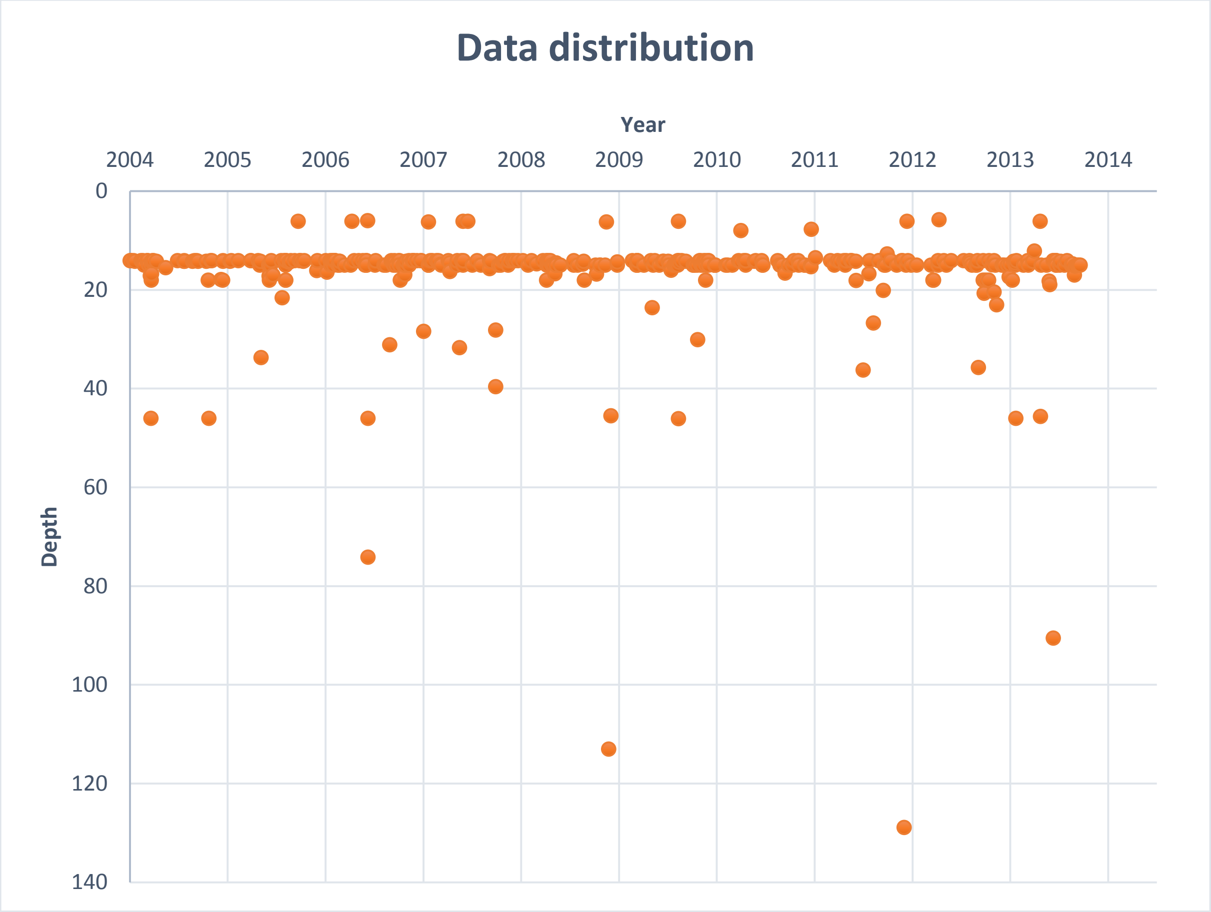

Figure 3-6: Depth distribution as a function of time.

Number	**Station code**	**Latitude °N**	**Longitude °E**	**Elevation m**	**Digitizer S/N**	**Start Time**
1	NASN	32°47.95′N	52°48.50′E	2800	DB10	12.04.2004
2	DAMV	35°37.81′N	51°58.25′E	2300	DB20	02.06.2004
3	GRMI	38°48.59′N	47°53.63′E	1300	DB16	10.09.2004
4	GHIR	28°17.13′N	52°59.20′E	1200	DB19	12.05.2004
5	BNDS	27°23.96′N	56°10.28′E	1500	DB06	11.05.2004
6	MAKU	39°21.29′N	44°41.00′E	1730	DB01	14.04.2004
7	ZHSF	29°36.66′N	60°46.52′E	1575	DB02	17.05.2004
8	ASAO	34°32.88′N	50°01.52′E	2217	DB05	10.05.2004
9	THKV	35°54.94′N	50°52.73′E	1795	DB09	22.05.2004
10	THR	35°54.48′N	51°07.56′E	2250		
11	CHTH	35°54.48′N	51°07.56′E	2250	DB04	03.10.2005
12	SNGE	35°05.55′N	47°20.82′E	1940	DB18	26.05.2004
13	SHGR	32°06.50′N	48°48.08′E	150	DB17	11.10.2002
14	SHGO	32°06.50′N	48°48.08′E	150		
15	KRBR	29°58.93′N	56°45.63′E	2576	DB14	23.08.2004
16	KRBA	29°58.93′N	56°45.63′E	2576		
17	MRVT	37°39.56′N	56°05.36′E	870	DB11	
18	GHVR	34°28.80′N	51°14.72′E	927	DE61	15.02.2007
19	ZNJK	36°40.25′N	48°41.11′E	2200	DB06	11.09.2007
20	BJRD	37°41.98′N	57°24.49′E	1337	DB11	06.02.2008
21	TABS	33°38.94′N	57°07.14′E	1106	DB05	10.09.2008
22	SHRT	33°38.77′N	60°17.46′E	837	DB01	11.09.2008
23	KHMZ	33°44.38′N	49°57.85′E	1985	DE48	12.01.2009
24	SHRO	36°00.51′N	56°00.78′E	1264	DE67	04.02.2009
25	AHRM	28°51.93′N	51°17.83′E	90	A1986	04.06.2010
26	YZKH	32°23.41′N	54°35.50′E	2226	A1983	10.07.2012
27	BSRN	15°7.90′N	59°07.55′E	1416	DB14	09.10.2012

Table 3-1: Information about seismic stations.

4 Location of events

By locating an earthquake we will find the origin time and the coordinates of earthquake. To do this we use the observed and the theoretical arrival times of seismic phases at different stations [*Stein and Wysession*, 2009].

The observed arrival time of each phase is determined by identifying and reading the phase from seismograms.

The theoretical arrival times can be found by using the 1D velocity model, ray tracing from a trial earthquake location and calculating the travel times of phases [*Kissling*, 1988].

There are various techniques to find the location of an earthquake [*Havskov and Ottemoller*, 2010]. In this thesis I used:

1) Inversion for single earthquake location
2) Joint hypocenter and velocity model inversion

Joint hypocenter and velocity model inversion provide a new velocity models by improving the existing velocity model as it locate a set of data with smaller errors .

I also attempted to use the double difference earthquake location method as it can provide better relative locations, but did not have enough data for this method. A brief description of the double difference earthquake location is given in section 4.5.

I used four different velocity models to calculate travel times of seismic phases. As I located the events, I also decided which one of the velocity models works better.

4.1 Phase reading

A seismogram consists of many seismic phases. The phases represent the paths that seismic waves have taken before they reach the station. In order to locate an event one needs to identify some of them on at least three seismic stations [*Havskov and Ottemoller*, 2010].

For local events, it is common to read Pg-, Sg-, Pn- and Sn-phases (Figure 4-1). They stand respectively for direct P-, direct S-, critically refracted P- and critically refracted S-waves along the Moho [*Havskov and Ottemoller*, 2010].

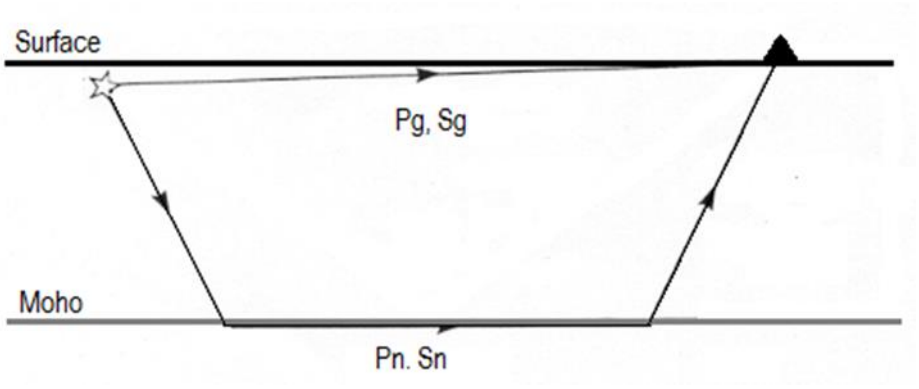

Figure 4-1: A simplified model for the Pg-, Sg-, Pn- and Sn-phases modified from Havskov and Ottemoller 2010.

I have done the first P-phase and Sg-phase reading for all 409 events (Table 4-1). The first P phase is either Pn or Pg depending on the cross-over distance, where the Pg-phase and the Pn-phase arrive simultaneously (Section 5.2.2). At larger distances Pn arrives before Pg. The first P-phase should be labeled as P-phase in the SEISAN for simplicity's sake and the location program decides whether it is Pg or Pn depending on the distance. It is usually done the same for the first S-phase, but I could not see the Sn-phases on my seismograms (Figure 4-2) and all S readings are made for Sg and labeled as such. This observation is consistent with IIEES observations (IIEES, personal communication, 2014).

For phase reading, filters were applied when needed, but most the readings were done on the raw data. The use of different filters is justified because the difference in phase response of the filters is not significant. The first P-phase was labeled on the vertical components of the station and Sg- phases labeled on one of the horizontal components (Figure 4-2). This is done because P-and S-phases are strongest on these components, respectively. In addition, S-P conversion close to the station can be misidentified as S on the vertical component. To avoid this mistake Sg was identified on the horizontal component and not on the vertical component.

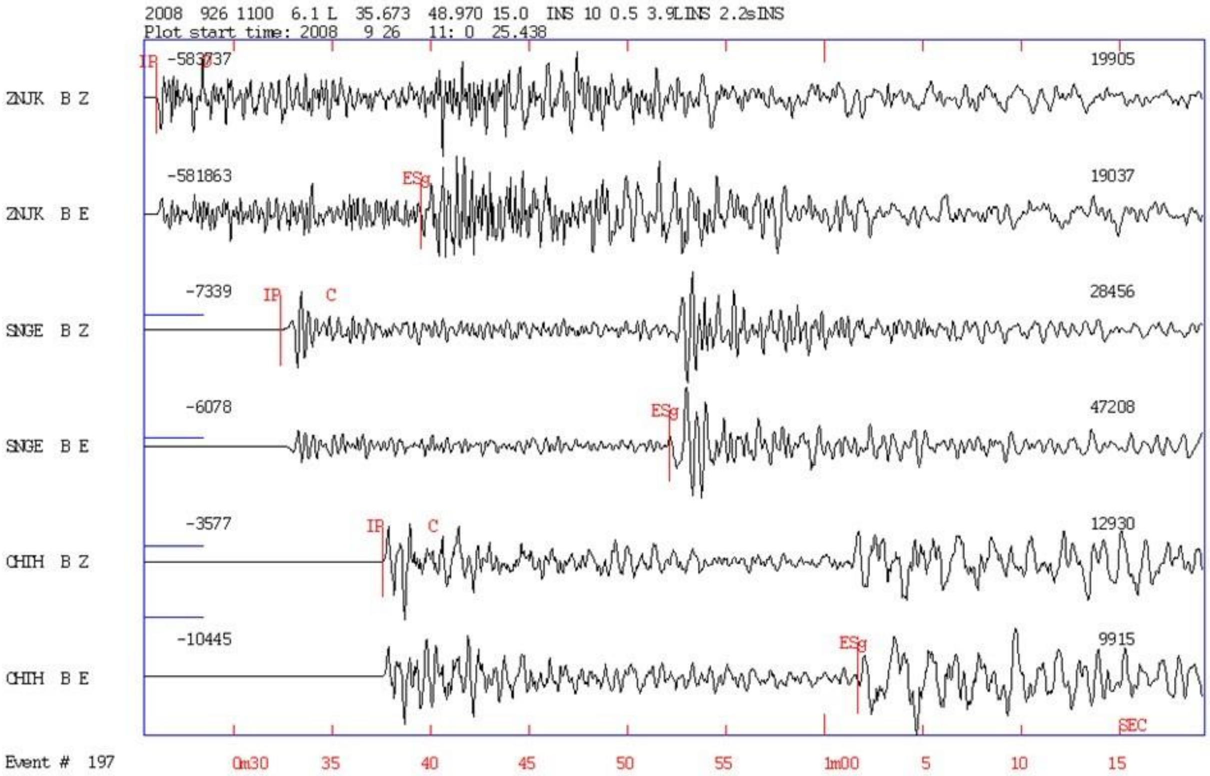

Figure 4-2: The waveforms of an event recorded by three seismic stations located at three different distances from the source. ZNJK, SNGE and CHIH are the stations codes. The vertical component (BZ) and a horizontal component (BE) are taken from each station. IP shows arrival times of the first P-phase and ESg shows arrival times of direct S-waves. The ZNJK-station is closer to the earthquake source relative to the SNGE- station and the CHIH- station; therefore the ZNJK-record contains more high-frequency signals, the P-wave reaches the station in a shorter time and there is less difference in arrival time of the P and S, in comparison to two other stations.

No.	Station code	No. P	No. Sg
1	NASN	19	17
2	DAMV	263	273
3	GRMI	79	67
4	GHIR	2	
5	BNDS	1	
6	MAKU	6	2
7	ZHSF	1	
8	ASAO	287	296
9	THKV	258	241
10	THR	2	2
11	CHTH	325	307
12	SNGE	176	169
13	SHGR	4	3
14	SHGO		1
15	KRBR	1	
16	MRVT	8	
17	GHVR	127	126
18	ZNJK	199	183
19	BJRD	1	
20	TABS	8	
21	SHRT	1	
22	KHMZ	59	72
23	SHRO	4	1
24	CHBR	1	
	Sum	1832	1760

Table 4-1: Number of read P-and Sg-phases of each station.

4.2 Calculating the travel times of phases

4.2.1 Theory

In a layered 1D velocity model the layers are parallel and uniform. In such a model the ratio of the sine of the incident angle and corresponding velocity remains constant at all the interfaces while a phase travels through them, so

$$\frac{\sin\ (i)}{v} = constant = p. \quad \textit{Equation 4-1}$$

This ratio is called the ray parameter, p. Each phase has a specific ray parameter; hence it is used to find the path of the phase.

If we know the path of the phases then we can compute the travel times (T) between source (i) and station (k) [*Um and Thurber*, 1987]

$$T_{travel} = \int_i^k \frac{1}{v}\, ds \qquad \textit{Equation 4-2}$$

Where v is the velocity field and ds is the parameter of path length.

The relationship between the arrival time, the origin time (τ) and the travel time is [*Waldhauser and Ellsworth*, 2000]

$$T_{arrival} = \tau^i + \int_i^k \frac{1}{v}\, ds \qquad \textit{Equation 4-3}$$

4.2.2 1D velocity models

I used four different velocity models to calculate travel times of seismic phases. In these velocity models crust divided into different number of layers. They represent different depth of the Moho and the velocity of P wave is also slightly different at the Moho. I tried to use my local data to see which one of them works better, consequently, which one of them represent the correct Moho depth in this area.

The first velocity model was provided by IIEES (Table 4-2, Figure 4-3). It is an average unpublished velocity model for the whole of Iran (M. Tatar, personal communication, 2014). In this model, the crust consists of four layers and there is a significant increase in seismic velocity from 6.5 km/s to 8.05 km/s at the depth of 46 km, which shows the depth of the Moho.

The second velocity model is obtained from Abbassi et al., 2010. This is a velocity model for an area inside the Central Alborz Mountains. In this model the crust consists of five layers, where the top two layers are sedimentary layers with a thickness of 3 km and 4 km. They suggest that the Moho is at a depth of 58±2 km (Table 4-3, Figure 4-4). This model is the result of joint inversion of receiver functions, inversion of local events and measurements of Rayleigh wave group velocity.

The third velocity model is taken from Ashtari et al., 2005. Ashtari et al., 2005 used this model to study the microseismic activities in Tehran region (Central Alborz Mountains). In this model, the crust consists of four layers and Moho is at a depth of 35 km (Table 4-4, Figure 4-5).

The fourth model is the result of analysis of teleseismic P-waveform receiver functions for the Tehran region (Central Alborz Mountains) [*Doloei and Roberts*, 2003]. In this model the crust consists of three main layers where seismic velocity gradually increases in each layer and Moho is at a depth of 46±2 km. To use this model in SEISAN, I used an approximation of velocity gradients by dividing each layer in several layers. The first and third layers are divided into five layers and the second layer is divided into three layers (Table 4-5, Figure 4-6).

1D Velocity Model 1 (IIEES):

Depth (km)	Velocity (km/s)
0.0	5.4
6.0	5.9
14.0	6.3
18.0	6.5
46.0 M	8.05
80.0	8.1

Table 4-2: 1D velocity model 1 (IIEES).M=Moho.

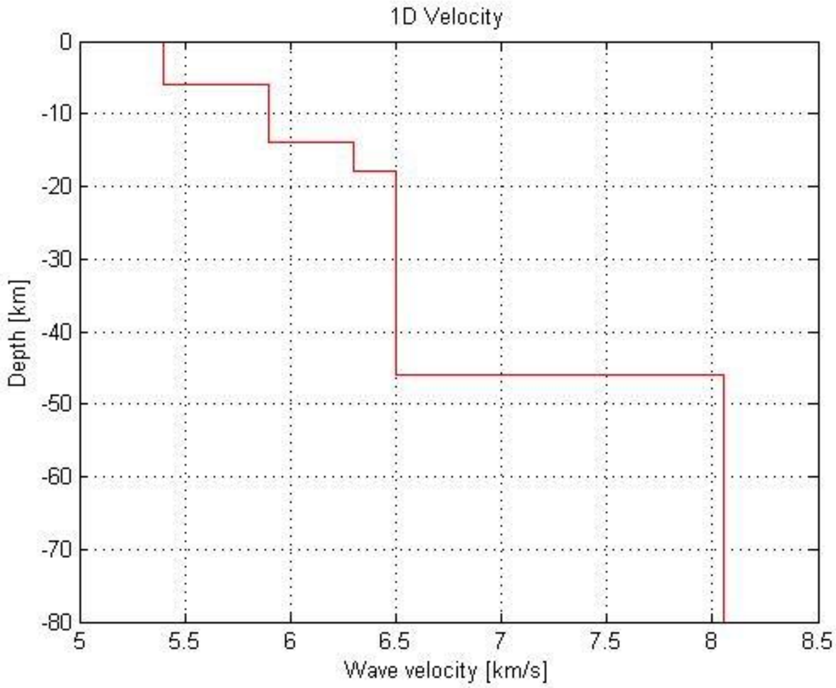

Figure 4-3: 1D velocity model 1 (IIEES). The crust consists of four layers and Moho is at a depth of 46 km.

1D Velocity Model 2 [*Abbassi et al.*, 2010]:

Depth (km)	**P-Velocity (km/s)**
0.0	5.4
3.0	5.8
7.0	6.1
16.0	6.25
24.0	6.40
58.0 M	8.1

Table 4-3: 1D velocity model 2 [Abbassi et al., 2010]. M=Moho.

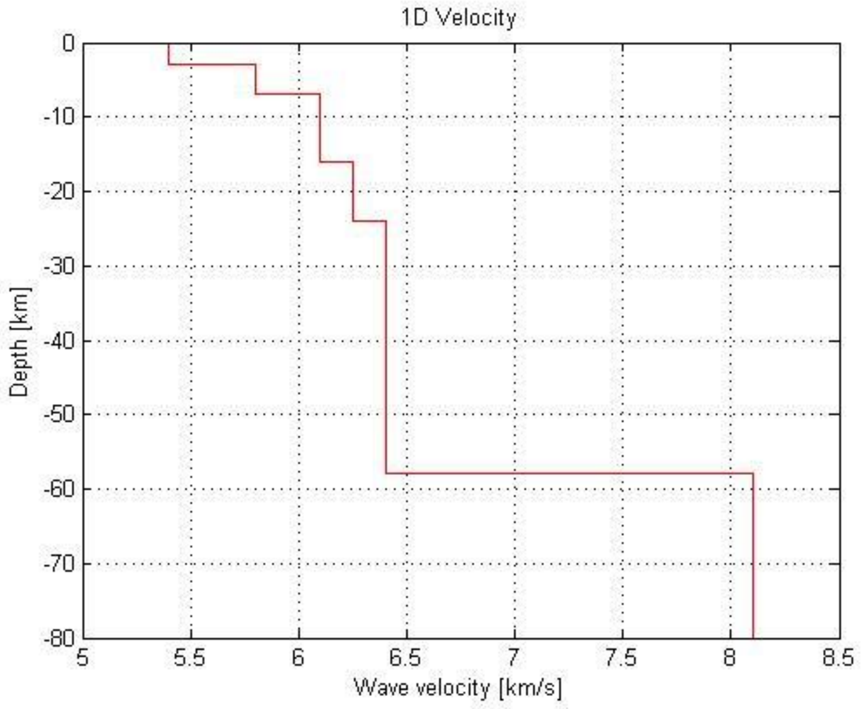

Figure 4-4: 1D velocity model 2 [Abbassi et al., 2010]. The crust consists of five layers, where the top two layers are sedimentary layers. Moho is at a depth of 58±2 km.

1D Velocity Model 3 [*Ashtari et al.*, 2005]:

Depth (km)	**P-Velocity (km/s)**
0.0	5.4
2.0	5.7
8.0	6.0
12.0	6.3
35.0 M	8.0

Table 4-4: 1D velocity model 3[Ashtari et al., 2005]. M=Moho.

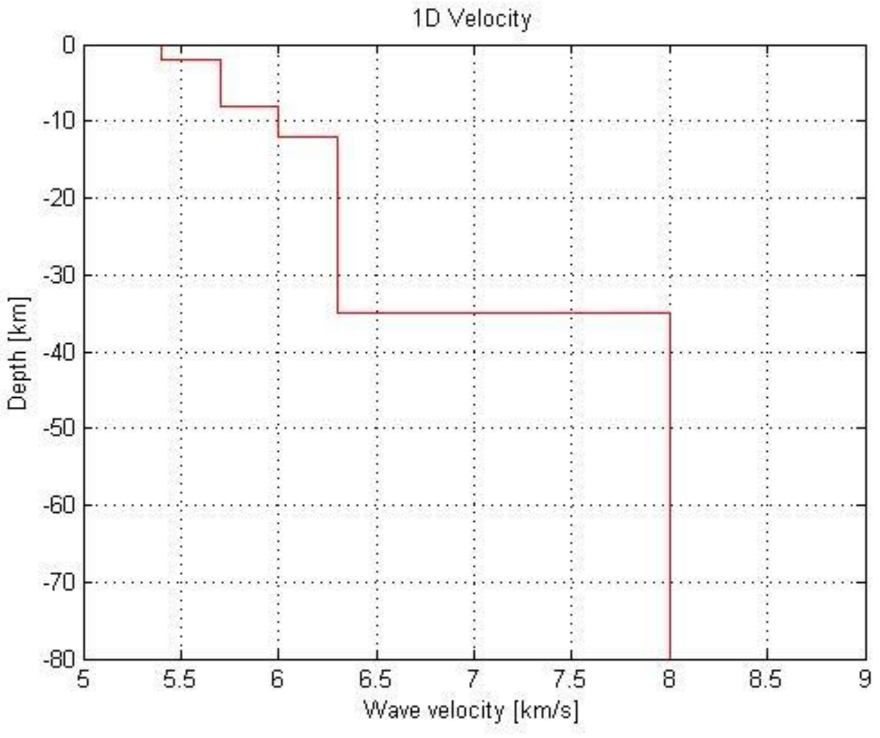

Figure 4-51D velocity model 3[Ashtari et al., 2005]. The crust consists of four layers and Moho is at a depth of 35 km.

1D Velocity Model 4 [*Doloei and Roberts*, 2003]:

Depth (km)	**P-Velocity (km/s)**	**The three main layers (Doloei and Roberts 2003)**
0,00	4,00	The first layer
2,80	4,36	
5,60	4,72	
8,40	5,08	
11,20	5,44	
14,00	5,80	
19,33	6,00	The second layer
24,66	6,20	
30,00	6,40	
33,20	6,62	The third layer
36,40	6,84	
39,60	7,06	
42,80	7,28	
46,00 M	7,50	

Table 4-5: An approximation of 1D velocity model suggested by Doloei and Roberts 2003. M=Moho.

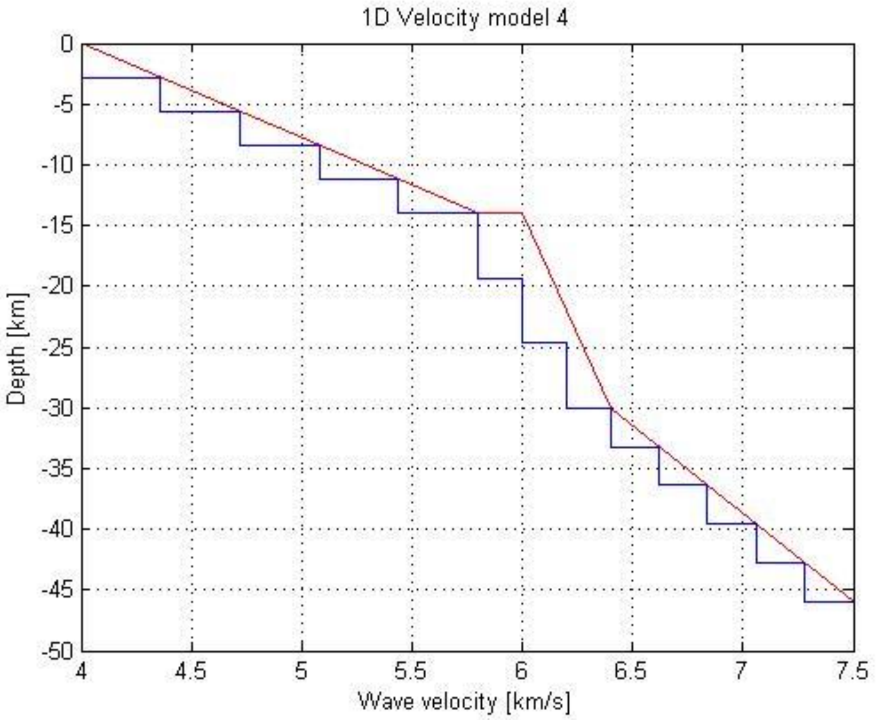

Figure 4-6: The red color shows the velocity model suggested by Doloei and Roberts 2003 and the blue color is an approximation of velocity gradients by dividing each layer in several layers. The first and third layers are divided into five layers and the second layer is divided into three layers.

4.2.3 The time-distance diagrams

Travel times for an event (15.06.2008) are calculated with the four different velocity models to show how the cross-over distance and calculated travel times of direct and critically refracted phases will vary depending on the velocity model. This calculation is done by the TTLAYER program [*Ottemöller et al.*, 2011].

In Figure 4-7, 1D velocity model 1 (IIEES) is used to calculate the travel times. Cross-over distance is ~ 104 km from the source. Up to ~ 140 km, travel times for direct and reflected waves are pretty close. In the 4 traces between 105 and 195 km I can see that Sn and Sg are not far apart and I identified them as Sg-phases.

Figure 4-8 shows calculated travel times using model 2. Cross-over distance is ~ 130 km. The direct and refracted waves are identified almost identical until ~ 270 km. S-phases are shown where I have identified Sg-phases.

Time-distance diagram using model 3 is shown in Figure 4-9. This velocity model represents the lowest Moho depth (35 km) for this area and it calculates shorter cross-over distance (~ 73 km). Up to ~ 145 km, travel times for direct and reflected waves are close. After this distance Sn-phases identified as they arrive in a shorter time.

As Figure 4-10 shows, time-distance diagram using model 4 is not even close to other calculated time-distance diagrams.

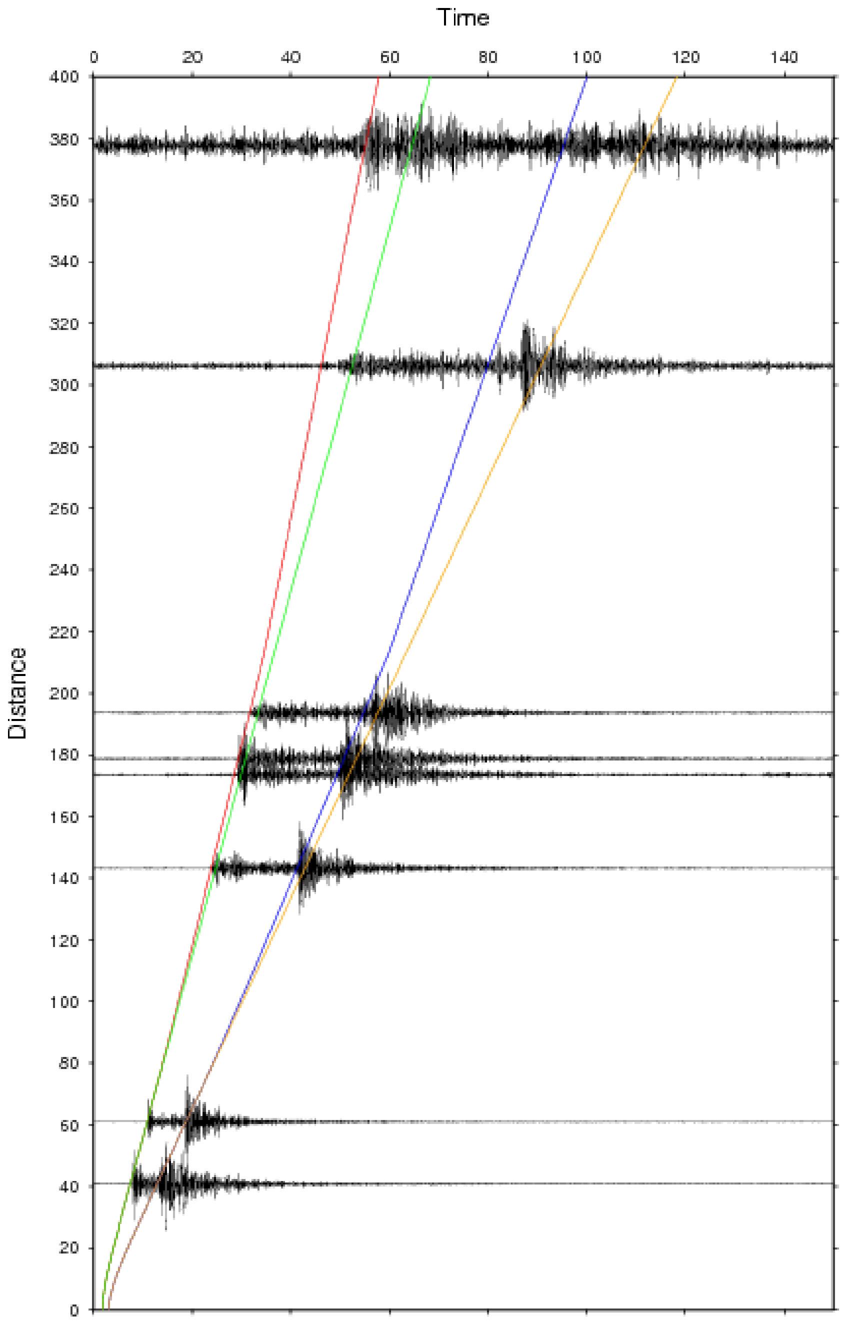

Figure 4-7: Time-distance diagram: 1D Velocity Model 1 (IIEES) is used to calculate the travel times. The green color = direct P-wave (Pg), the orange color = direct S-wave (Sg), the red color = refracted P-waves (Pn) and the blue color = refracted S-waves (Sn). Cross-over distance is ~ 104 km from the source.

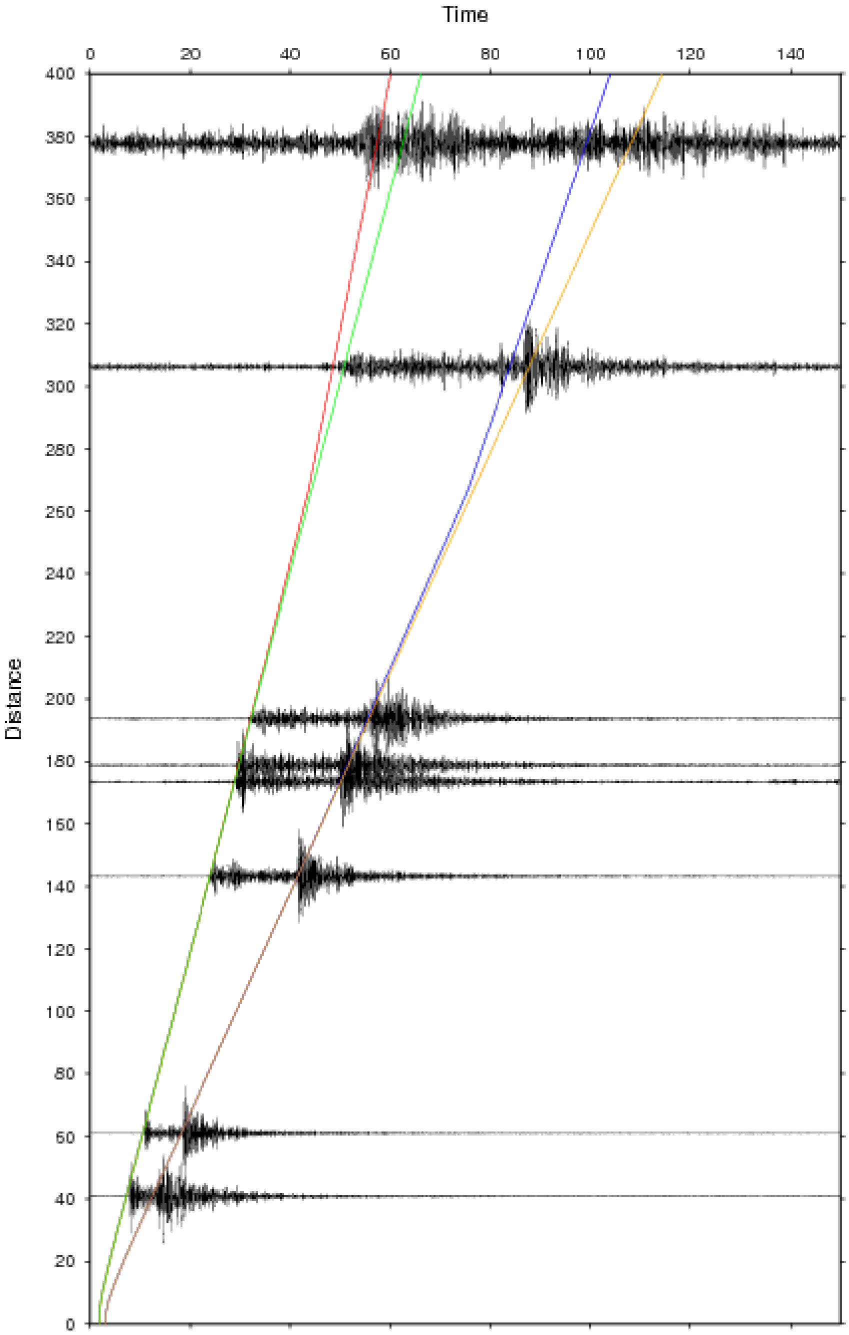

Figure 4-8: Time-distance diagram: 1D Velocity Model 2 [Abbassi et al., 2010]is used to calculate the travel times. The green color = direct P-wave (Pg), the orange color = direct S-wave (Sg), the red color = refracted P-waves (Pn) and the blue color = refracted S-waves (Sn). Cross-over distance is ~ 130 km from the source.

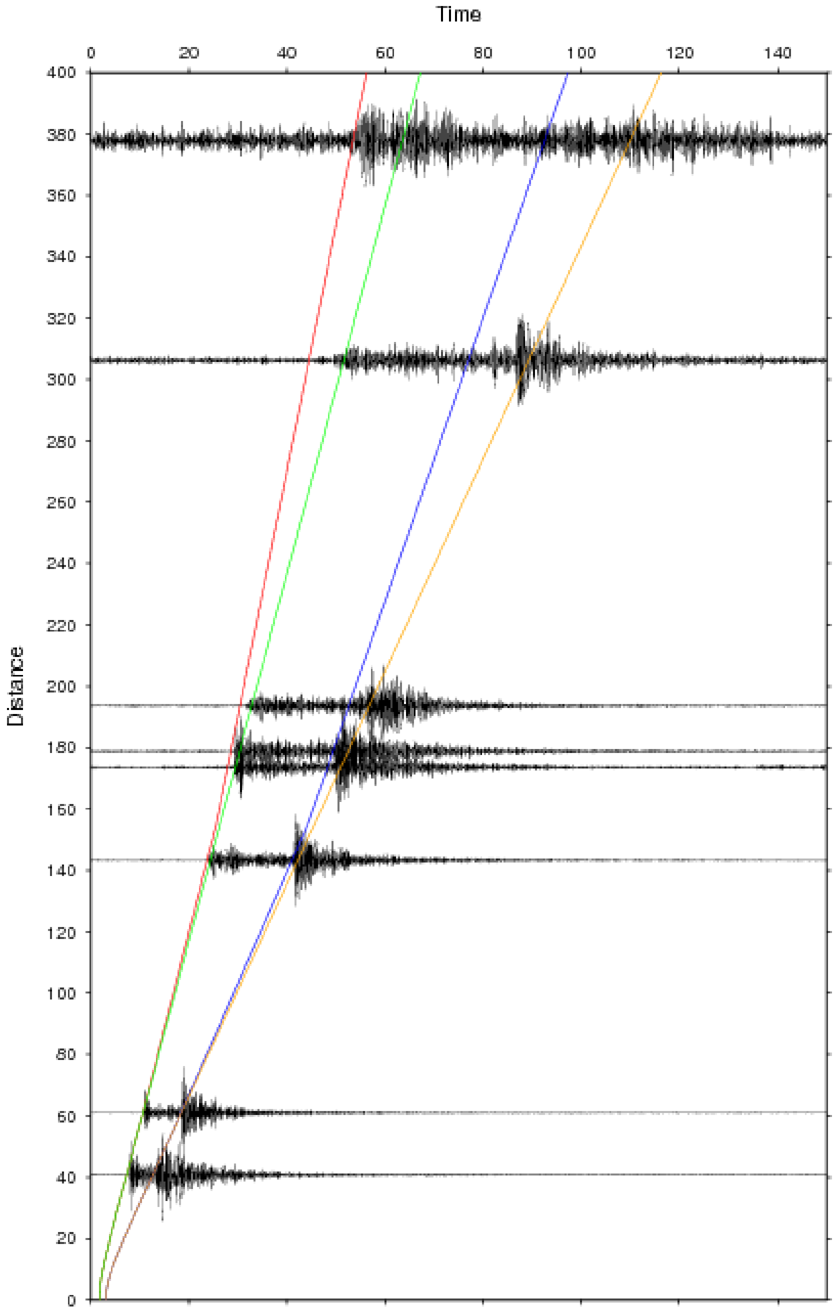

Figure 4-9: Time-distance diagram: 1D Velocity Model 3 [Ashtari et al., 2005] is used to calculate the travel times. The green color = direct P-wave (Pg), the orange color = direct S-wave (Sg), the red color = refracted P-waves (Pn) and the blue color = refracted S-waves (Sn). Cross-over distance is ~ 73 km from the source.

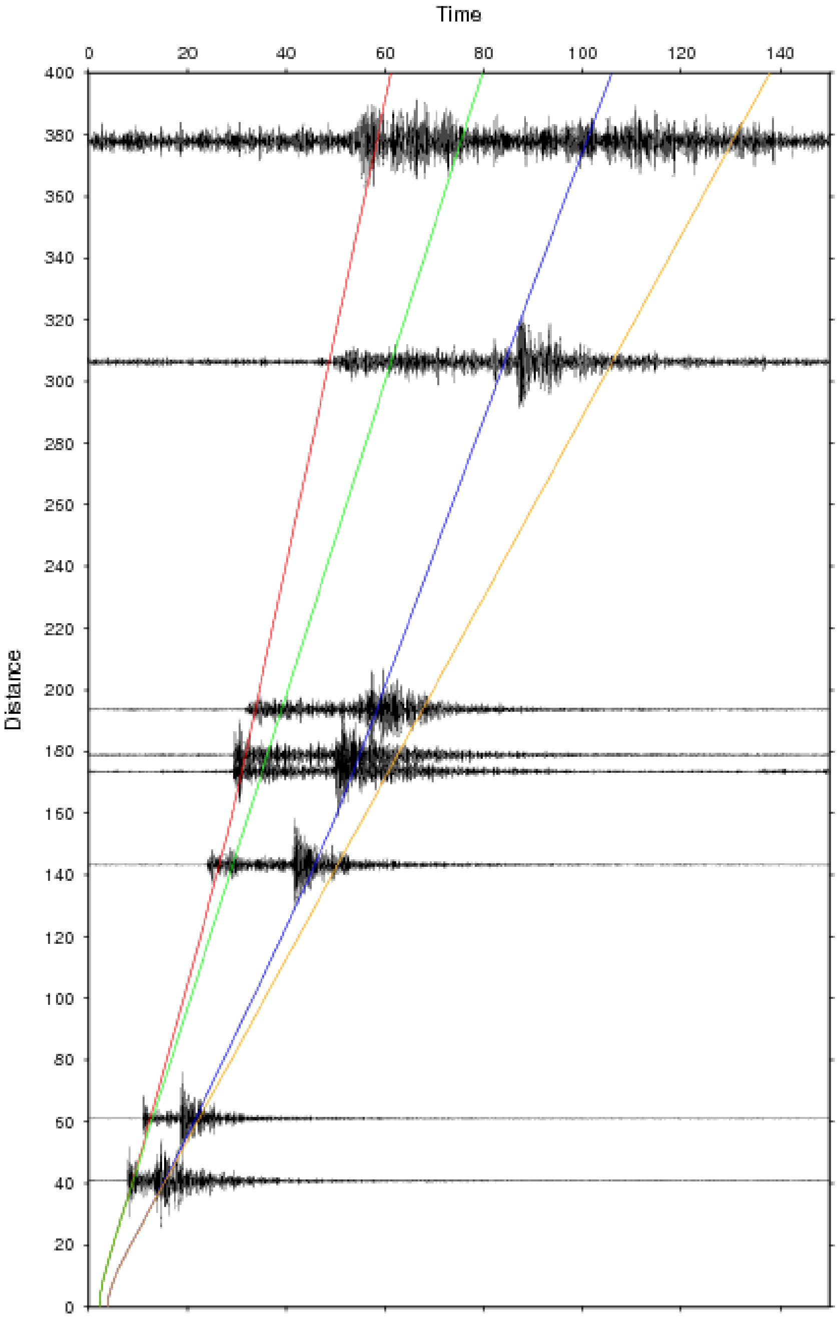

Figure 4-10: Time-distance diagram: 1D Velocity Model 4 [Ashtari et al., 2005] is used to calculate the travel times. The green color = direct P-wave (Pg), the orange color = direct S-wave (Sg), the red color = refracted P-waves (Pn) and the blue color = refracted S-waves (Sn).

4.3 Inversion for single earthquake location

4.3.1 Theory

In this method the origin time of events (t_0) and the locations of events (x_0, y_0, z_0) are unknowns and we will find them on the basis of a set of observed arrival times (t_{obs}) by an iterative inversion [*Kissling*, 1988; *Stein and Wysession*, 2009]:

$$t_{obs} = F(t_0\,, x_0\,, y_0\,, z_0\,). \qquad \textit{Equation 4-4}$$

The procedure begins after finding the ray paths and computing the theoretical arrival times (t_{calc}). In this calculation we use estimated parameters for hypocenters (t_0*, x_0*, y_0*, z_0*) as an initial model [*Kissling*, 1988; *Stein and Wysession*, 2009]:

$$t_{calc} = F(t_0^*\,, x_0^*\,, y_0^*\,, z_0^*\,) \qquad \textit{Equation 4-5}$$

The difference between the observed arrival time (t_{obs}) and the calculated arrival time (t_{calc}) gives us the travel time residuals (Δt). As hypocenter parameters (except for the origin time) have a nonlinear relationship with the travel times, we are performing a first order Taylor expansion to provide an approximate linear relationship between them [*Kissling*, 1988; *Stein and Wysession*, 2009]:

$$\Delta t = t_{obs} - t_{calc} = \sum_{k=1}^{4} \frac{\partial F}{\partial h_k} \Delta h_k \qquad \textit{Equation 4-6}$$

In matrix notation, this relation is written as

$$\Delta t = H\, \Delta h \qquad \textit{Equation 4-7}$$

Where H is a matrix containing partial derivatives of travel time with respect to hypocentral parameters ($H = \frac{\partial F}{\partial h_k}$) and Δh is adjustment to the hypocentral parameters [*Kissling*, 1988; *Stein and Wysession*, 2009].

The number of arrival times of seismic phases is greater than the hypocentral parameters; therefore to minimize the error we use the least squares method to find the adjustment (Δh) that explain travel time residuals (Kissling 1988, Stein and Wysession 2009)

$$\Delta h = (H^T H)^{-1}\, H^T\, \Delta t \qquad \textit{Equation 4-8}$$

H^T is the transpose matrix of H.

This is an iterative procedure i.e. we first find the adjustments (Δh) then we apply those adjustments to our initial model parameters and we will start again from where we began the process and so on. After each iteration the travel time residuals are expected to become smaller.

We continue the inversion until the error in the data does not allow us to get a better solution (Kissling 1988, Stein and Wysession 2009).

For inversion for single earthquake location I have used the hypocenter program, HYPOCENTER [*Lienert and Havskov*, 1995; *Ottemöller et al.*, 2011]. The complete procedure for locating an event by hypocenter program is shown in Figure 4-11.

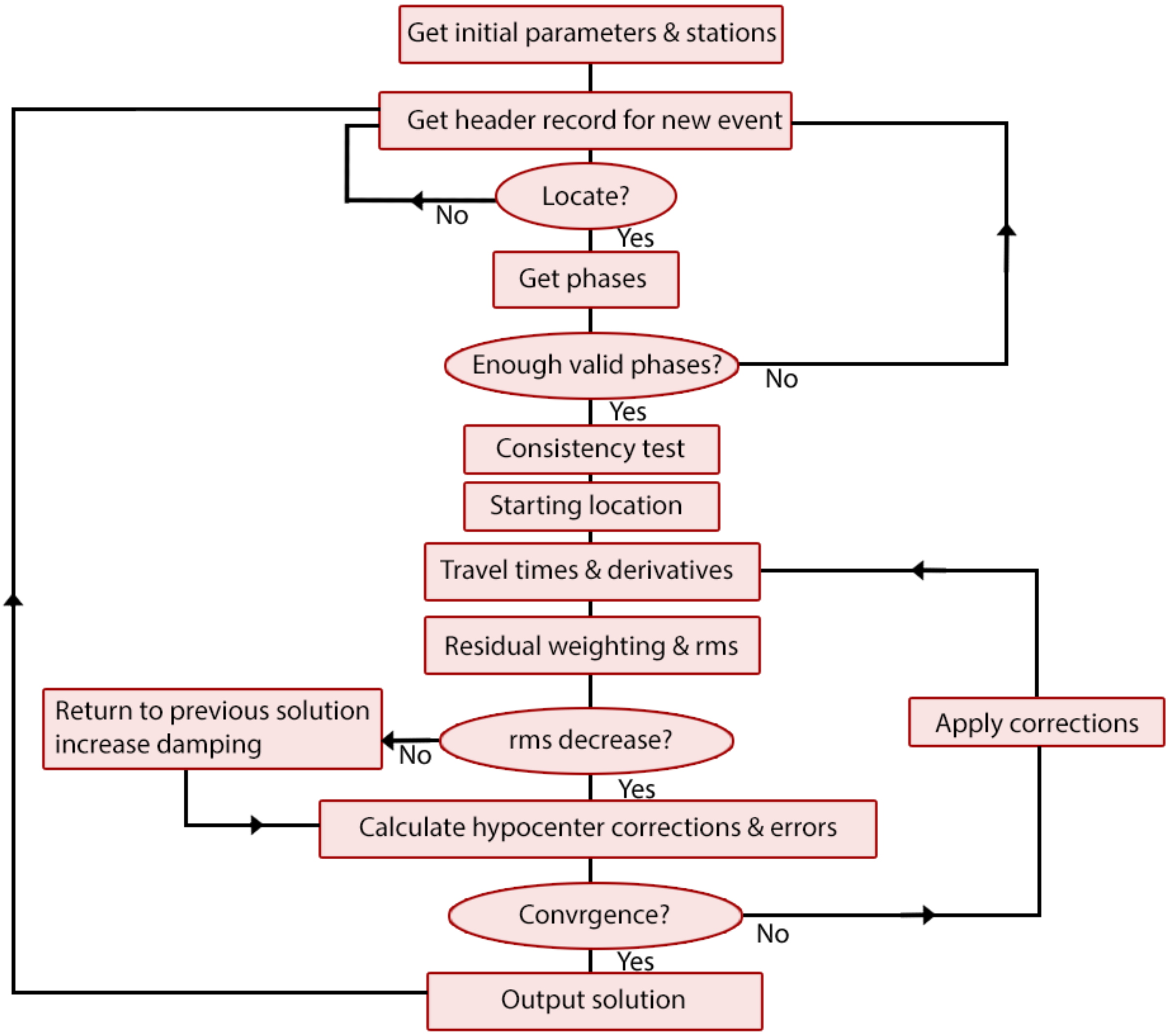

Figure 4-11: Flowchart for the hypocenter program[Lienert and Havskov, 1995].

4.3.2 Results

The hypocenter program can locate a dataset and calculate a mean rms value for the entire dataset [*Ottemöller et al.*, 2011]. I have run the hypocenter program for all my events with the four different models. By using the mean rms value, I can compare the velocity models and say which one of them works better. As Table 4-6 shows, model 2 (Abbassi, Nasrabadi et al. 2010) provides a smaller mean rms value; therefore it works better. The mean rms value for model 1 is also small and close to the model 2.

In these two velocity models (model 1 and 2) the crust is divided in quite a similar way and the corresponding P-velocities are also fairly close. The crust is divided into 4 and 5 layers in model 1 and 2, respectively, and it can be explained that model 1 takes a thick sedimentary layer (6 km) in the upper crust, but in model 2, the sedimentary layer is divided in 2 thinner layers. The main difference between model 1 and 2 is that the depth of Moho is 46 and 58, respectively.

The higher mean rms value for model 3 and 4 can be explained that velocity model 3 represent the lowest Moho depth (35 km) for this area and P-velocities are lower in model 4 compared to other velocity models.

velocity model	**Number of events**	**Mean rms value**
Model 1 (IIEES)	408	0.776
Model 2 (Abbassi, Nasrabadi et al. 2010)	408	0.649
Model 3 (Ashtari, Hatzfeld et al. 2005)	408	1.041
Model 4 (Doloei and Roberts 2003)	407	1.809

Table 4-6: Comparison of velocity models by mean rms value calculated by the hypocenter program.

To see how much difference the different velocity models make for locating earthquakes, I compared the changes between the calculated depth and distance of events using various models in 6 figures (Figure 4-12-Figure 4-17). Figure 4-13 shows that there are small depth and distance changes between using model 1 and 3 which indicates model 1 and 3 should be the most similar models. Comparison between Figure 4-12 and Figure 4-13 shows that model 1 and 2 are more different than model 1and 3. As Figure 4-14 shows for depth difference between model 1 and 4 is small, but for location I have quite a lot of changes. Similarly the other velocity models can be compared. These comparisons are useful because they are telling something about uncertainties in the locations.

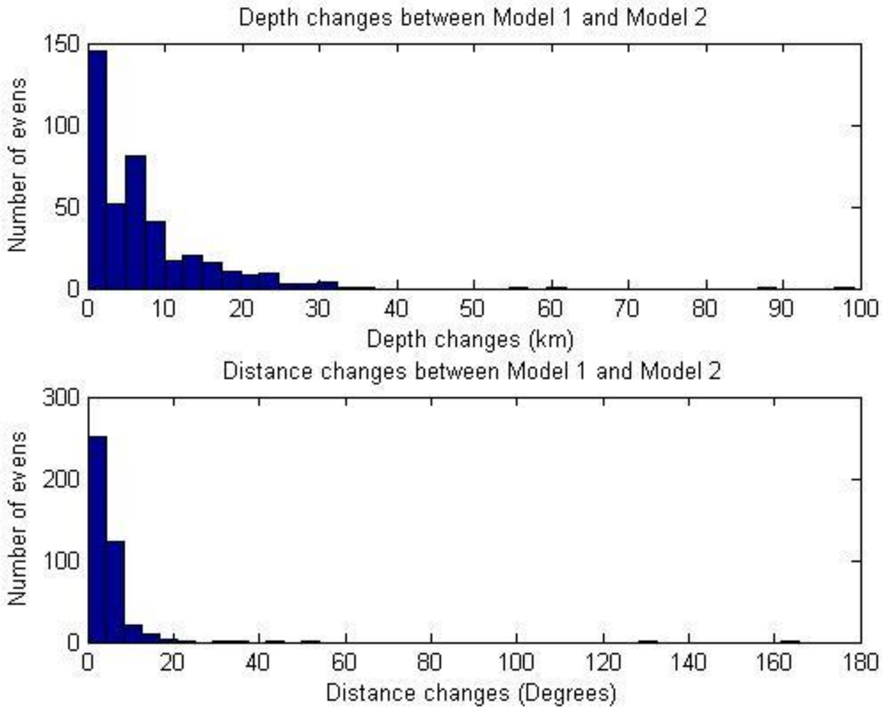

Figure 4-12: Depth and distance chances between Model 1 and Model 2.

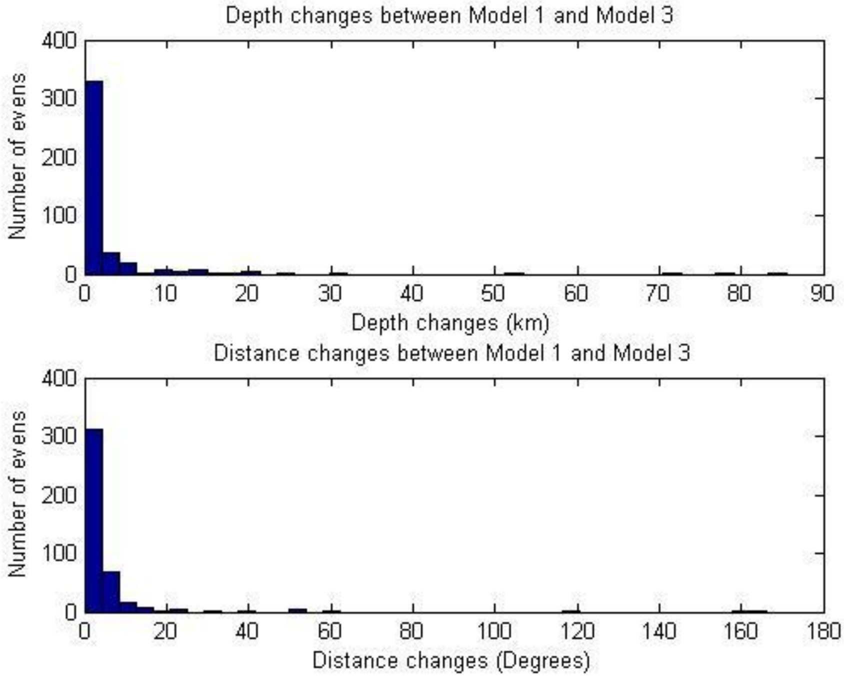

Figure 4-13: Depth and distance chances between Model 1 and Model 3.

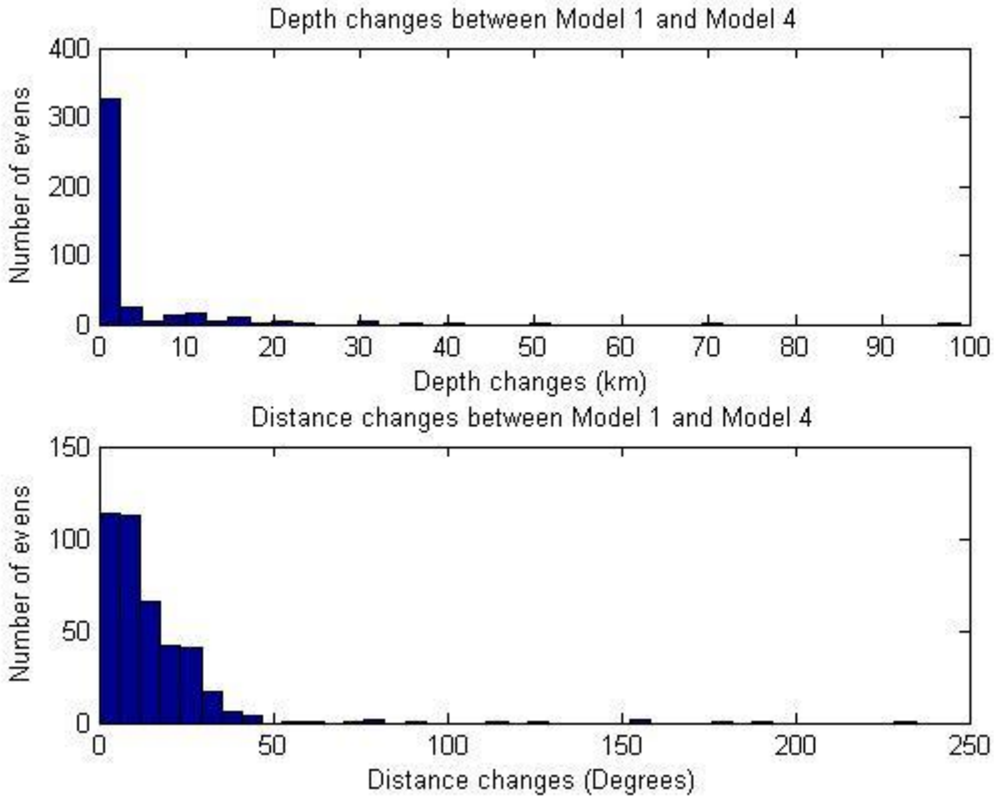

Figure 4-14: Depth and distance chances between Model 1 and Model 4.

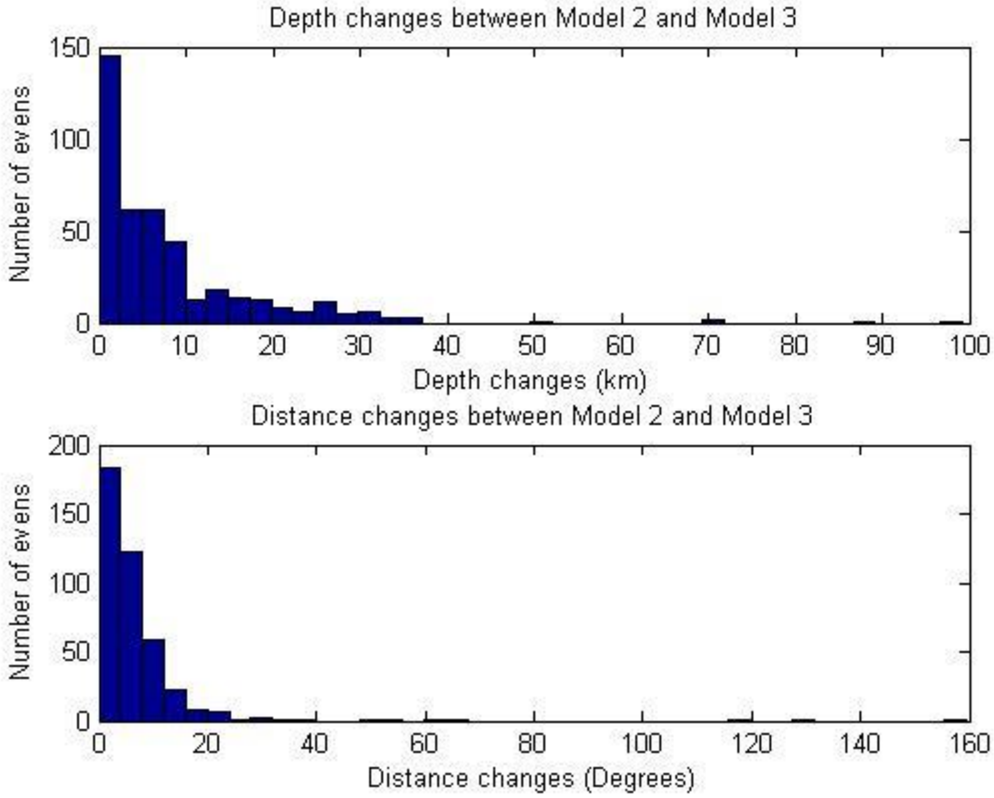

Figure 4-15: Depth and distance chances between Model 2 and Model 3.

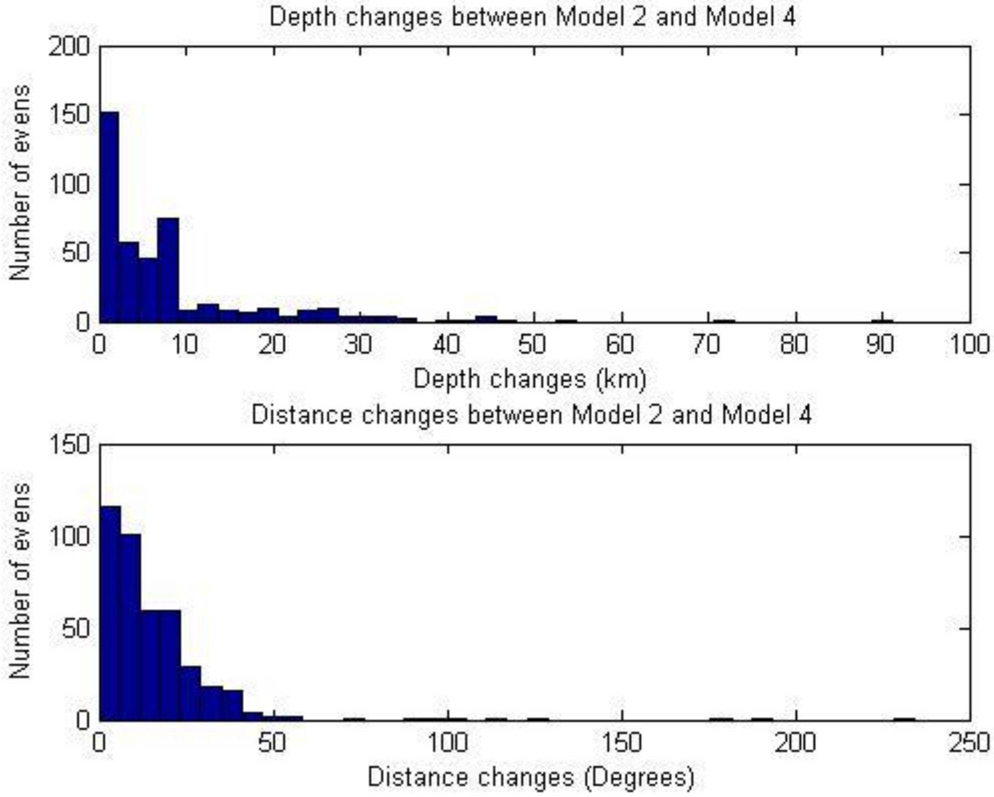

Figure 4-16: Depth and distance chances between Model 2 and Model 4.

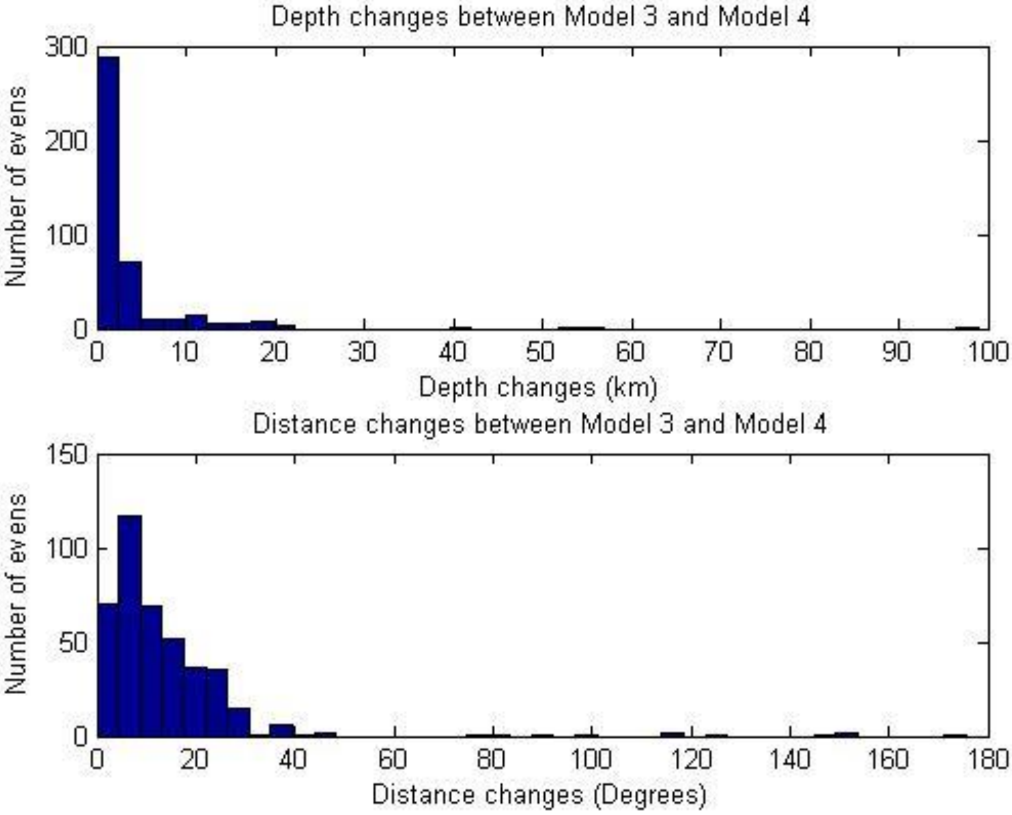

Figure 4-17: Depth and distance chances between Model 3 and Model 4.

4.4 Joint hypocenter and velocity model inversion

4.4.1 Theory

In this method the origin time of events (t_0), the locations of events ((x_0, y_0, z_0)) and velocity model (V(x, y, z)) of area are unknowns and we find them on the basis of a set of arrival times (t_{obs}) by a simultaneous iterative inversion for a set of earthquake hypocenters and velocity model for the area [*Kissling*, 1988]

$$t_{obs} = F\big(t_0\,, x_0\,, y_0\,, z_0\,, V(x, y, z)\big). \qquad \textit{Equation 4-9}$$

Similar to inversion for single event location that is explained in section 4.3, the procedure begins after finding the ray paths, by computing the theoretical arrival time (t_{calc}). In this calculation we use estimated parameters for hypocenters (t_0*, x_0*, y_0*, z_0*) and a 1D velocity model which is a result from previous studies as initial model parameters ($V^{existing}$ (x,y,z)) [*Kissling et al.*, 1994]

$$t_{calc} = F\left(t_0^*\,, x_0^*\,, y_0^*\,, z_0^*\,,\ V^{existing}\,(x, y, z)\right) \qquad \textit{Equation 4-10}$$

The difference between the observable arrival time (t_{obs}) and the calculated arrival time (t_{calc}) gives us the travel time residuals (Δt). As hypocenter parameters (except for the origin time) and velocity model parameters have a nonlinear relationship with the travel times, we are performing a first order Taylor expansion to Equation 4-9 to provide an approximate linear relationship between them. Afterwards, we add an error vector (e) to the equation. e contains different types of errors that affect the calculation of travel times and the errors that are made as a result of linear approximation

$$\Delta t = t_{obs} - \ t_{calc} = \textstyle\sum_{k=1}^{4} \frac{\partial f}{\partial h_k} \Delta h_k + \sum_{i=1}^{n} \frac{\partial f}{\partial m_i} \Delta m_i \ + e \quad \textit{Equation 4-11}$$

In matrix notation, this relation is written as

$$\Delta t = H\,\Delta h + M\,\Delta m + e \qquad \textit{Equation 4-12}$$

Where H is a matrix containing partial derivatives of travel time with respect to hypocentral parameters ($H = \frac{\partial f}{\partial h_k}$) and M is a matrix containing partial derivatives of travel time with respect to velocity model parameters ($M = \frac{\partial f}{\partial m_i}$). By combining all the partial derivatives in a matrix (A) and parameters adjustments in a vector (d), we get:

$$\Delta t = A\,\Delta d + e \qquad \textit{Equation 4-13}$$

To minimize the effect of error vector (e) to our results we use the damped least squares method to find the adjustments (Δd) that explain travel time residuals [*Snieder and Trampert*, 1999]

$$\Delta d = (A^T A + d)^{-1} A^T \Delta t \qquad \textit{Equation 4-14}$$

A^T is the transpose matrix of A and d is a matrix that contains damping parameter.

This is an iterative procedure i.e. we find the first adjustments (Δd) then we apply those adjustments to our initial model parameters and we will start again from where we began the process. In the end of each iteration we will get a RMS residual for all events used in the inversion that can be used to judge and compare the results from each iteration. We can continue the procedure until we don't get a better solution.

Simultaneous inversion leads to locating of a set events with smaller errors and finding a new velocity models by improving the existing initial velocity models. The new velocity model can describe better the local seismic wave propagation compared to the initial velocity model [*Aloisi et al.*, 2002] and is called a minimum 1D model, since the standard deviation of the travel time residuals is minimized in this calculation [*Kissling*, 1988].

A very important criteria that we must take into account in this method is that we have to use high quality data with many observations. Poor selection of data will change the outcome. [*Kissling et al.*, 1994].

The complete procedure for calculating minimum 1D model is shown in Figure 4-18. In this algorithm ray tracing as a forward problem and applying the simultaneous inversion is done by running the VELEST program (Figure 4-18, Figure 4-19). The description for use of VELEST program is given by Kissling, Kradolfer et al. 1995.

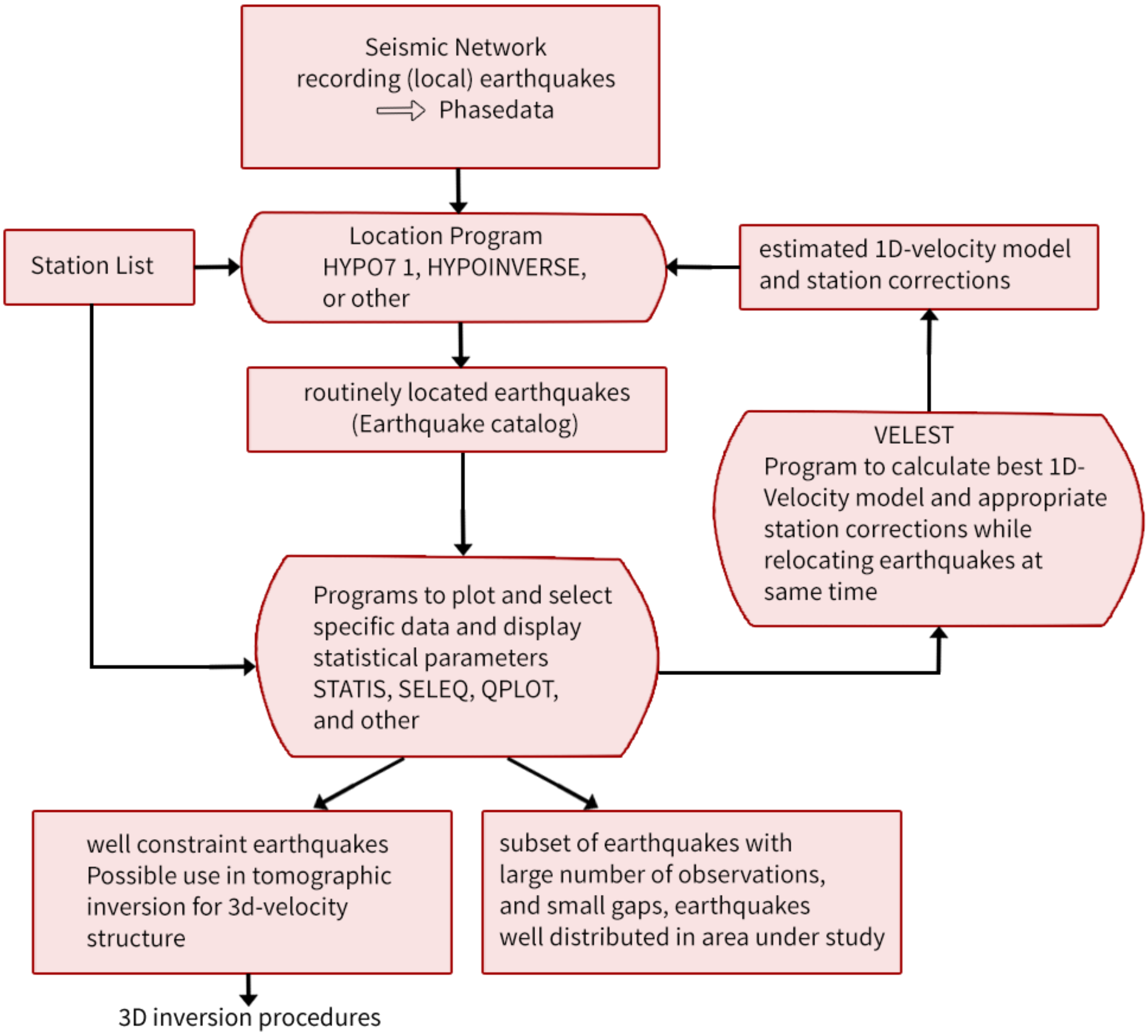

Figure 4-18: Flowchart to obtain a minimum 1D model [Kissling, 1988].

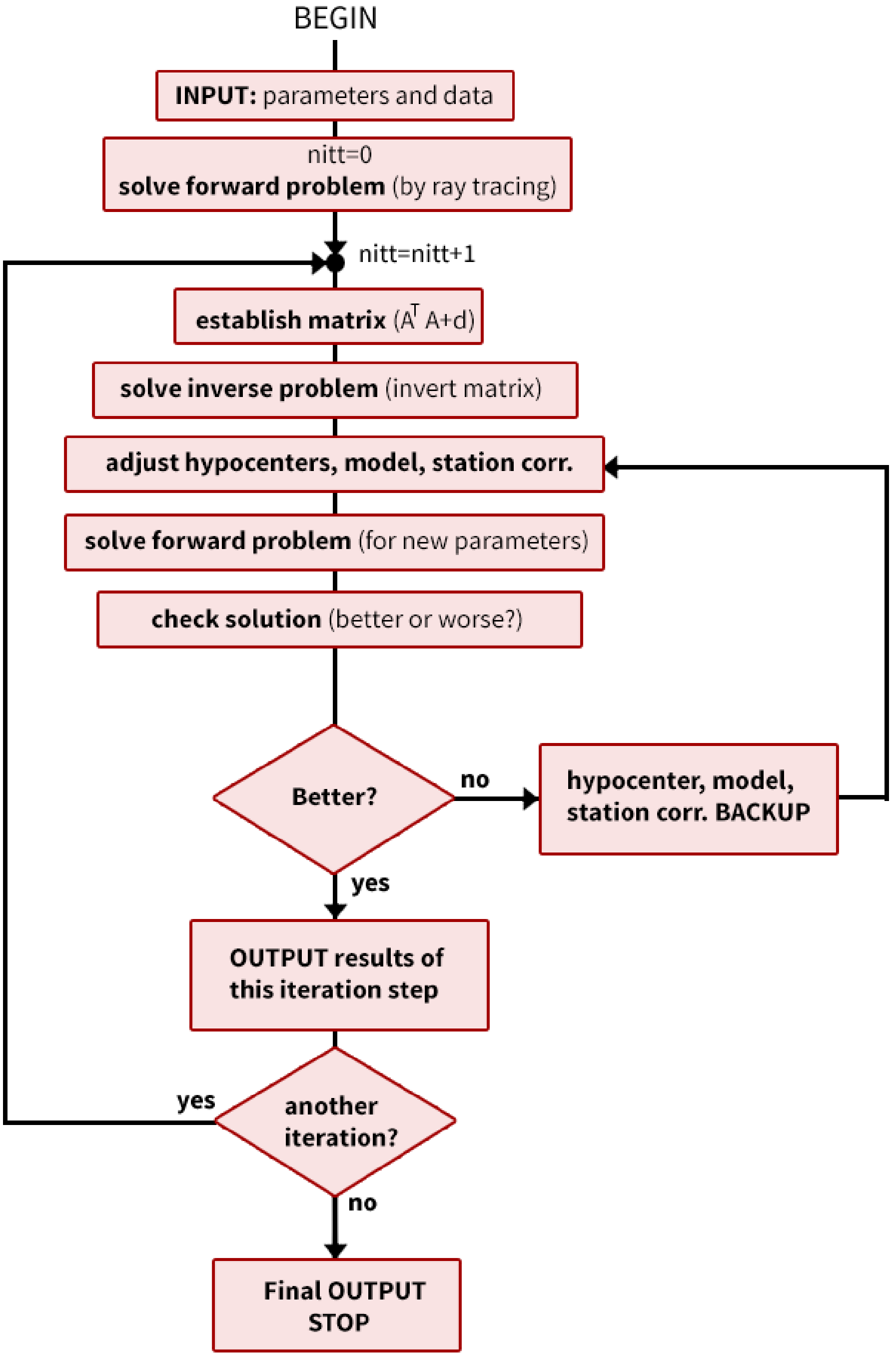

Figure 4-19: Flowchart for the VELEST program modified from Kissling, Kradolfer et al. 1995.

4.4.2 Results

In this study, I used the 4 velocity models that I already used to locate my data set as initial model and tried to improve them by running simultaneous inversions. Unfortunately, I did not have any artificial sources of known locations to verify results, and used the RMS residuals to compare the results and to say which of the resulting minimum 1D models work better.

I selected a data set consisting of 126 earthquakes which can be located with at least 5 P observations, since S observations have not been used. The reason that S-observations not used is that VELEST program uses only the first S-phase and I read S-phase as Sg-phase, since I could not see Sn-phase on my waveforms (section 4.1). I have chosen 5 iteration for the running of simultaneous inversions. As Table 4-7 shows, I goet smaller RMS residual in each iteration. Comparison of the RMS residual at each iteration shows the minimum 1D model with the model 1 as initial model at iteration No.5 provides a smaller RMS residual. It could mean that this new model works better for my entire data set by providing smaller mean rms value; therefore to check the results from simultaneous inversion I ran the hypocenter program for the final minimum 1D models to see how the mean rms values (Table 4-6) for the entire data set is changed. Results are shown in Table 4-8. It shows that three of minimum 1D models provide smaller mean rms values compared with their initial models, but minimum 1D model for model 2 is not working as expected and gives a higher mean rms values compared with its initial model. To examine why this is so

- I ran the VELEST using a smaller data set consisting of 39 events which could be located with at least 7 P observations, but I did not get any better result.
- I also ran the VELEST one more time using same data set (39 events) to calculate correction station and added the correction station when I ran hypocenter program, but it did not change the result.
- It is most likely that since I have not used S-phases in the calculation, the new model will not work for the entire data set when I include S-readings. To check it I ran hypocenter program using the initial modeler and the new models for the entire data set when I excluded S phases. Results are shown in Table 4-9 which shows something similar to initial results.

The reason that the new model does not provide smaller mean rms value for the entire dataset, could be that the initial model 2 is not close to the true model, but it is not the case, since this initial model provides the lowest mean rms value for the entire dataset and I had been hoping to get even smaller mean rms value after running VELEST program. This example shows that inversion even for a 1D model is not trivial as it depends on the starting model, the data and is a non-unique problem. It appears that for model 2, only the inclusion of the S-waves in the inversion would provide a final model that would reduce the combined overall RMS.

The minimum 1D model for each initial model is shown in Table 4-10, Figure 4-20, Figure 4-21, Figure 4-22 and Figure 4-23. As it is shown in the figures, the new velocity models for model 2 and model 4 generally show higher P-velocities compared to their initial velocity models where increasing of velocity is most in model 2 (Figure 4-21) and as a result of this velocity increasing 2 layers in model 2 are combined as one layer. The velocity also increased for model 1 and model 3, but only in the upper layers in the crust and then there was a reduction of velocity at Moho for model 1 and model 3.

	RMS Residual for iteration No. 0	RMS Residual for iteration No. 1	RMS Residual for iteration No. 2	RMS Residual for iteration No. 3	RMS Residual for iteration No. 4	RMS Residual for iteration No. 5
Model 1	0.561848	0.484727	0.443173	0.418135	0.402843	0.399002
Model 2	0.944115	0.632142	0.497608	0.442786	0.431468	0.429454
Model 3	1.020493	0.756485	0.527768	0.485867	0.469743	0.457921
Model 4	0.827116	0.736876	0.696968	0.669658	0.646963	0.626431

Table 4-7: RMS residual of each iteration for all events used in the inversion calculated by the VELEST program, where Model 1= (IIEES), Model 2 = (Abbassi, Nasrabadi et al. 2010), Model 3= (Ashtari, Hatzfeld et al. 2005) and Model 4= (Doloei and Roberts 2003).

The final minimum 1D velocity model	Number of events	Mean rms value
Model 1 (IIEES)	408	0.764
Model 2 (Abbassi, Nasrabadi et al. 2010)	408	0.719
Model 3 (Ashtari, Hatzfeld et al. 2005)	408	0.763
Model 4 (Doloei and Roberts 2003)	408	1.500

Table 4-8: Comparison of the final minimum 1D velocity models by mean rms value calculated by the hypocenter program.

	The initial 1D velocity model		**The final minimum 1D velocity model**	
	Number of events	Mean rms value	Number of events	Mean rms value
Model 1 (IIEES)	353	0.554	356	0.425
Model 2 (Abbassi, Nasrabadi et al. 2010)	364	0.397	364	0.427
Model 3 (Ashtari, Hatzfeld et al. 2005)	359	0.809	364	0.529
Model 4 (Doloei and Roberts 2003)	349	0.588	350	0.586

Table 4-9: Comparison of the initial 1D velocity models and the final minimum 1D velocity model for the entire data set when I excluded S-phases by mean rms value.

Model 1		**Model 2**		**Model 3**		**Model 4**	
Depth (km)	P-Velocity (km/s)	Depth (km)	P-Velocity (km/s)	Depth (km)	P-Velocity (km/s)	Depth (km)	P-Velocity (km/s)
-5.0	5.95	-5.0	6.05	-5.0	5.99	-5.0	4.14
6.0	5.99	3.0	6.05	2.0	6.10	2.0	4.75
14.0	6.51	7.0	6.39	8.0	6.21	5.0	5.23
18.0	6.51	16.0	6.39	12	6.43	8.0	5.49
46.0 M	7.93	24.0	6.93	35 M	7.52	11.0	5.83
80.0	8.10	58.0 M	8.29			14.0	5.92
						19.0	6.19
						24.0	6.45
						30.0	6.45
						33.0	6.72
						36.0	7.12
						39.0	7.25
						42.0	7.25
						46.0 M	7.59

Table 4-10: The final minimum 1D model for four different initial models. M=Moho and Minus sign indicates above sea level

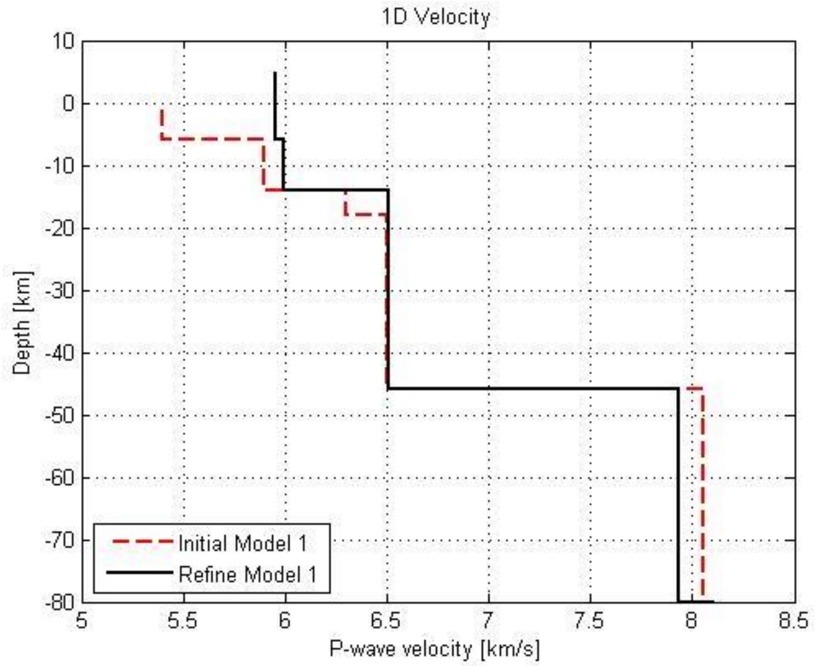

Figure 4-20: The initial model (Model 1 -IIEES) and the final minimum 1D model.

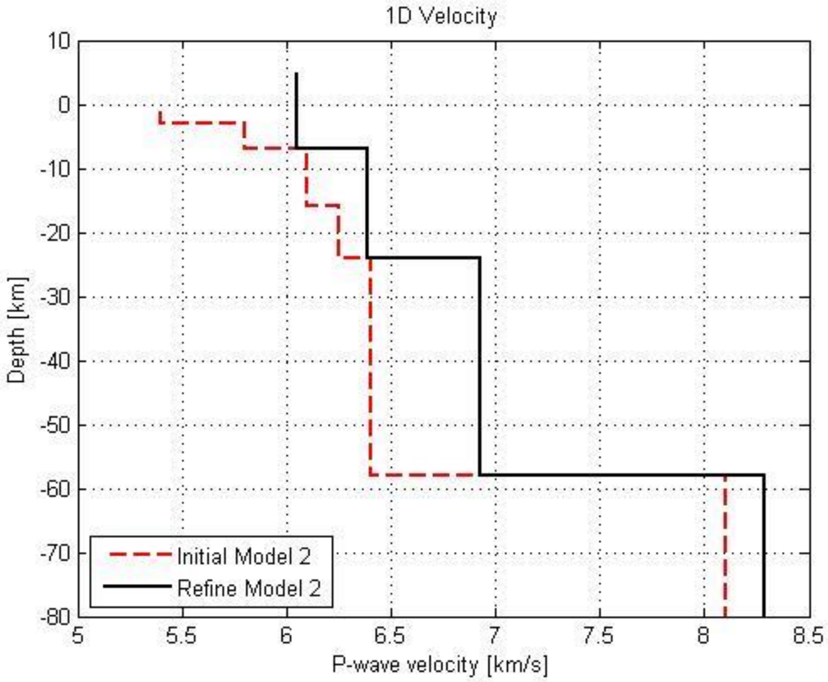

Figure 4-21: The initial model (Model 2 - Abbassi, Nasrabadi et al. 2010) and the final minimum 1D model.

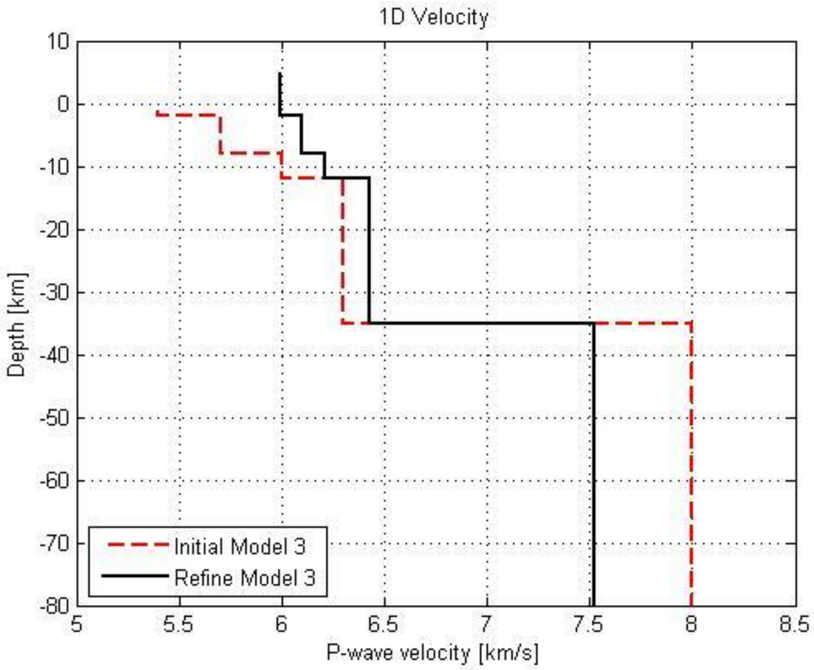

Figure 4-22: The initial model (Model 3: Ashtari, Hatzfeld et al. 2005) and the final minimum 1D model.

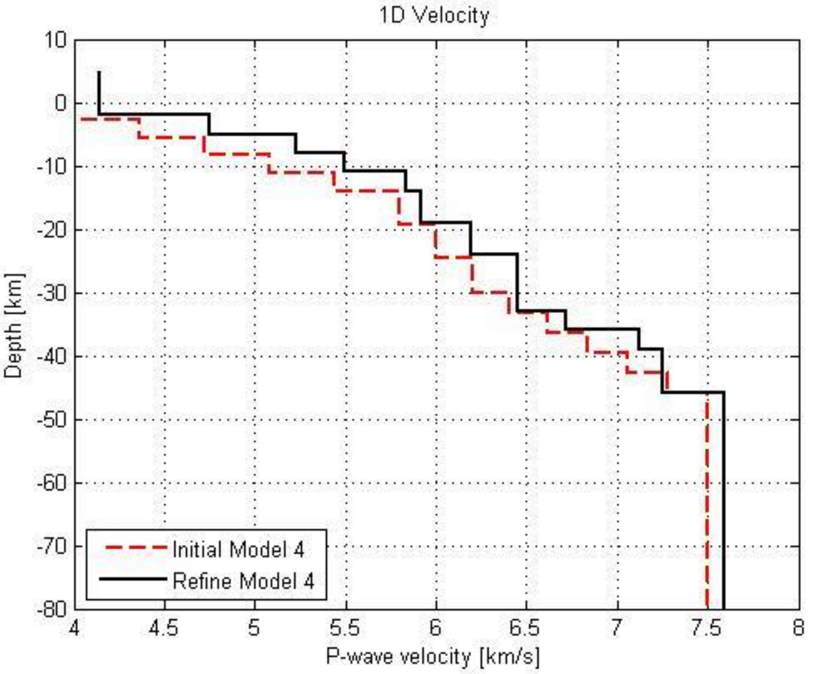

Figure 4-23: The initial model (Model 4: Doloei and Roberts 2003) and the final minimum 1D model.

4.5 Double difference earthquake location

By the double difference earthquake location method we can relocate a large data set simultaneously, where there is relative short distance between the neighboring events. In this method we use the residuals (Δt_k^{ij}) between the observed and calculated travel time difference for two earthquakes (i and j) that are observed on a common station (k) to find adjustment to the hypocentral parameters [*Waldhauser and Ellsworth*, 2000].

$$\Delta t_k^{ij} = (t_k^i - t_k^j)^{obs} - (t_k^i - t_k^j)^{Calc} \qquad \text{Equation 4-15}$$

In this way we cancel common mode errors and we can get better earthquake locations [*Waldhauser and Ellsworth*, 2000; *Waldhauser and Schaff*, 2008]. I attempted to use the use the hypoDD program [*Waldhauser*, 2001].

For double difference earthquake location I selected a data set consisting of 272 earthquakes which can be located with at least 4 P observations, since S observations are not going to use in this calculation. In this selection, it was unfortunately very few events that were relatively close; therefore I could not use this method.

5 Magnitude of events

One way of estimating the magnitude of earthquakes is measuring the amplitude of the seismic waves. The amplitude of seismic waves decreases as a function of distance as a result of geometric spreading and attenuation. Therefore it is necessary to correct the change of amplitude with distance in determining the magnitude of an event [*Stein and Wysession*, 2009]. This correction should be region-dependent since geometric spreading and attenuation depends on the Earth structure in a region [*Ottemöller and Sargeant*, 2013].

In this section, I tried to find a local magnitude scale (M_L) for study the area using magnitude inversion technique and then, I compared the new magnitude scale with Hutton and Boore (1987) scale which is developed for southern California and has been applied in the computation of M_L in Iran.

5.1 Amplitude reading

I used vertical component and the horizontal components for this purpose. Before amplitude reading, the recorded ground displacements were filtered with Wood-Anderson response. S – waves was used to amplitude reading and they were measured in nanometers. Measurements were done using the SEISAN [*Ottemöller et al.*, 2011].

The total number of amplitudes reading is 2147 and 3893 on the vertical - and the horizontal components, respectively.

5.2 Magnitude (M_L) Inversion

5.2.1 Theory

The local magnitude scale (M_L) is the earliest magnitude scale and was introduced by Richter. He used shallow events in Southern California and Wood-Anderson seismographs to develop M_L [*Richter*, 1935]. The original form of the M_L is modified several times. The new version of M_L can be written as [*Ottemöller and Sargeant*, 2013]

$$M_{Lij} = log\, A_{ij} + a\, log\, R_{ij} + bR_{ij} + S_j + C \qquad Equation\ 5\text{-}1$$

Where i is earthquake index and j is station index, A is ground displacement simulated on Wood-Anderson seismograph in nm, R is hypocentral distance in km and S_j is station correction. a, b and C are constants for geometrical spreading, attenuation and the scale to have the same magnitude for same amplitude similar to the original M_L, respectively.

To find a local magnitude scale for a region we need to estimate a, b, C and Sj parameters.

By reformulating the equation we get a linear relationship between the amplitude observations and the other parameters

$$-\log A_{ij} = a \log R_{ij} + bR_{ij} - M_{Lij} + S_j + C \qquad \textit{Equation 5-2}$$

Using this linear relationship and singular value decomposition, we can find geometrical spreading – and attenuation parameters for the region of interest, station corrections and the local magnitude of the events.

To invert the local magnitude scale we use MAG2 program [*Ottemöller et al.*, 2011]. This program finds all our unknown parameters simultaneously.

We can also evaluate the magnitude scale by calculating standard deviation of all magnitude residuals using MAGSTAT program [*Ottemöller et al.*, 2011].

5.2.2 Results

I used the amplitudes on the vertical - and the horizontal components to make vertical to horizontal comparison. This comparison shows that amplitudes on horizontal components are 1.48 larger than amplitudes on vertical components on average.

I used observations from the two horizontal components to invert for the local magnitude scale as amplitudes on horizontal components (E and N) as they were larger than the vertical component (Z) (Table 5-1).

Station code	Z-component	E-component	N-component
ASAO	702.0	948.0	993.8
DAMV	323.1	675.3	715.8
NASN	31.1	43.6	35.5

Table 5-1: Horizontal to vertical amplitude comparison in nanometers for 2004 .7.2-event

Table 5-2 shows statistical information in this calculation.

Number of events in input file	409
Number of events used	340
Number of observations	3397
Number of stations	16
Minimum observation per earthquake	6

Table 5-2: Statistical information for calculation of the local magnitude scale of Iran using horizontal components.

The initial inversion with horizontal data resulted in a=0.99, so that in subsequent runs I fixed a=1 and inverted for the other parameters. a and b are dependent on one another and by putting a equal to 1, b become equal to 0.0021 . Table 5-3 shows the results of inverting for a-, b-, C- and S parameters using horizontal components.

a	1					
b	0.0021					
C	-1.89218					
S	Number	Station Code	Station Residuals	Uncertainties +/-	Latitude °N	Longitude °E
	1	ASAO	0.023	0.0975	34.548	50.025
	2	DAMV	-0.304	0.0993	35.630	51.971
	3	NASN	0.162	0.1298	32.799	52.808
	4	THKV	-0.385	0.1102	35.916	50.879
	5	SNGE	-0.166	0.1039	35.092	47.347
	6	MAKU	0.578	0.3092	39.355	44.683
	7	SHGR	-0.244	0.2048	32.108	48.801
	8	CHTH	-0.010	0.1079	35.908	51.126
	9	MRVT	-0.060	0.1870	37.659	56.089
	10	GHVR	-0.207	0.1009	34.480	51.245
	11	ZNJK	-0.030	0.1123	36.671	48.685
	12	KHMZ	-0.043	0.1079	33.740	49.964
	13	TABS	0.206	0.3624	33.649	57.119
	14	SHRO	0.248	0.2076	36.008	56.013
	15	GRMI	-0.062	0.1302	38.810	47.894
	16	BJRD	0.293	0.4172	37.700	57.408

Table 5-3: The local magnitude scale of Iran using horizontal components. a= geometrical spreading, b= attenuation, C=the scale to have the same magnitude for same amplitude similar to the original M_L and S=station corrections.

The values of a and b, calculated from horizontal components are used in calculation of station corrections using vertical component (Table 5-4, Table 5-5).

Number of events in input file	409
Number of events used	130
Number of observations	961
Number of stations	15
Minimum observation per earthquake	6

Table 5-4: Statistical information for calculation of the station corrections (S) using vertical component.

	Number	Station Code	Station Residuals	Uncertainties +/-	Latitude ºN	Longitude ºE
S	1	ASAO	-0.027	0.1296	34.548	50.025
	2	DAMV	-0.076	0.1341	35.630	51.971
	3	NASN	0.186	0.1814	32.799	52.808
	4	SHGR	-0.177	0.3903	32.108	48.801
	5	SNGE	-0.120	0.1382	35.092	47.347
	6	THKV	-0.156	0.1395	35.916	50.879
	7	CHTH	-0.131	0.1300	35.908	51.126
	8	MRVT	0.085	0.2551	37.659	56.089
	9	MAKU	0.169	0.5834	39.355	44.683
	10	GHVR	0.002	0.1332	34.480	51.245
	11	ZNJK	0.033	0.1339	36.671	48.685
	12	KHMZ	-0.223	0.1475	33.740	49.964
	13	TABS	0.070	0.4969	33.649	57.119
	14	SHRO	0.207	0.2788	36.008	56.013
	15	GRMI	0.159	0.1984	38.810	47.894

Table 5-5: The station corrections (S) using vertical component.

The Hutton and Boore (1987) scale has been applied in the computation of M_L in the study area. In this magnitude scale it is not used station correction and constants are a = 1.110, b = 0.00189 and C= -2.09 [*Hutton and Boore*, 1987] in which 1.110 and 0.00189 are geometrical spreading parameter and attenuation parameter for the Southern California.

Comparison of the new M_L scale (using horizontal components), the new M_L scale (using vertical component) and Hutton and Boore (1987) scale by calculated standard deviation of all magnitudes (Table 5-6) and plotting M_L residuals of events (Figure 5-1) shows that the M_L scale (using horizontal components) works slightly better for study area; therefore as amplitude on horizontal components are larger than vertical components it would be better to use horizontal amplitudes or add station corrections from horizontal components.

Figure 5-2 shows that ($-\log A_0$) term as a function of distance for the Hutton and Boore (1987) scale and Iran M_L scale are almost identical. In addition, comparison of magnitude scales means that geometrical spreading parameter (a) is slightly lower and attenuation parameter (b) is slightly higher in study area compared to Southern California. However, the $-\log A_0$ plot shows that there is almost no difference and the trade-off between a and b can produce the same correction with slight differences in a and b.

Scale	Station Correction	M_L Scale Parameter a	ML Scale Parameter b	Standard Deviation of All Magnitudes
The new M_L scale (using horizontal components)	Yes (Table 5-3)	1	0.0021	0.3044
The new M_L scale (using vertical component)	Yes (Table 5-5)	1	0.0021	0.3106
Hutton and Boore (1987)	No	1.110	0.00189	0.3106

Table 5-6: Comparison of magnitudes scales by calculated standard deviation.

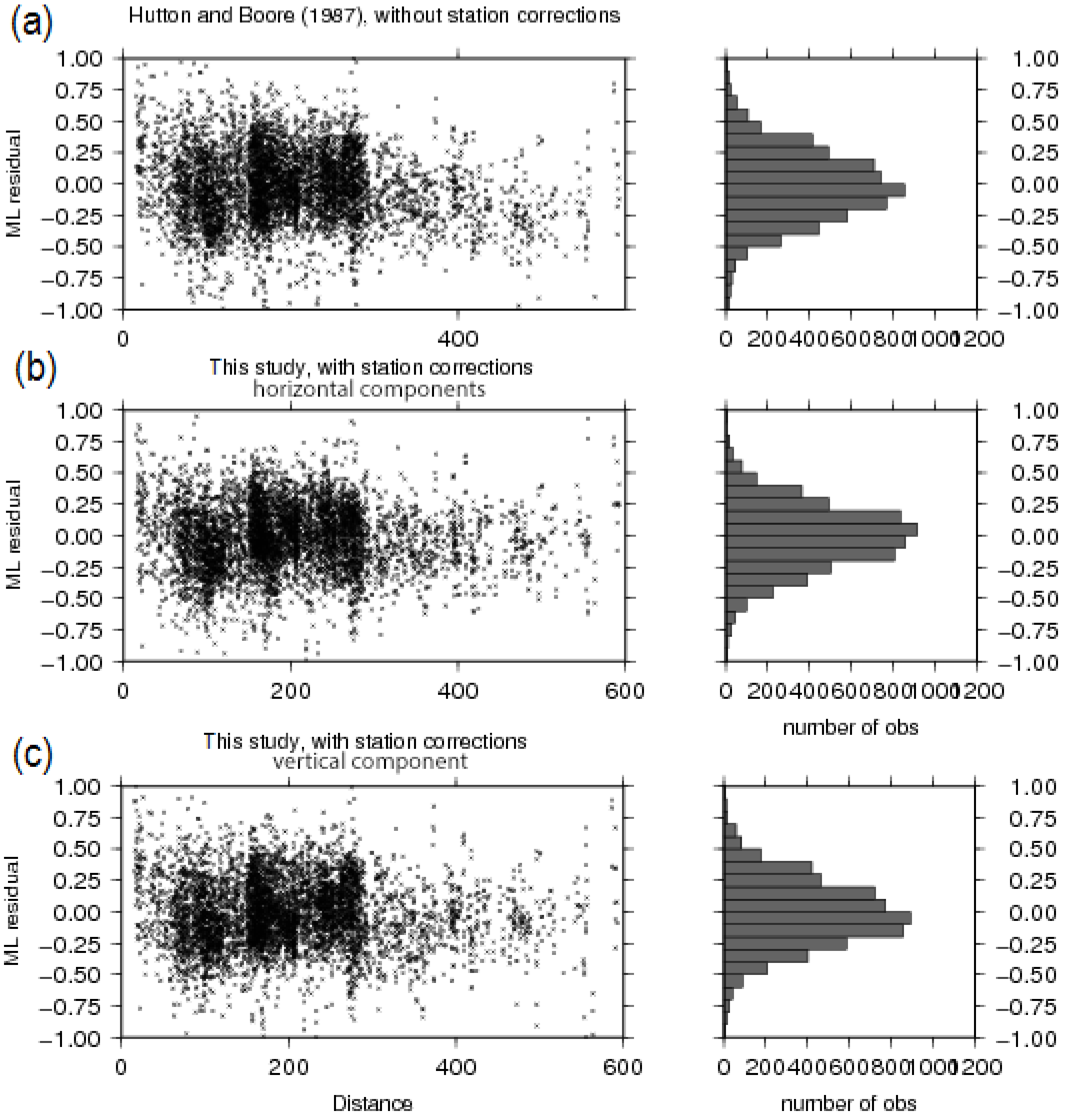

Figure 5-1: Comparison of M_L residuals of events using (a) Hutton and Boore (1987) scale; (b) calculated magnitude scale using horizontal components; (c) calculated magnitude scale using vertical component.

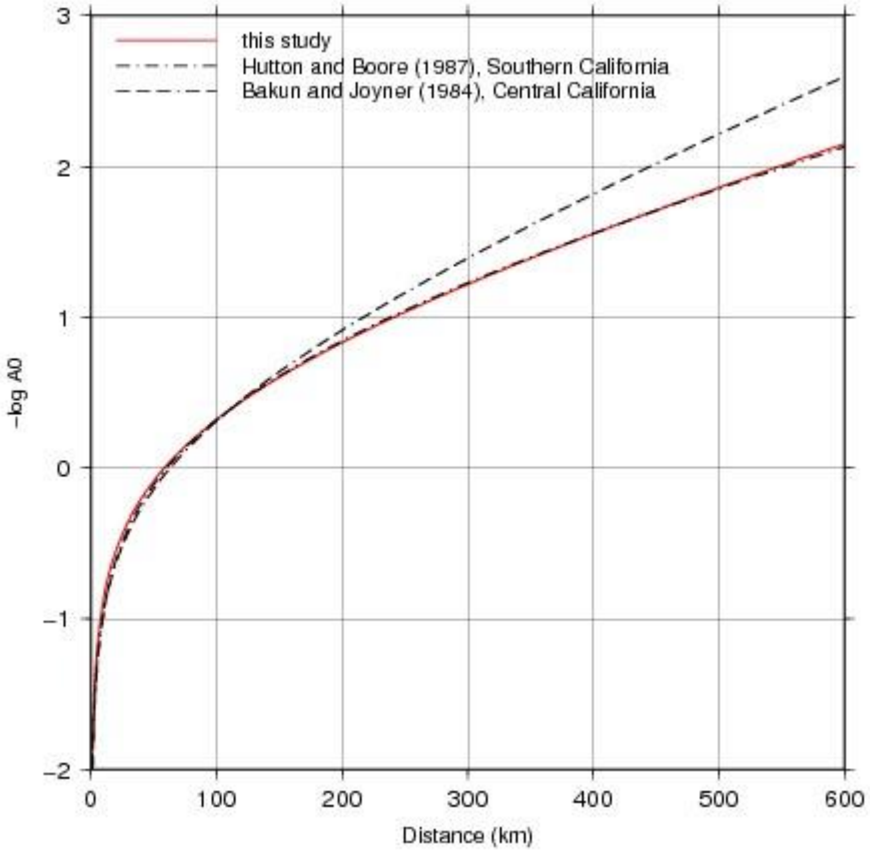

Figure 5-2: Comparison of (-logA_0) term as function of distance. A is measured in nanometers.

6 Geometry of faulting

Strike-, dip- and slip angles are three parameters that describe the geometry of faults (Figure 6-1) and since seismic waves radiate in various patterns in different fault geometry, we are using the amplitudes and shape of seismic waves recorded on seismograms to find the geometry of faulting, called for focal mechanism [*Stein and Wysession*, 2009]. Fault plane solution are determined to identify and understand faults and tectonic of an area.

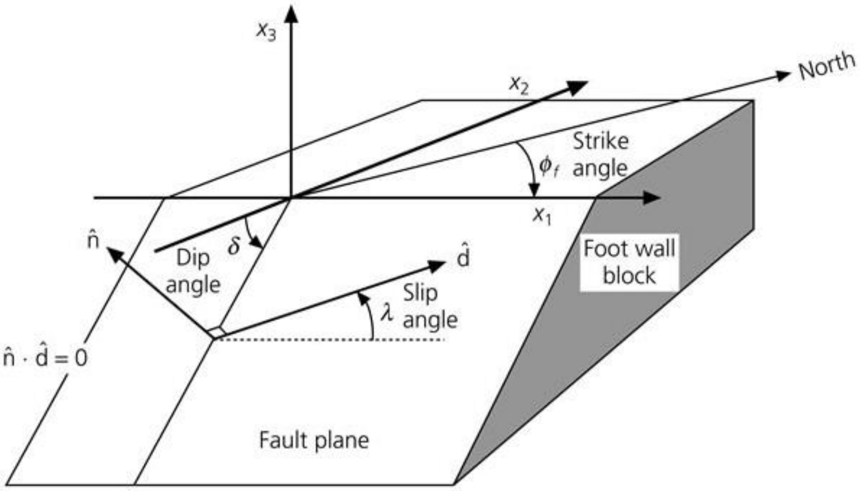

Figure 6-1: The parameters used to describe the geometry of faults. $\hat{d}$ = slip vector and $\hat{n}$ = normal vector [Stein and Wysession, 2009].

There are different methods to find the focal mechanisms where we use some parts of seismograms or the whole seismograms. For this purpose I used:

1) Polarity of the first motion (P-wave) and amplitude ratio, using FOCMEC Program [*Snoke*, 2003] and HASH Program [*Hardebeck and Shearer*, 2008].
2) Moment tensor inversion using Time-Domain Moment Tensor Inverse Code [*Dreger*, 2002] where full waveforms were used.

Moment tensor inversion can be performed to study the events with magnitude greater than 3.5 (M_L> 3.5) [*Dreger*, 2002]; therefore I selected a data set consisting of 14 earthquakes with M_L> 3.5 and I determined the focal mechanisms for them, using different programs and afterwards compared the results.

6.1 Relation between geometry of faults and regional tectonics

The relation between geometry of faults and regional tectonics can be described by principal stresses, labelled as σ_1, σ_2 and σ_3. The principal stresses are compressive stresses in lithosphere where σ_1 is the maximum compressive stress (P), σ_2 is the intermediate principal stress and σ_3 is the minimum compressive stress (T) [*Stein and Wysession*, 2009].

We can determine the stress orientations in the lithosphere by assuming that faults form on a plane 45 degree from σ_1-axis and depending on the orientation of the σ_1-axis and σ_3-axis we will have different types of faulting and focal mechanisms (Figure 6-2). Hence the axes of principal stresses must be perpendicular to each other where we describe them as a vertical- and two parallel axes to the surface [*Stein and Wysession*, 2009].

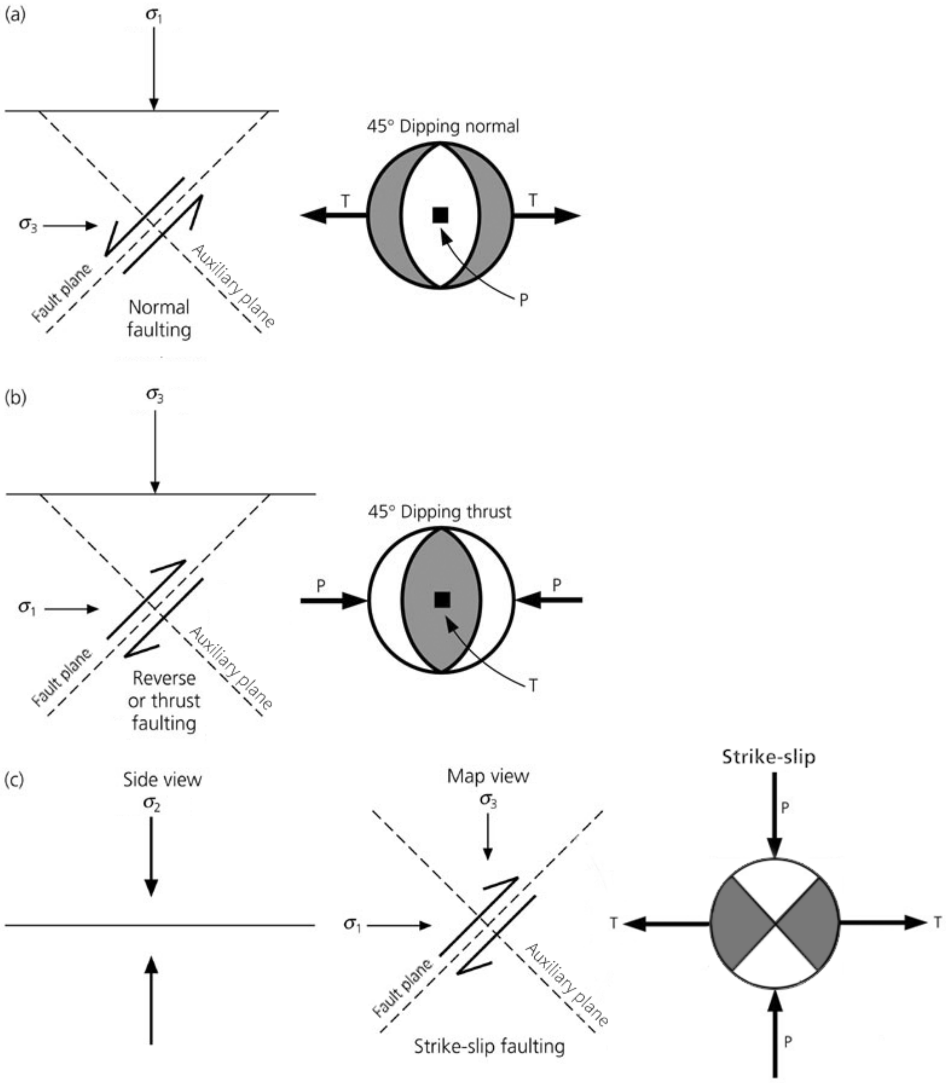

Figure 6-2: The relation between orientation of principal stresses and different types of faulting modified from Stein and Wysession, 2009. a) Normal faulting b) Reverse or thrust faulting c) Strike-slip faulting.

6.2 Polarity of the first motion (P-wave) and amplitude ratio

6.2.1 Theory

Polarity of the first motion (P-wave):

First motion or polarity of P-wave (Pg- or Pn-phase depending on cross-over distance) is a method to find the focal mechanism by using a small part of the seismogram. In this method we read the polarity of the first phase (P-wave) of seismogram to see if it is registered upward or downward. It is because the P wave is recorded upward in compressional quadrants, downward in dilatation quadrants and it will be very small or zero along the fault- and auxiliary planes [*Stein and Wysession*, 2009].

The different rays are defined on the focal sphere by the azimuth and take-off angle. Take-off angle is the angle at which the seismic waves leave the source. Afterwards, we can plot the polarity observations based on azimuth of the stations and the incidence angle of the wave at the stations on a stereonet and try to find the nodal planes that separate compressional and dilatational quadrants as good as possible [*Stein and Wysession*, 2009].

In this method, we get the best results when we have many stations in various directions relative to the source [*Havskov and Ottemoller*, 2010].

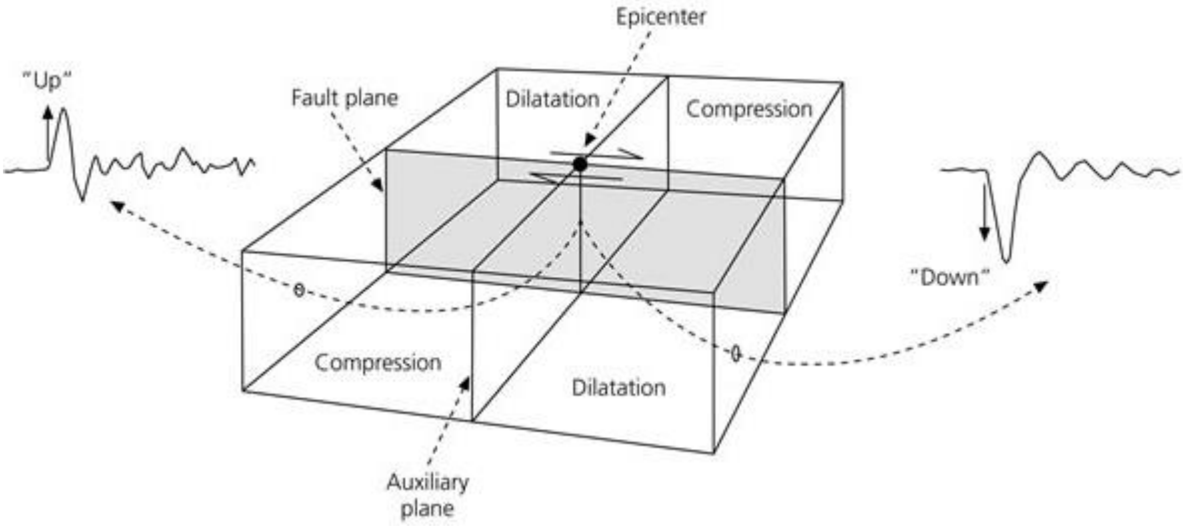

Figure 6-3: The first motion is recorded upward in compression quadrants and downward in dilatation quadrants [Stein and Wysession, 2009].

Amplitude ratio:

Seismic waves have different amplitudes in various directions relative to fault slip. For example, in a homogeneous sphere the amplitude of the P-wave is very small or zero along the fault plane and auxiliary plane, but amplitude of S-wave is the maximum in these directions (Figure 6-4). Hence, amplitude ratio of different waves in the same direction will help us to find the geometry of faults and it is used as a complementary method for the first motion method, when we do not have enough polarity observations [*Havskov and Ottemoller*, 2010].

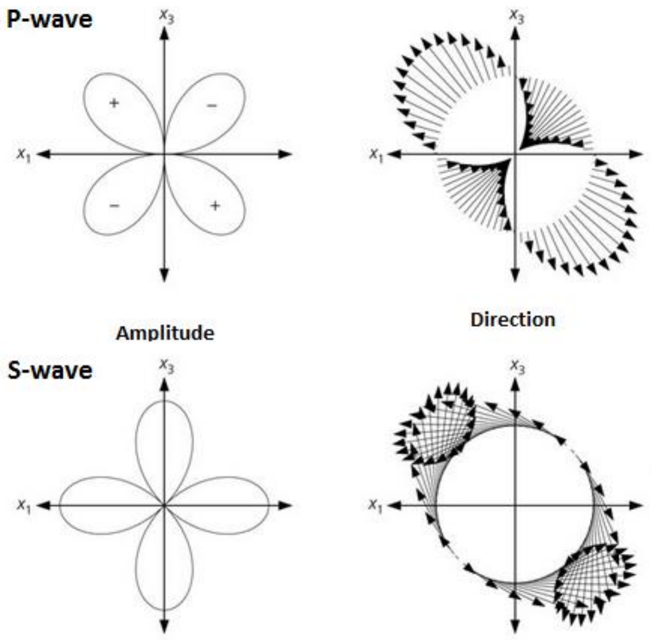

Figure 6-4: Amplitude patterns of P-wave and S-wave in a homogeneous sphere. Auxiliary plane is along the x_3 axis and fault plane is along the x_1 axis [Stein and Wysession, 2009].

The reason we use the amplitude ratio of seismic waves and not the absolute amplitudes is that there is less uncertainty in the determination of the amplitude ratio than the absolute amplitudes since some effects on seismic amplitudes such as source and instrument effects will be canceled in an amplitude ratio, but one still needs to correct for attenuation difference between P and S- and free surface [*Havskov and Ottemoller*, 2010].

FOCMEC Program and HASH Program:

In order to compare the results, I used the polarity of P-wave and amplitude ratio of phases as inputs in two different programs, FOCMEC [*Snoke*, 2003] and HASH [*Hardebeck and Shearer*, 2008], where FOCMEC Program computes and reports all possible solutions [*Snoke*, 2003] and I need to select the most likely solution from the reported solutions. The HASH program is a bit different in that it assesses the possible solutions for focal mechanism by taking into account various uncertainties such as error in polarity observations, locating and velocity model and then it selects the best solution [*Hardebeck and Shearer*, 2008].

6.2.2 Input for FOCMEC Program and HASH Program

I read the polarity of the first motion for 14 earthquakes with $M_L > 3.5$ (Table 6-1). To avoid choosing the wrong polarities, polarity reading was made on the stations that clearly show upward or downward movements. Therefore, the number of read polarities (Table 6-1) will be dependent on the number of stations and the quality of the stations that are registered for these events. Reading the polarity is done on the vertical component and we don't perform any filter on the waveform as it may change the polarity [*Havskov and Ottemoller*, 2010].

Figure 6-5 shows polarity reading that I have done for one of the events.

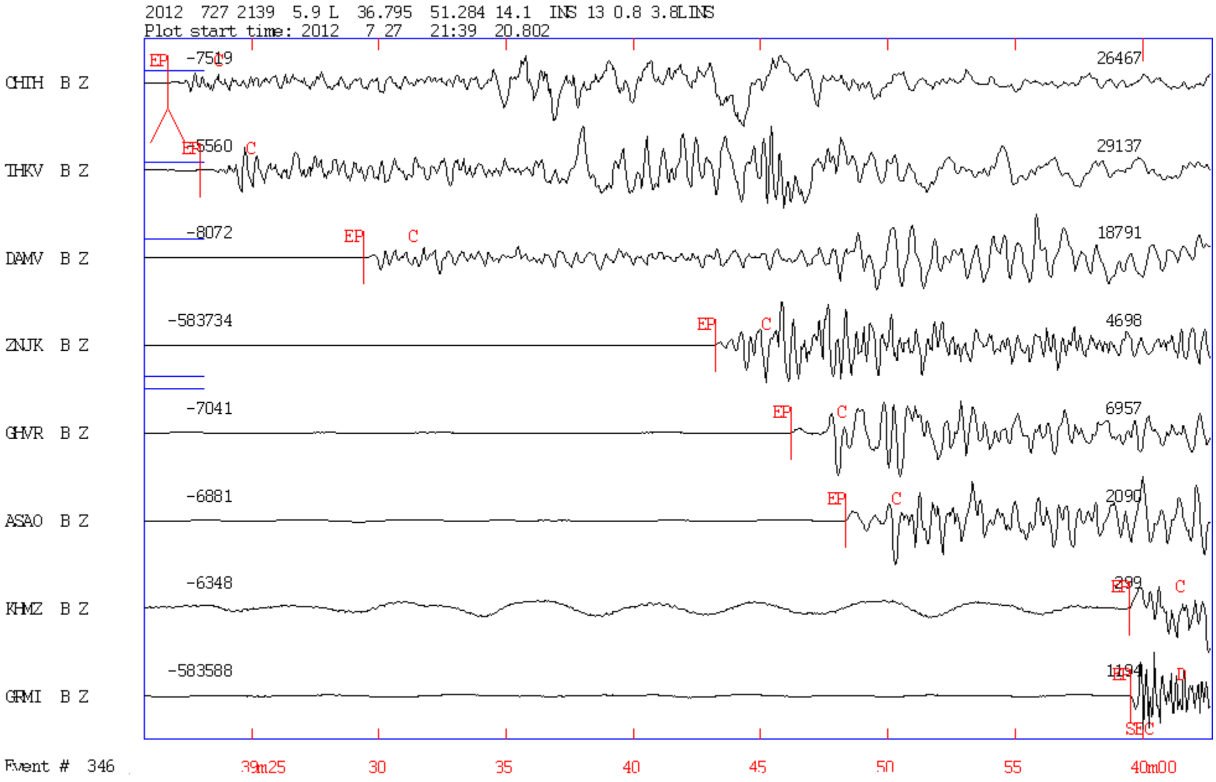

Figure 6-5: Polarity reading of the first motion on the vertical components for the 27.7.2012-event. Ep shows arrival time of the first P-phase. C= upward motion and D= downward motion.

For the amplitude ratio I used the amplitude of Pg and Sg phases. The selection was made on the vertical-(V) and transverse (T) components, respectively and it was applied a band-pass filter between 0.1- 1.0 Hz before amplitude reading. Three stations (Table 6-1) were used for each event and it was tried to select the nearest stations to the source where V and T components were both of good quality. The approach was to use few good stations to avoid difficulties in the corrections for longer and possibly more complicated rays.

Figure 6-6 shows amplitude reading of Pg and Sg phases that I have done for one of the events.

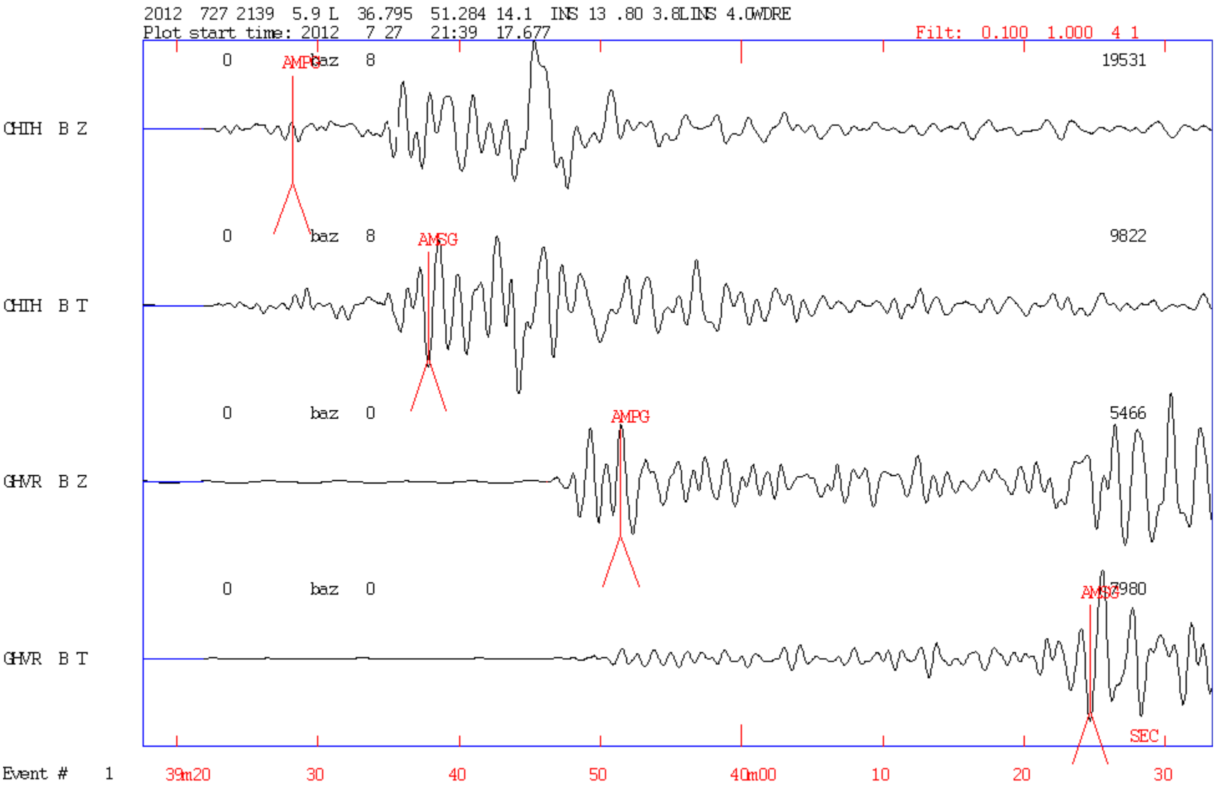

Figure 6-6: Amplitude reading of Pg and Sg phases on the vertical-(V) and transverse (T) components, respectively for the 27.7.2012-event. Two stations are used for the amplitude ratio. AMPG = amplitude of Pg and AMSG= amplitude of Sg.

No.	**Date of events**	**Magnitude**	**Number of the first polarities**	**Number of amplitude ratio**	**Stations used for amp. ratio**
1	17th October 2004	4.1	4	3	ASAO-THKV-DAMV
2	8th November 2004	3.9	5	3	THKV- DAMV-GRMI
3	24th July 2005	3.8	3	3	SNGE- DAMV-GRMI
4	20th December 2006	3.7	6	2	THKV-CHTH
5	11th May 2007	3.7	3	3	THKV-CHTH-GRMI
6	27th March 2008	3.7	7	3	ZNJK-SNGE-ASAO
7	27th May 2008	4.8	9	3	THKV-SNGE-CHTH
8	13th September 2008	3.7	7	2	ZNJK-THKV
9	26th September 2008	3.9	6	3	ZNJK-ASAO-SNGE
10	28th April 2010	3.7	7	2	ZNJK-ASAO
11	8th September 2010	3.8	5	2	CHTH-GRMI
12	18th March 2012	4.1	7	3	ZNJK-THKV-CHTH
13	27th July 2012	3.7	8	2	CHTH-GHVR
14	27th July 2012	3.8	8	2	CHTH-GHVR

Table 6-1: Focal mechanism analysis is done for these events.

6.3 Moment tensor inversion

6.3.1 Theory

A double couple force is considered sufficient to cause slip along the fault plane and generates seismic waves. A double couple force is a pair of force couples with opposite direction offset by a small distance, where one of pairs is oriented parallel to fault plane and the other pair is oriented parallel to auxiliary plane [*Stein and Wysession*, 2009].

Fault geometries depend on the orientation of these force couples. To have a general description that represents different fault geometries we combine double couple forces of different orientations into seismic moment tensor (M), where null axes, the maximum compressive stress axis (P) and the minimum compressive stress axis (T) are the eigenvectors of the moment tensor.

The moment tensor is symmetric. It consists of nine force couples and only six of them are independent. The components of moment tensor in an arbitrary orthogonal coordinate system are given by the scalar moment (M_0), the normal vector to the fault plane ($\hat{n}$) and the slip vector ($\hat{d}$) [*Stein and Wysession*, 2009]

$$M_{ij} = M_0(n_i d_j + n_j d_i) \qquad \text{Equation 6-1}$$

To find components of the moment tensor we write the entire seismogram (u) as linear function of the six independent components of moment tensor (m) and their corresponding Green's function (G)

$$u_i(t) = \sum_{j=1}^{6} G_{ij}(t) m_j \qquad \text{Equation 6-2}$$

Where i representing number of stations and j is equal to six. In matrix notation, this relation is written as [*Stein and Wysession*, 2009]

$$u = Gm \qquad \text{Equation 6-3}$$

We invert this equation using the least squares method to find the components of moment tensor [*Stein and Wysession*, 2009]

$$m = (G^T G)^{-1} G^T u \qquad \text{Equation 6-4}$$

In the moment tensor inversion full waveforms are used.

To find the focal mechanisms using moment tensor I have used Time-Domain Moment Tensor Inverse Code [Dreger, 2002]. This software package has the option to model the synthetic waveforms using computed moment tensor and it provides a quality value for comparison between the observed and synthetic waveforms. Quality value vary in the range between 1 and

4, where 4 representing the best result. In this way we can gauge the result of the inversion [*Dreger*, 2002].

6.3.2 Input for moment tensor inverse software

Moment tensor inversion can be performed to study the events with magnitude greater than 3.5 (ML> 3.5) [*Dreger*, 2002] which are large enough to generate surface waves; therefore I selected a data set consisting of 14 earthquakes with ML> 3.5.

For inversion I rotated Vertical (V), North (N) and East (E) components to Vertical (V), Radial (R) and Transverse (T) components and applied a band-pass filter between 0.03 - 0.1 Hz to use low frequency signals (long period signals). Seismograms were computed in units of ground velocity.

In general I tried to use V, R and T components, but for the stations that qualities of the T or R components were not good enough, I used only V components (Table 6-2).

In some stations that I could see synthetic waveforms are close to those observed in the V and R component and not in T component, I excluded T component and then I ran inversion again by using V and R components and assuming that T component is ok.

Finding focal mechanisms using moment tensor depends on the depth of source. I used the depth that was found in section 4, using the velocity model from IIEES for the selected data set (Table 6-2). This software package have the option to make grid search to find the most appropriate source depth which could give better results, but this was not done here to have consistent results with the location section as well as the first motion based approach.

No	Date of events	Magnitude	Source depth (Km)	Station codes
1	17th October 2004	4.1	15	ASAO-THKV
2	8th November 2004	3.9	17.1	MAKU-SNGE-THKV
3	24th July 2005	3.8	18.1	DAMV-SNGE-THKV
4	20th December 2006	3.7	14.1	CHTH-THKV-ASAO
5	11th May 2007	3.7	14.2	CHTH-THKV-ASAO-DAMV
6	27th March 2008	3.7	39.6	ASAO-ZNJK
7	27th May 2008	4.8	14.1	ASAO-SNGE-THKV
8	13th September 2008	3.7	14.1	ASAO-CHTH-DAMV-THKV-ZNJK
9	26th September 2008	3.9	15	ZNJK-ASAO-THKV-CHTH
10	28th April 2010	3.7	15	ZNJK-ASAO-SNGE-CHTH
11	8th September 2010	3.8	15	DAMV- NASN
12	18th March 2012	4.1	14.1	ZNJK-THKV-CHTH-SNGE-KHMZ
13	27th July 2012	3.7	15	ASAO-CHTH-GHVR-KHMZ-THKV
14	27th July 2012	3.8	14.1	CHTH-THKV-ASAO-KHMZ-SHRO

Table 6-2: Information about the Inputs for moment tensor inverse software.

6.4 Results and comparison

I selected a data set consisting of 14 earthquakes with ML> 3.5 and I determined the focal mechanisms for them, using the different programs. In this section I compared the results and I selected the solution that I thought is best due to number of polarity observations, number of errors in calculation of focal mechanisms and the quality value that Time-Domain Moment Tensor Inverse Code give for inversion. The quality value vary in the range between 1 and 4, where 4 representing the best result.

I selected the solution that was presented by inversion when the quality value for inversion is 2 or 3, since in this method the entire waveform is used. Otherwise, I preferred to choose Hash solution due to various uncertainties are taken into account in calculating the focal mechanism instead of the solution which I selected from FOCMEC solutions. One solution from the FOCMEC solutions was selected when the quality value of inversion is 0 or I could see one polarity error in the Hash solution. Table 6-3 and Figure 6-7shows the selected focal mechanisms for the selected data set.

1) **17th October 2004-event:**

   Using 4 polarities, 3 amplitude ratios and 5 degree increments, FOCMEC generated 73 solutions where all P- and T- axes were gathered together (Figure 6-8). I selected the most likely solution from the reported solutions. The solutions that Hash and moment tensor inversion generated are quite similar and the selected solution from FOCMEC and the other two solutions show a similar direction for T axis (Figure 6-9). Although 4 polarities are not enough to determine reliable solutions for Hash and FOCMEC, quality value of inversion is 3 and it confirms the direction of the T axis (Figure 6-10, Table 6-4).

2) **8th November 2004-event:**

   5 polarities and 3 amplitude ratios was used for FOCMEC and Hash. The solution that Hash produced was similar to the 12 solutions that FOCMEC generated (Figure 6-11, Figure 6-12). Moment tensor inversion provided a solution which P and T axes have different directions relative to the solutions from the two other programs and it was not consistent with the polarity observations, which is not surprising since the quality value for inversion is zero (Figure 6-12, Table 6-4).

3) **24th July 2005-event:**

FOCMEC using 3 polarities and 3 amplitude ratios generated 27 solutions where all P- and T- axes are gathered (Figure 6-13). The selected solution from FOCMEC and solution from Hash and moment tensor show different directions for P and T axes. Since number of polarities is very low and the quality of inversion is zero, it is difficult to choose between the solutions. I must also mention that only the selected solution from FOCMEC is consistent with the polarity observations (Figure 6-14).

4) **20th December 2006-event:**

With 6 polarities and 2 amplitude ratios could FOCMEC not presenting any solutions even with allowing errors for amplitude ratio and polarity (Table 6-4) and the solution from the moment tensor is not consistent with the polarity observations at all, where the quality of inversion is zero (Figure 6-15, Figure 6-16). Hash generated a solution with one polarity error (Figure 6-15).

5) **11th May 2007-event:**

The observed polarities were low (3 polarities) and using 3-amplitude ratios FOCMEC presented a large number of solutions (125) with 5 degree increments, where T axes were gathered in two area. A solution is selected from where T axes were gathered (Figure 6-17). T axis of the solution from Hash shows the same direction as the selected solution from FOCMEC.

Although the quality of inversion was zero, the solution is consistent with the observation polarities and the observed waveform and the synthesized waveform are not very different (Figure 6-19).

6) **27th March 2008-event:**

By using 7 polarities, 3 amplitude ratios and 5 degree increments, FOCMEC generated 5 similar solutions (Figure 6-20). Hash presented a solution with a polarity error where P axis was in the same direction as the P axes of the FOCMEC solutions, but T axis was in a different direction. The solution presented by inversion was not consistent with the observation polarities (Figure 6-21) as quality of inversion was zero.

7) **27th May 2008-event:**

With 6 polarities, 2 amplitude ratios, 10 degree increments and allowing one polarity error FOCMEC made 19 solutions (Figure 6-22). Solution from Hash is close to the selected solution from FOCMEC and moment tensor gave a solution with a quality value of 3 (Figure 6-24). T-axes of the solutions were oriented in the same direction (Figure 6-23).

8) **13th September 2008-event:**

FOCMEC, using 7 polarities and 2 amplitude ratios generated 2 solutions (Figure 6-25) and Hash gave a solution with one polarity error where T- axes were together (Figure 6-26). Despite the observed waveform and the synthesized waveform are not very different (Figure 6-27), the quality of moment tensor was zero and the solution was not consistent with a polarity observation.

9) **26th September 2008-event:**

6 polarities and 3 amplitude ratios was used for FOCMEC and Hash. FOCMEC made 29 acceptable solutions where T- axes were gathered in two areas (Figure 6-28). T-axes of Hash solution was in the same direction as FOCMEC solutions. Moment tensor inversion found a solution by a quality value of 2, but the solution was not consistent with one polarity observation (Figure 6-29, Figure 6-30).

10) **28th April 2010-event:**

Using 7 polarities, 2 amplitude ratios and 5 degree increments, FOCMEC generated 82 solutions where all T- axes were gathered together (Figure 6-31). Solution of Hash and moment tensor by a similar polarity misfit show similar T orientation as FOCMEC-solutions (Figure 6-32). The quality value of inversion is zero and the comparison between the observed waveform and the synthetic waveform is shown in Figure 6-33.

11) **8th September 2010-event:**

It was used 5 polarities and 2 amplitude ratios for FOCMEC and Hash. FOCMEC presented 23 solutions (Figure 6-34). T- axes of these solutions was consistent with the T axis of Hash. The quality value of inversion was zero and the solution showed the orientation of P-axis at which the hash and FOCMEC showed orientation of the T axis (Figure 6-35); therefore it is my best event for calculating focal mechanism.

12) **18th March 2012-event:**

FOCMEC generated 6 solutions using 7 polarities and 3 amplitude ratios where P-axes were together (Figure 6-36). Hash using same input and a polarity error and moment tensor with quality value of 2 provided solutions with similar P orientation as FOCMEC (Figure 6-37, Figure 6-38).

13) **27th July 2012-event:**

FOCMEC using 8 polarities, 2 amplitude ratios and allowing a polarity error generated 59 solutions where all P- and T- axes are gathered (Figure 6-39). The solution of moment tensor with 2 polarity misfit shows similar T orientation as FOCMEC and Hash with a polarity misfit shows another orientation for T (Figure 6-40, Figure 6-41).

14) **27th July 2012-event:**

With 8 polarities, 2 amplitude ratios and 5 degree increments FOCMEC made 98 solutions (Figure 6-42) where all P- and T- axes are gathered. Hash shows similar P axis as FOCMEC, but moment tensor showed T direction at which the hash and FOCMEC showed P direction (Figure 6-43).

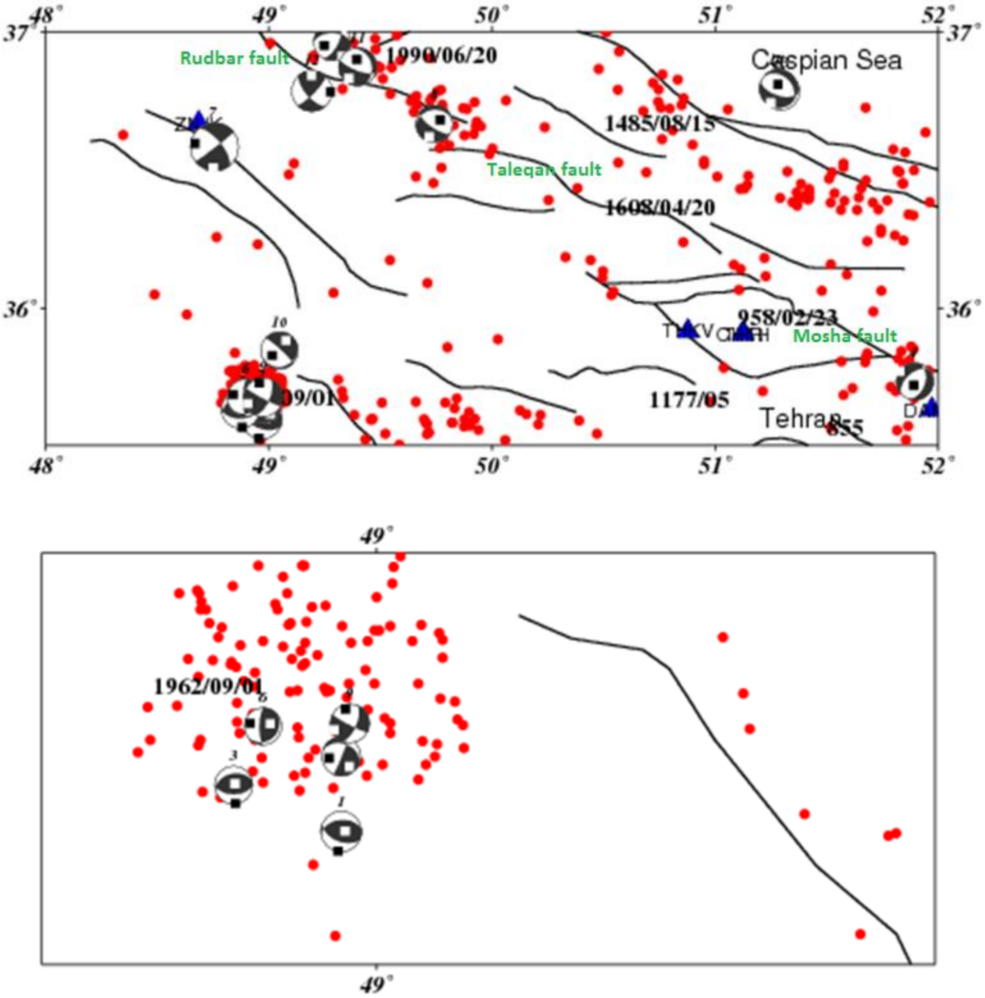

Figure 6-7: The best focal mechanisms for the selected data set. The top figure shows the study area and the bottom shows the area that focal mechanisms are overlapping.

No.	**Date of events**	**Latitude**	**longitude**	**Depth**	**Strike**	**Dip**	**Rake**	**Using program**
1	17th October 2004	35.597	48.968	15.0	112	51	109	Moment tensor inversion
2	8th November 2004	35.652	48.898	17.1	288	35	-5	Hash
3	24th July 2005	35.631	48.872	18.0	259	40	82	FOCMEC
4	20th December 2006	35.733	51.895	14.1	229	51	-69	Hash
5	11th May 2007	36.962	49.284	14.2	271	49	-37	Hash
6	27th March 2008	35.674	48.898	39.6	181	76	75	FOCMEC
7	27th May 2008	36.585	48.757	14.1	52	87	-157	Moment tensor inversion
8	13th September 2008	36.668	49.741	14.1	124	71	-73	FOCMEC
9	26th September 2008	35.676	48.976	15.0	117	83	-153	Hash
10	28th April 2010	35.846	49.048	15.0	72	13	-150	Hash
11	8th September 2010	36.873	49.398	15.0	344	27	-40	Hash
12	18th March 2012	36.786	49.192	14.1	44	78	155	Moment tensor inversion
13	27th July 2012	36.784	51.295	15.0	271	59	109	Hash
14	27th July 2012	36.795	51.284	14.1	310	32	-72	Hash

Table 6-3: The best focal mechanisms for the selected data set.

		FOCMEC				**HASH**		**Moment tensor inversion**
No.	Date of events	No. of solutions presented	Degree increments	Allowing Amp. ratio errors	Allowing Polarity errors	Polarity errors	Min. average Amp. ratio errors	Quality
1	17th October 2004	9 73	10 5	0 0	0 0	0	0.02	3
2	8th November 2004	12	5	0	0	0	0.03	0
3	24th July 2005	27	5	0	0	1	0.07	0
4	20th December 2006	0 0 0	5 5 5	0 0 1	0 1 0	1	0.85	0
5	11th May 2007	125 44	5 10	0 0	0 0	0	0.02	0
6	27th March 2008	5	5	0	0	1	0.05	0
7	27th May 2008	0 19	5 10	0 1	0 0	0	0.31	3
8	13th September 2008	2	5	0	0	1	0.04	0
9	26th September 2008	29	5	0	0	0	0.04	2
10	28th April 2010	0 82	0 5	0 1	0 0	1	0.01	0
11	8th September 2010	23	5	0	0	0	0.01	0
12	18th March 2012	6	5	0	0	1	0.27	2
13	27th July 2012	0 0 59	5 5 5	0 1 0	0 0 1	1	0.03	0
14	27th July 2012	98	5	0	0	1	0.01	0

Table 6-4: Quality of results, using FOCMEC, HASH and Moment tensor inversion.

Event no.1

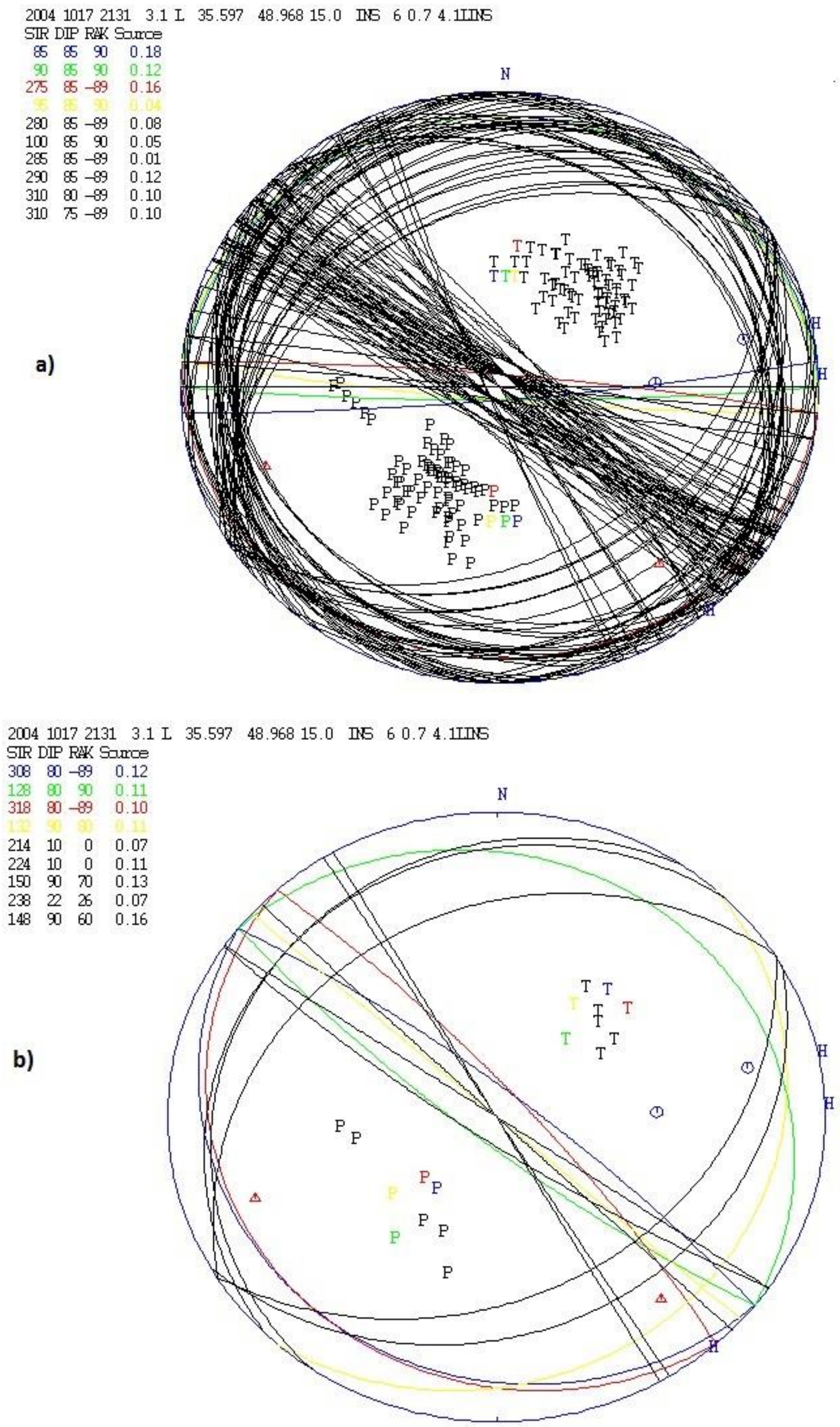

```
2004 1017 2131  3.1 L  35.597  48.968 15.0  INS  6 0.7 4.1LINS
STR DIP RAK Source
 85  85  90   0.18
 90  85  90   0.12
275  85 -89   0.16
 95  85  90   0.04
280  85 -89   0.08
100  85  90   0.05
285  85 -89   0.01
290  85 -89   0.12
310  80 -89   0.10
310  75 -89   0.10
```

```
2004 1017 2131  3.1 L  35.597  48.968 15.0  INS  6 0.7 4.1LINS
STR DIP RAK Source
308  80 -89   0.12
128  80  90   0.11
318  80 -89   0.10
132  90  80   0.11
214  10   0   0.07
224  10   0   0.11
150  90  70   0.13
238  22  26   0.07
148  90  60   0.16
```

Figure 6-8: a) it shows 73 acceptable solutions suggested by FOCMEC program with 5 degree increments in search. b) It shows 9 acceptable solutions suggested by FOCMEC program with 10 degree increments in search.

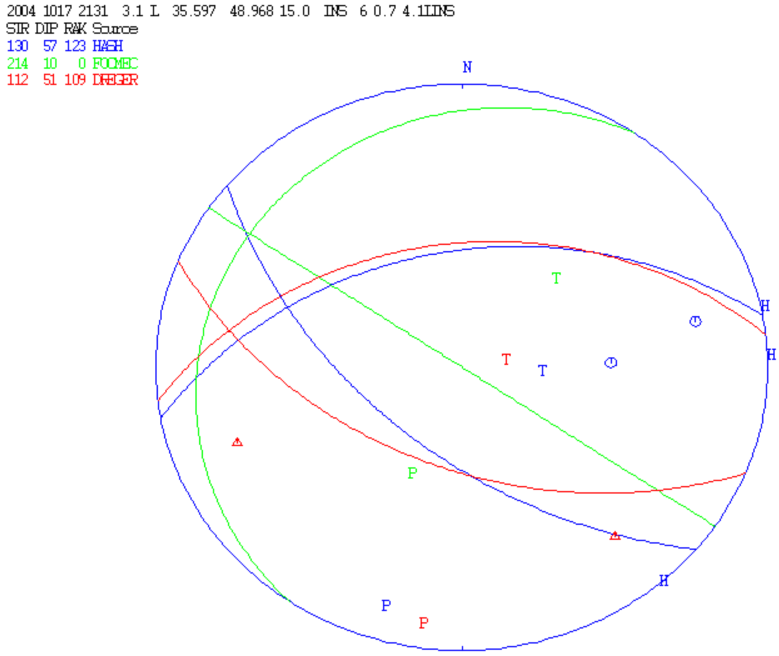

Figure 6-9:: It shows the most likely solution suggested by HASH program (blue), the solution that I have chosen from solutions suggested by FOCMEC program (green) and the solution suggested by moment tensor inversion (red). Compressional motions are shown with blue circles. Dilatational motions are shown with red triangles.

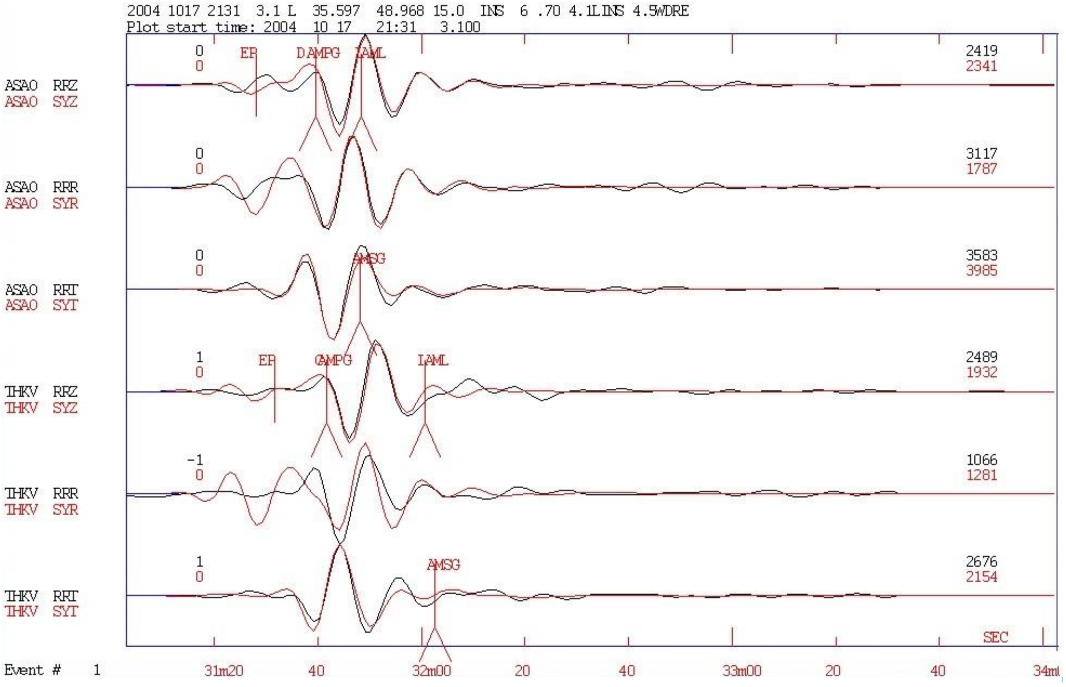

Figure 6-10: Observed (blue) and synthetic (red) waveforms.

Event no.2

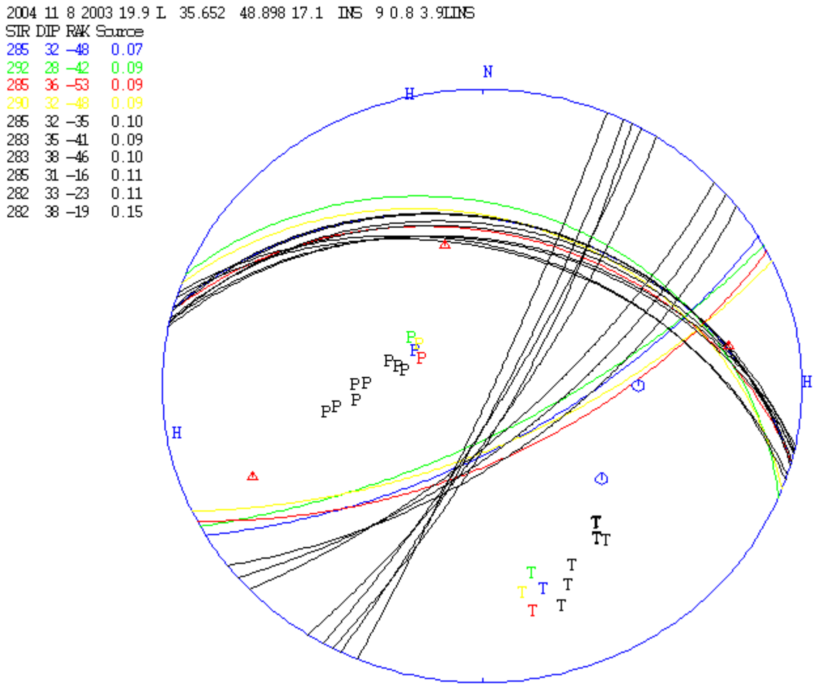

Figure 6-11: It shows 12 acceptable solutions suggested by FOCMEC program with 5 degree increments in search.

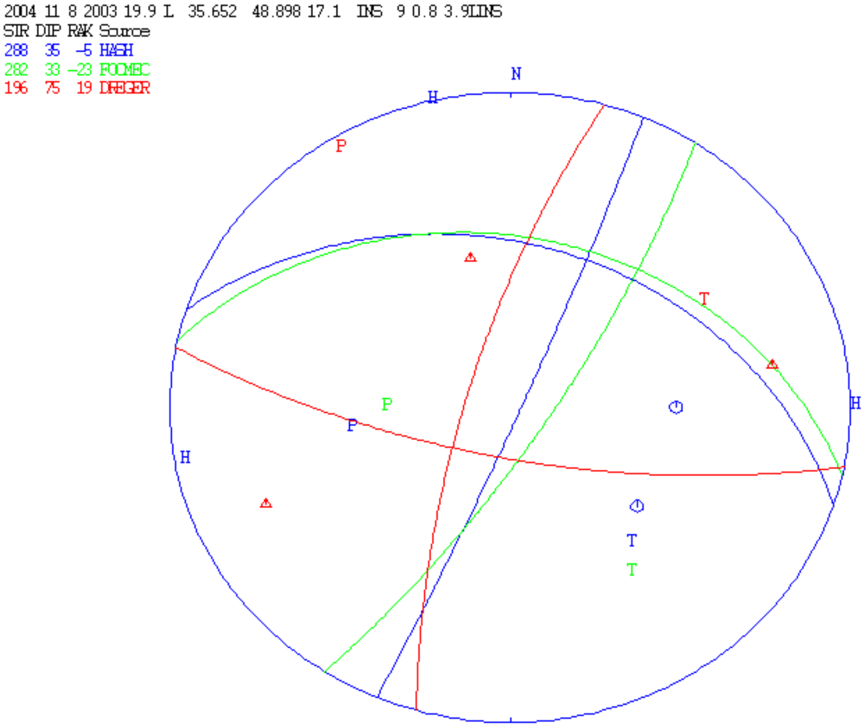

Figure 6-12: It shows the most likely solution suggested by HASH program (blue), the solution that I have chosen from solutions suggested by FOCMEC program (green) and the solution suggested by moment tensor inversion (red). Compressional motions are shown with blue circles. Dilatational motions are shown with red triangles.

Event no.3

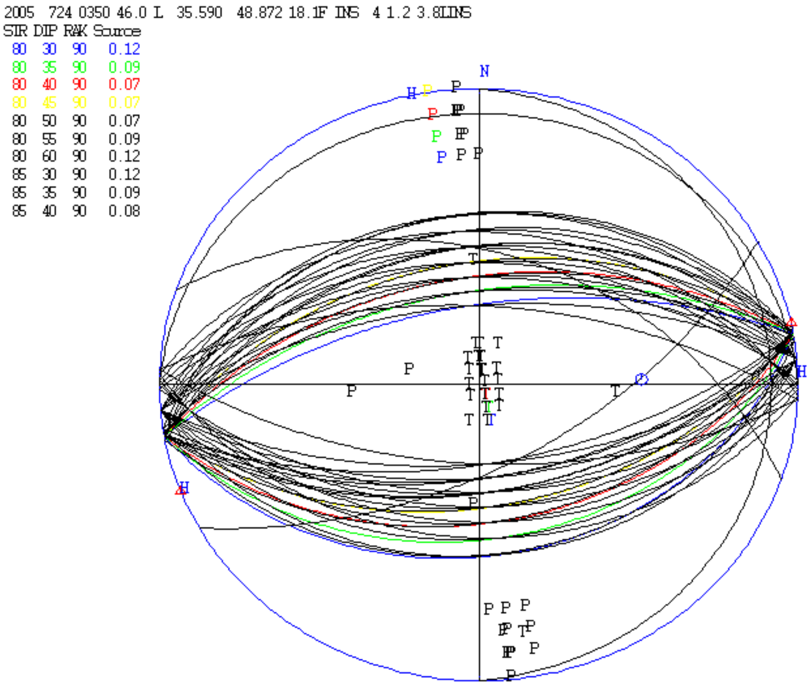

Figure 6-13: It shows 27 acceptable solutions suggested by FOCMEC program with 5 degree increments in search.

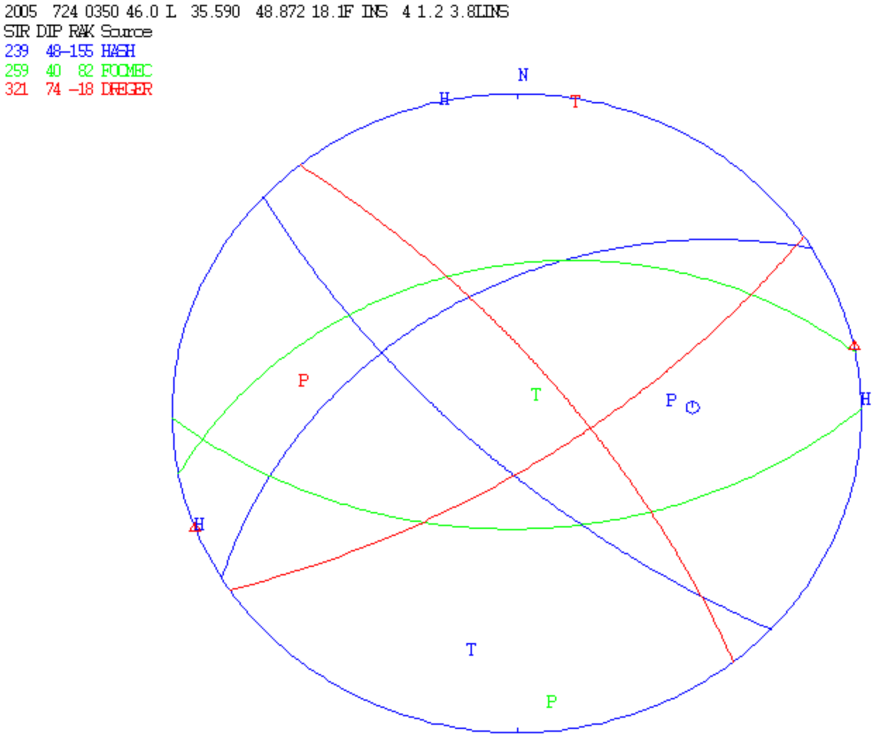

Figure 6-14: It shows the most likely solution suggested by HASH program (blue), the solution that I have chosen from solutions suggested by FOCMEC program (green) and the solution suggested by moment tensor inversion (red). Compressional motions are shown with blue circles. Dilatational motions are shown with red triangles.

Event no.4

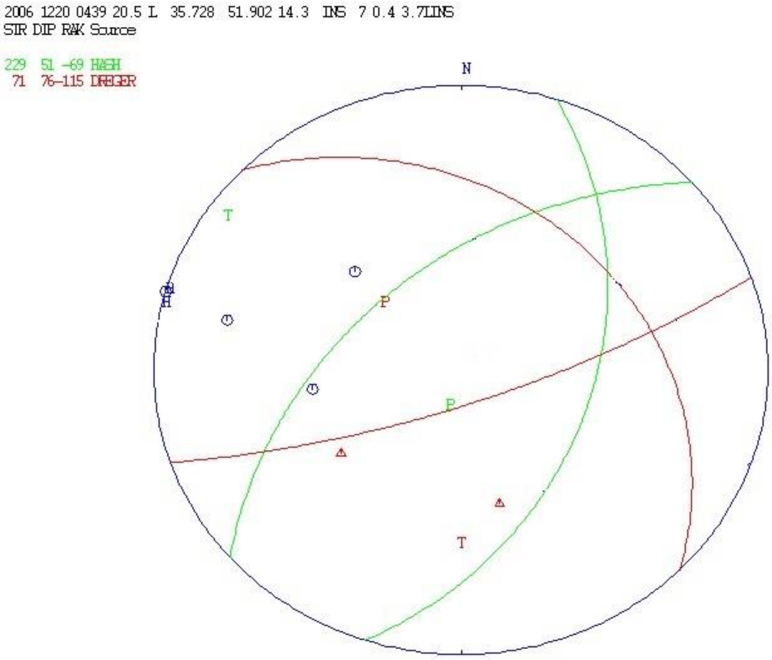

Figure 6-15: It shows the most likely solution suggested by HASH program (green) and the solution suggested by moment tensor inversion (red). Compressional motions are shown with blue circles. Dilatational motions are shown with red triangles.

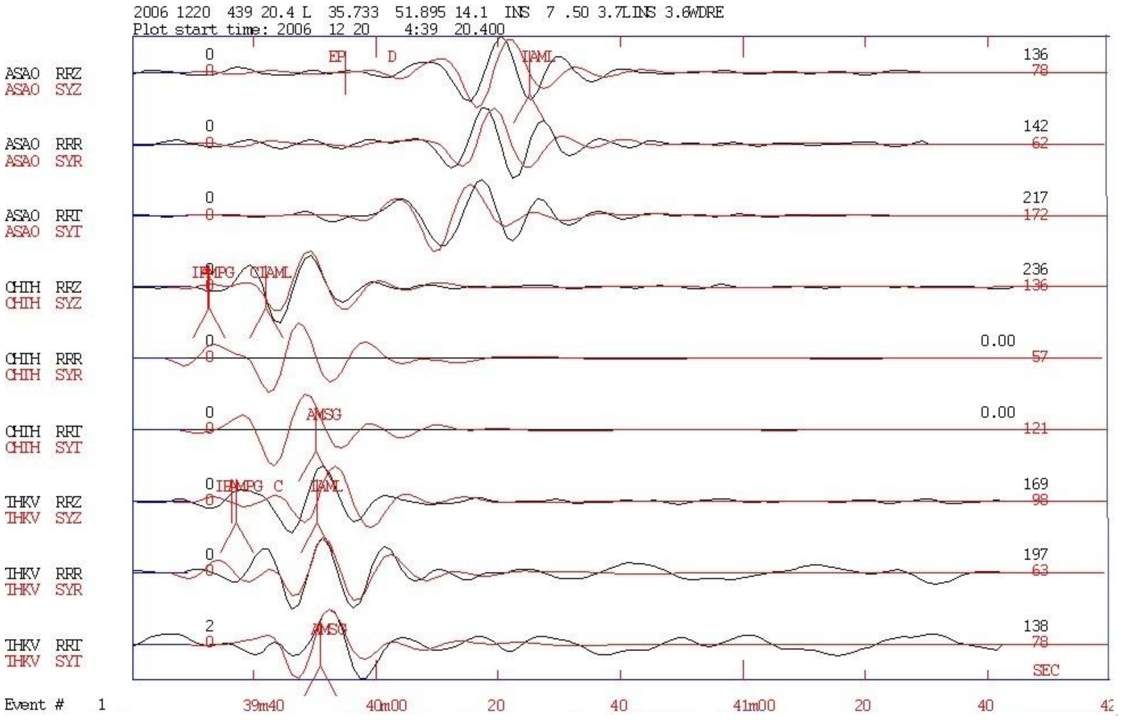

Figure 6-16: Observed (blue) and synthetic (red) waveforms.

Event no.5

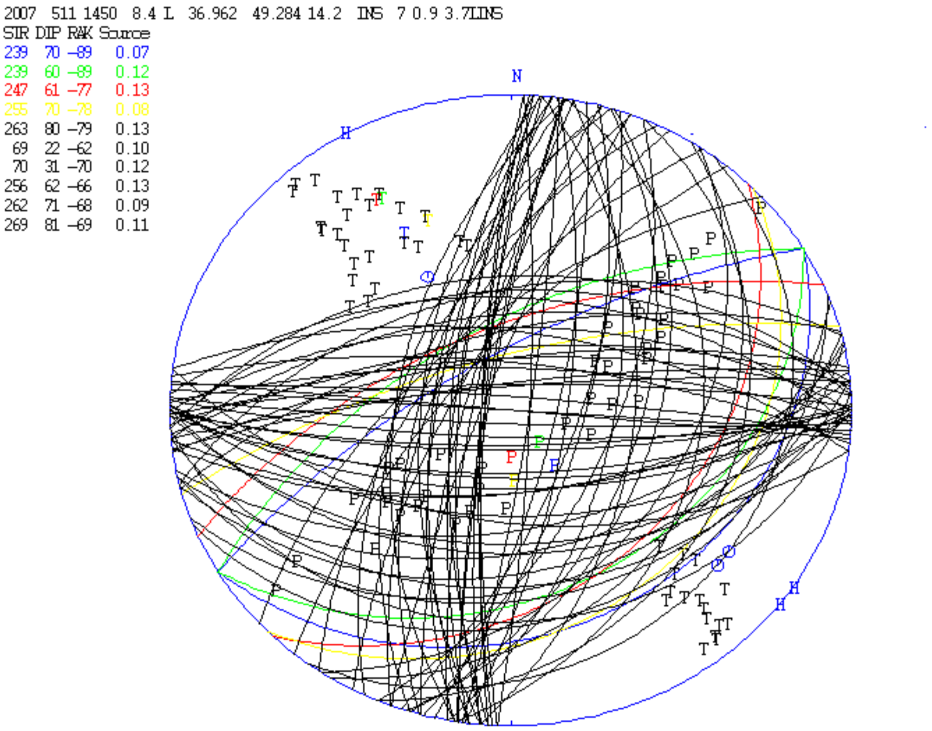

```
2007  511 1450  8.4 L  36.962  49.284 14.2  INS  7 0.9 3.7LINS
STR DIP RAK Source
239  70 -89   0.07
239  60 -89   0.12
247  61 -77   0.13
255  70 -78   0.08
263  80 -79   0.13
 69  22 -62   0.10
 70  31 -70   0.12
256  62 -66   0.13
262  71 -68   0.09
269  81 -69   0.11
```

Figure 6-17: It shows 44 acceptable solutions suggested by FOCMEC program with 10 degree increments in search.

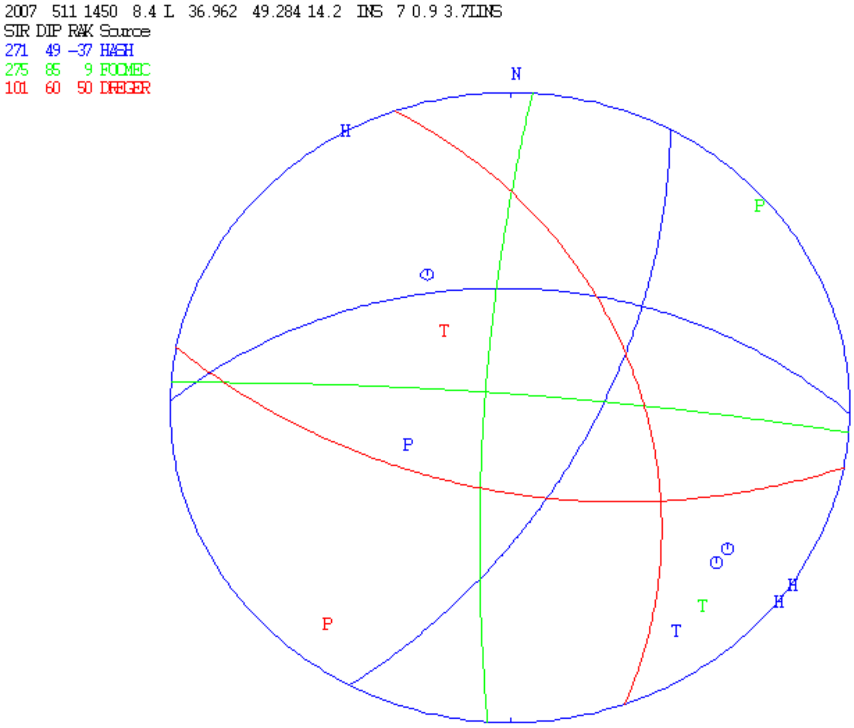

```
2007  511 1450  8.4 L  36.962  49.284 14.2  INS  7 0.9 3.7LINS
STR DIP RAK Source
271  49 -37 HASH
275  85   9 FOCMEC
101  60  50 DREGER
```

Figure 6-18: It shows the most likely solution suggested by HASH program (blue), the solution that I have chosen from solutions suggested by FOCMEC program (green) and the solution suggested by moment tensor inversion (red). Compressional motions are shown with blue circles. Dilatational motions are shown with red triangles.

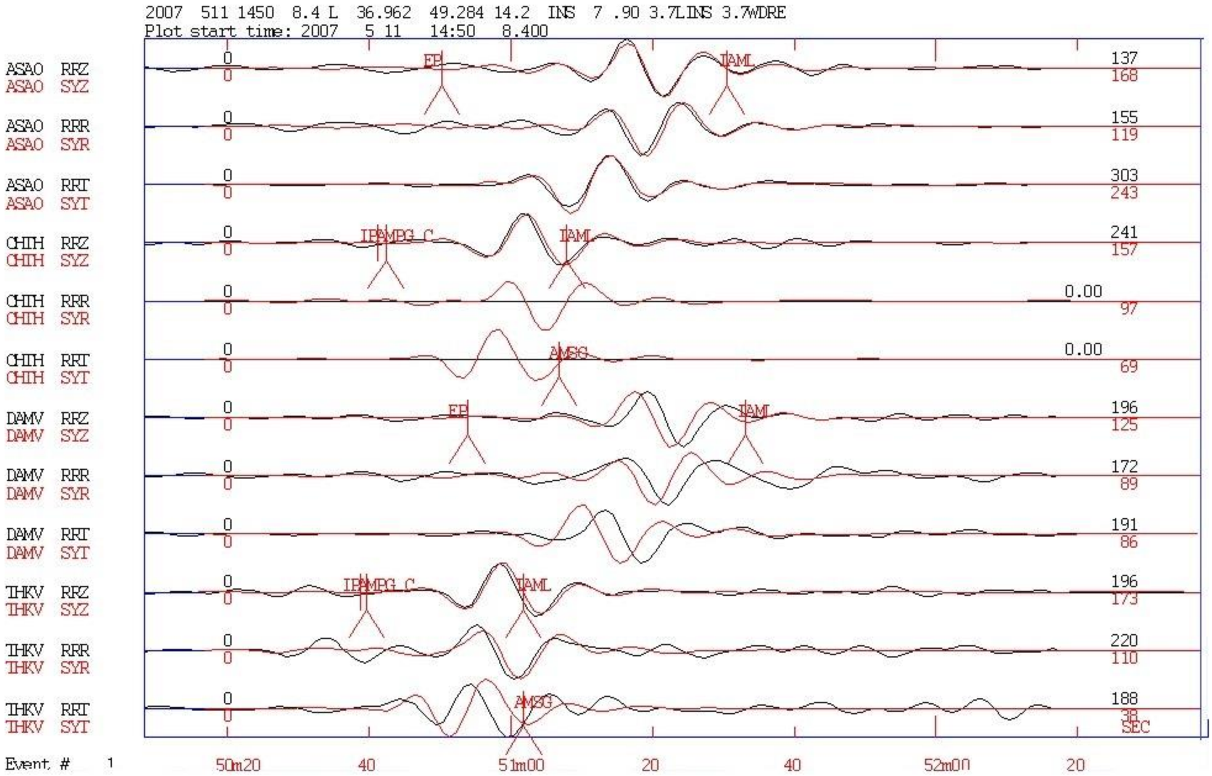

Figure 6-19: Observed (blue) and synthetic (red) waveforms.

Event no.6

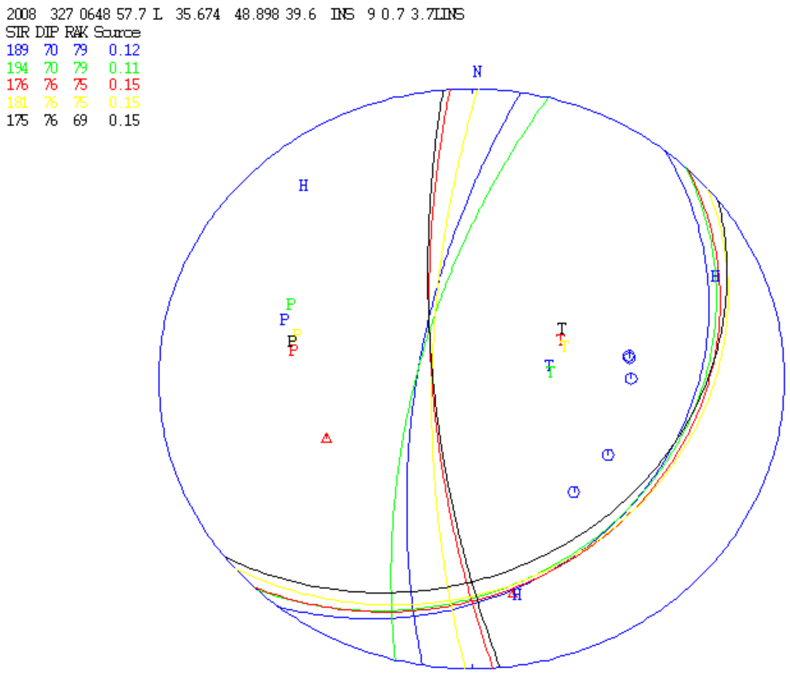

Figure 6-20: It shows 5 acceptable solutions suggested by FOCMEC program with 5 degree increments in search.

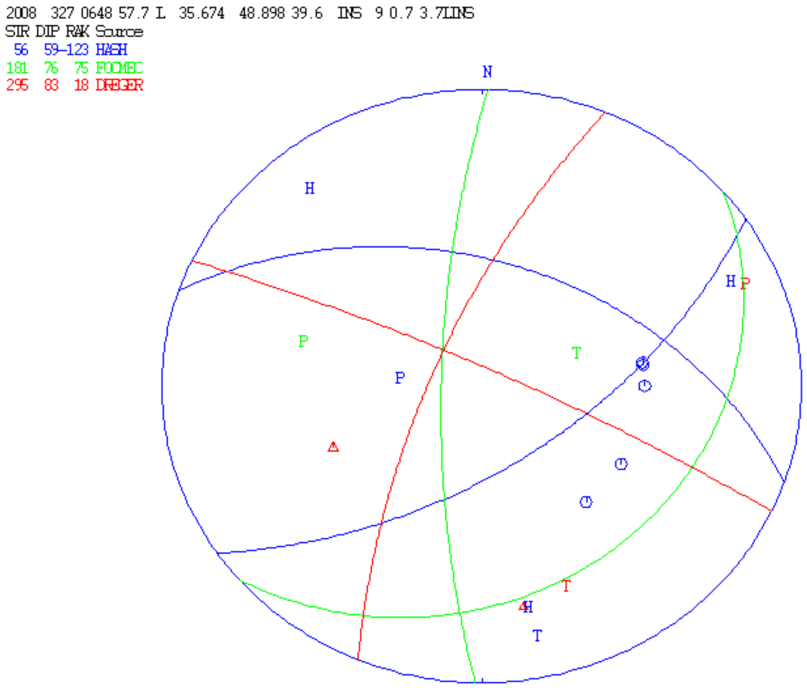

Figure 6-21: It shows the most likely solution suggested by HASH program (blue), the solution that I have chosen from solutions suggested by FOCMEC program (green) and the solution suggested by moment tensor inversion (red). Compressional motions are shown with blue circles. Dilatational motions are shown with red triangles.

Event no.7

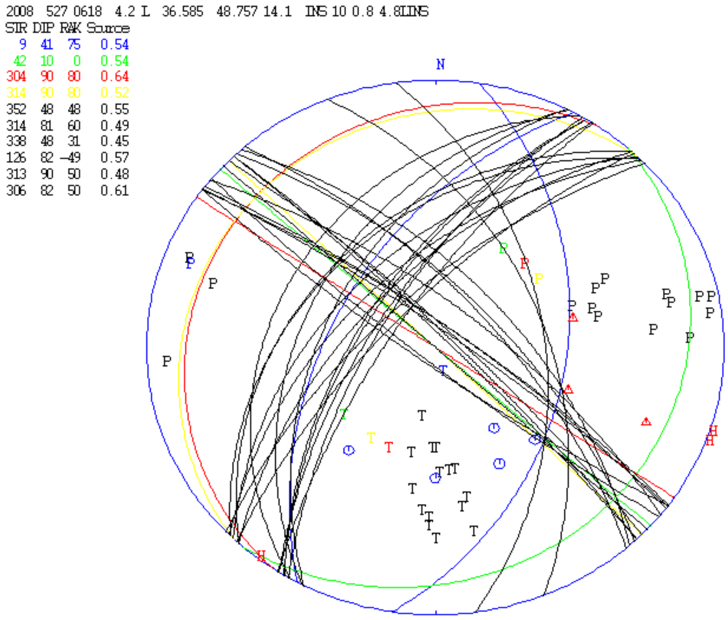

```
2008  527 0618  4.2 L  36.585  48.757 14.1  INS 10 0.8 4.8LINS
STR DIP RAK Score
  9  41  75   0.54
 42  10   0   0.54
304  90  80   0.64
314  90  80   0.52
352  48  48   0.55
314  81  60   0.49
338  48  31   0.45
126  82 -49   0.57
313  90  50   0.48
306  82  50   0.61
```

Figure 6-22: It shows 19 acceptable solutions suggested by FOCMEC program with 10 degree increments in search.

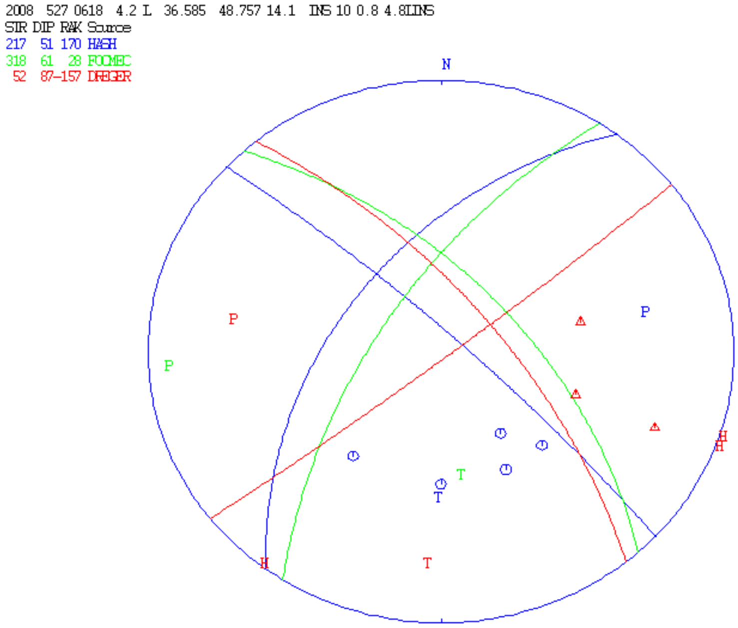

```
2008  527 0618  4.2 L  36.585  48.757 14.1  INS 10 0.8 4.8LINS
STR DIP RAK Source
217  51 170 HASH
318  61  28 FOCMEC
 52  87-157 DREGER
```

Figure 6-23: It shows the most likely solution suggested by HASH program (blue), the solution that I have chosen from solutions suggested by FOCMEC program (green) and the solution suggested by moment tensor inversion (red). Compressional motions are shown with blue circles. Dilatational motions are shown with red triangles.

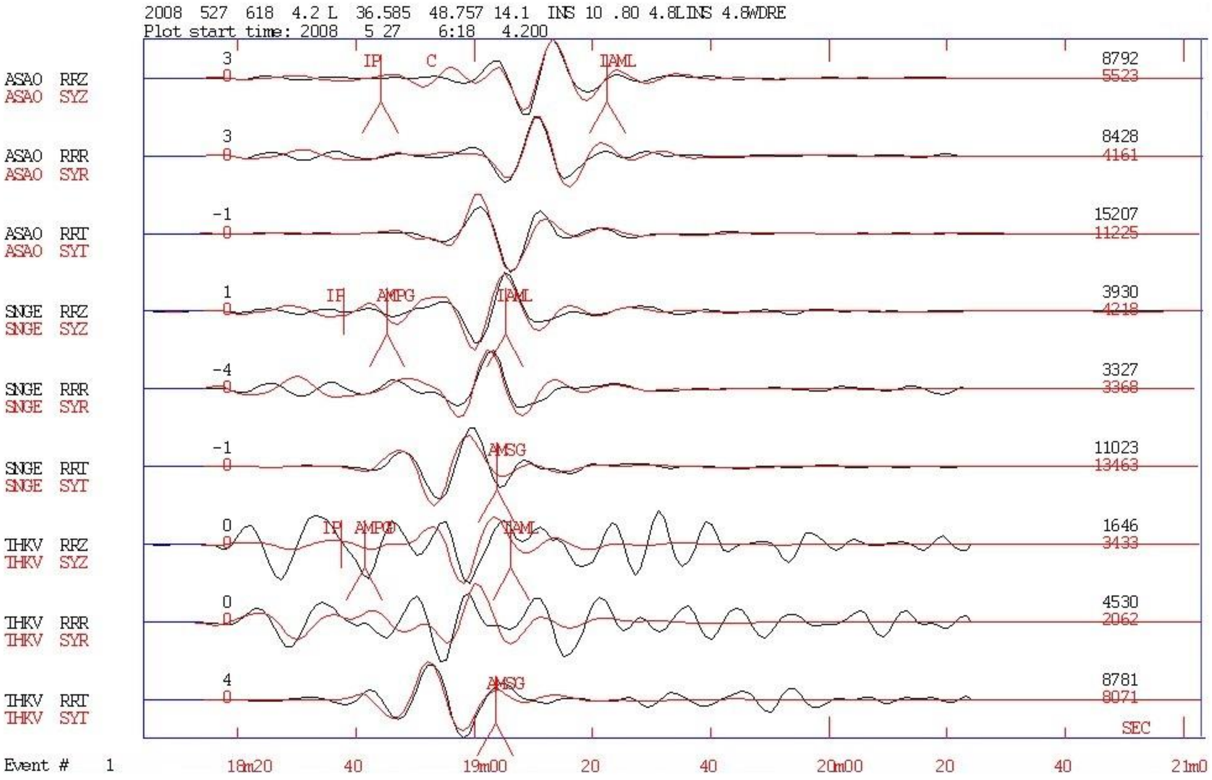

Figure 6-24: Observed (blue) and synthetic (red) waveforms.

Event no.8

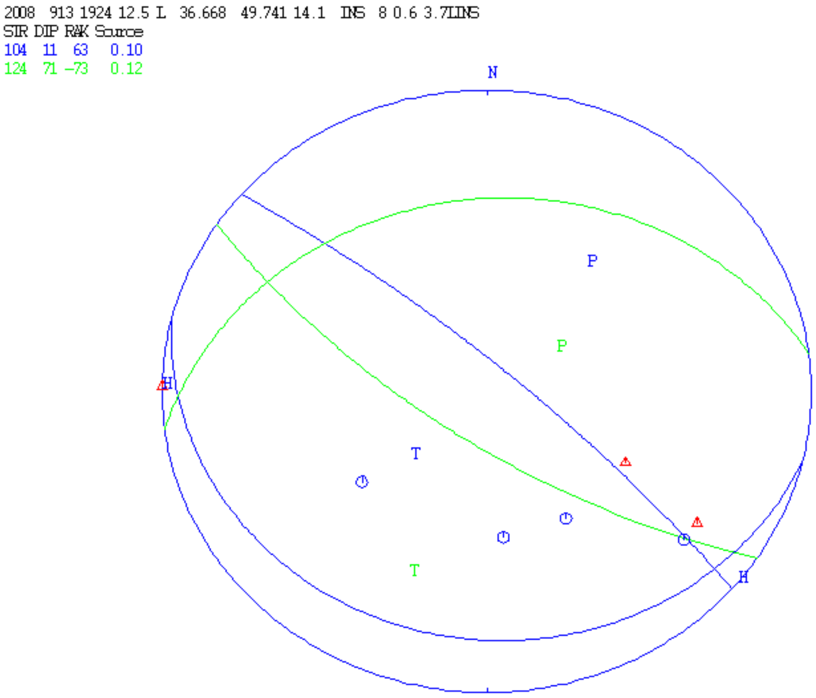

Figure 6-25: It shows 2 acceptable solutions suggested by FOCMEC program with 5 degree increments in search.

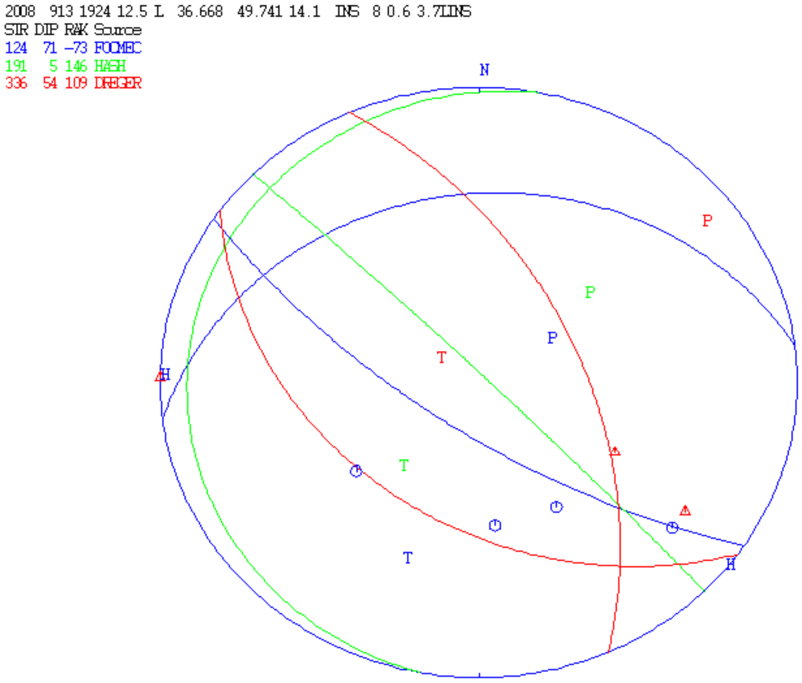

Figure 6-26: It shows the most likely solution suggested by HASH program (blue), the solution that I have chosen from solutions suggested by FOCMEC program (green) and the solution suggested by moment tensor inversion (red). Compressional motions are shown with blue circles. Dilatational motions are shown with red triangles.

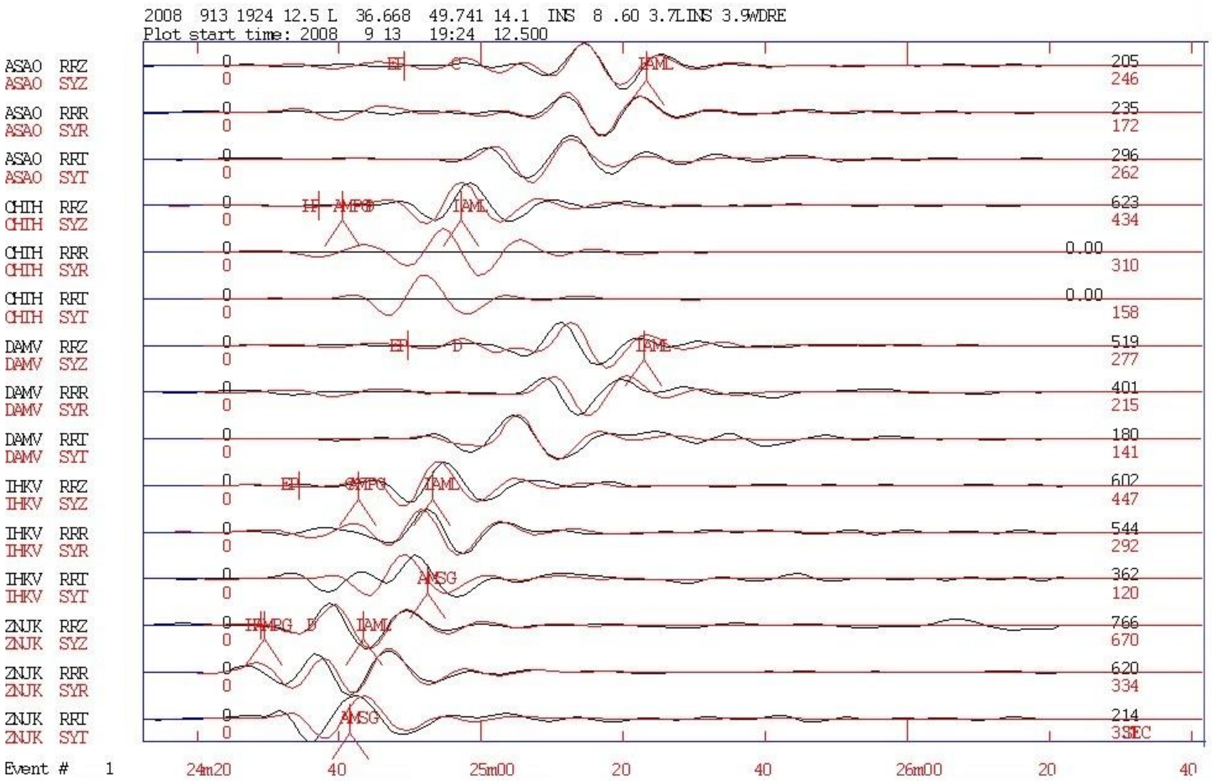

Figure 6-27: Observed (blue) and synthetic (red) waveforms.

Event no.9

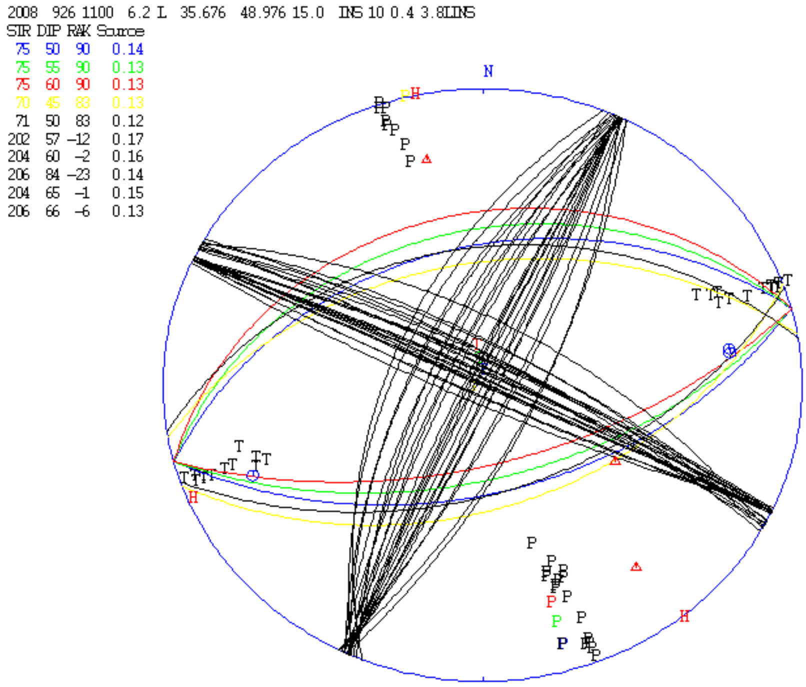

```
2008  926 1100  6.2 L  35.676  48.976 15.0  INS 10 0.4 3.8LINS
STR DIP RAK Source
 75  50  90   0.14
 75  55  90   0.13
 75  60  90   0.13
 70  45  83   0.13
 71  50  83   0.12
202  57 -12   0.17
204  60  -2   0.16
206  84 -23   0.14
204  65  -1   0.15
206  66  -6   0.13
```

Figure 6-28: It shows 29 acceptable solutions suggested by FOCMEC program with 5 degree increments in search.

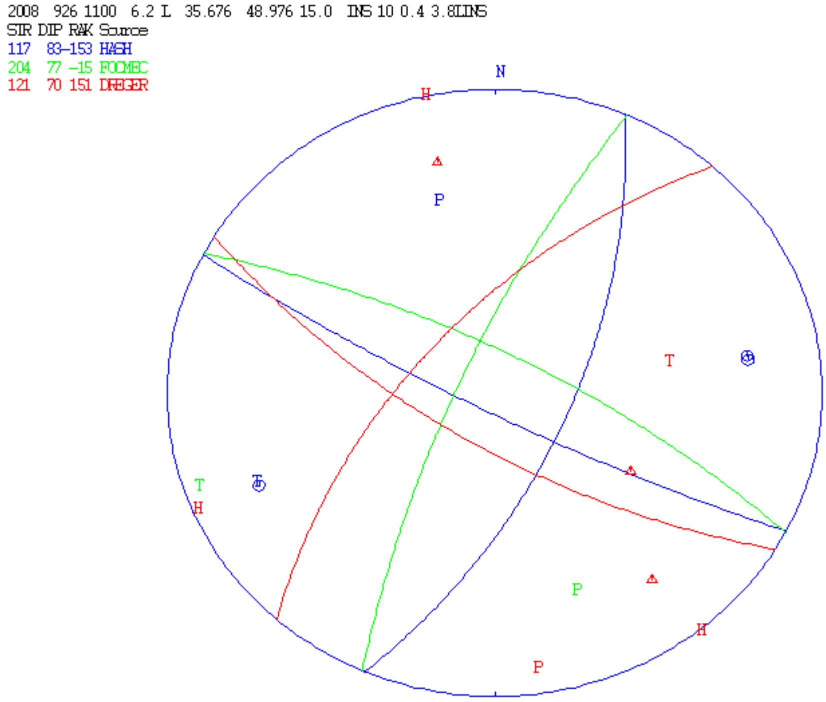

```
2008  926 1100  6.2 L  35.676  48.976 15.0  INS 10 0.4 3.8LINS
STR DIP RAK Source
117  83-153 HASH
204  77 -15 FOCMEC
121  70 151 DREGER
```

Figure 6-29: It shows the most likely solution suggested by HASH program (blue), the solution that I have chosen from solutions suggested by FOCMEC program (green) and the solution suggested by moment tensor inversion (red). Compressional motions are shown with blue circles. Dilatational motions are shown with red triangles.

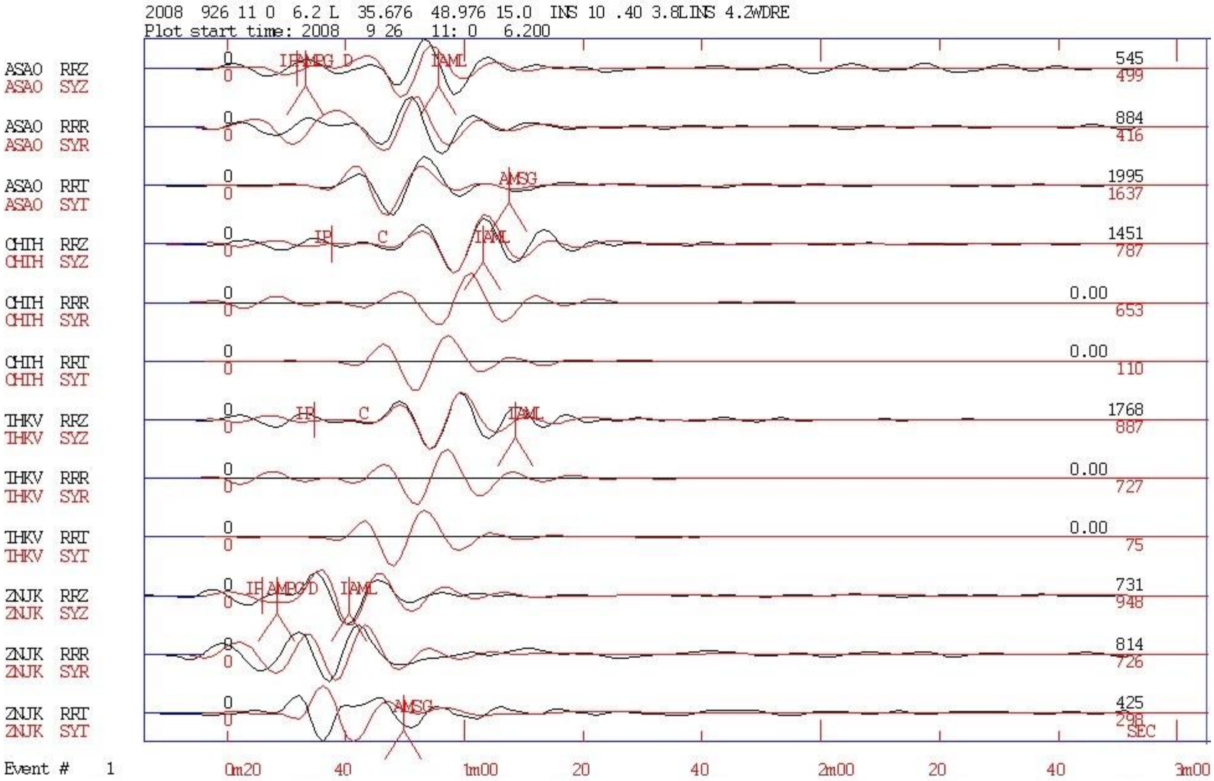

Figure 6-30: Observed (blue) and synthetic (red) waveforms.

Event no.10

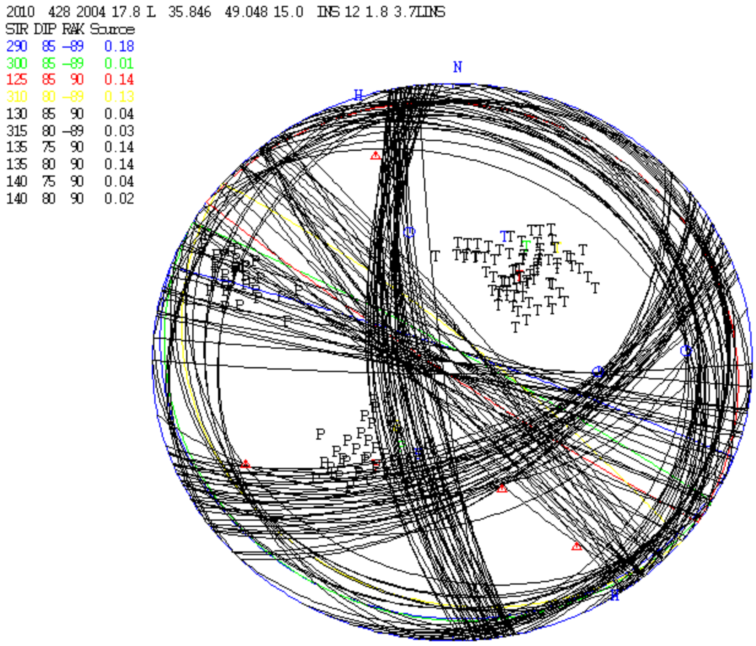

```
2010   428 2004 17.8 L  35.846   49.048 15.0   INS 12 1.8 3.7LINS
STR DIP RAK Source
290  85 -89    0.18
300  85 -89    0.01
125  85  90    0.14
310  80 -89    0.13
130  85  90    0.04
315  80 -89    0.03
135  75  90    0.14
135  80  90    0.14
140  75  90    0.04
140  80  90    0.02
```

Figure 6-31: It shows 82 acceptable solutions suggested by FOCMEC program with 5 degree increments in search.

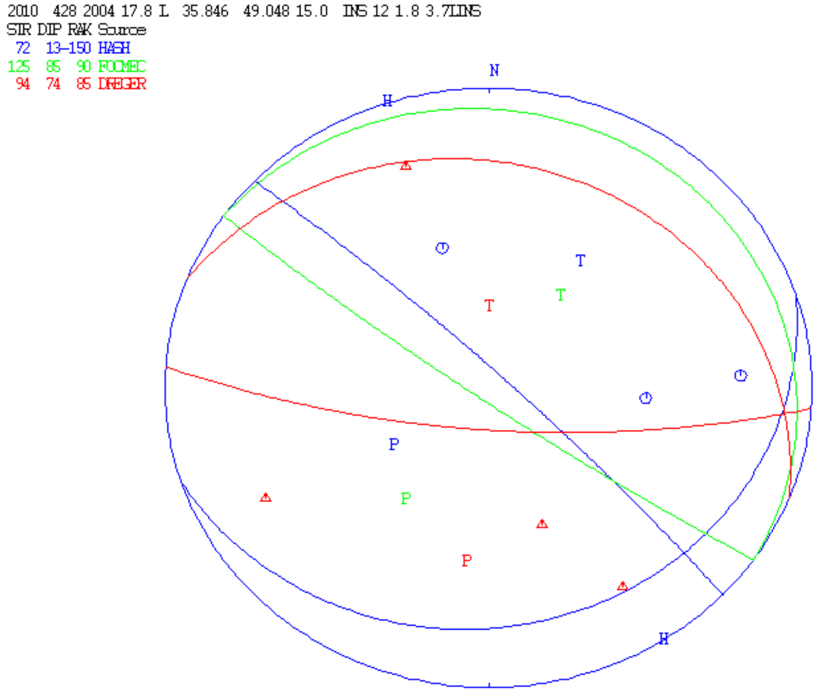

```
2010   428 2004 17.8 L  35.846   49.048 15.0   INS 12 1.8 3.7LINS
STR DIP RAK Source
 72  13-150 HASH
125  85  90 FOCMEC
 94  74  85 DREGER
```

Figure 6-32: It shows the most likely solution suggested by HASH program (blue), the solution that I have chosen from solutions suggested by FOCMEC program (green) and the solution suggested by moment tensor inversion (red). Compressional motions are shown with blue circles. Dilatational motions are shown with red triangles.

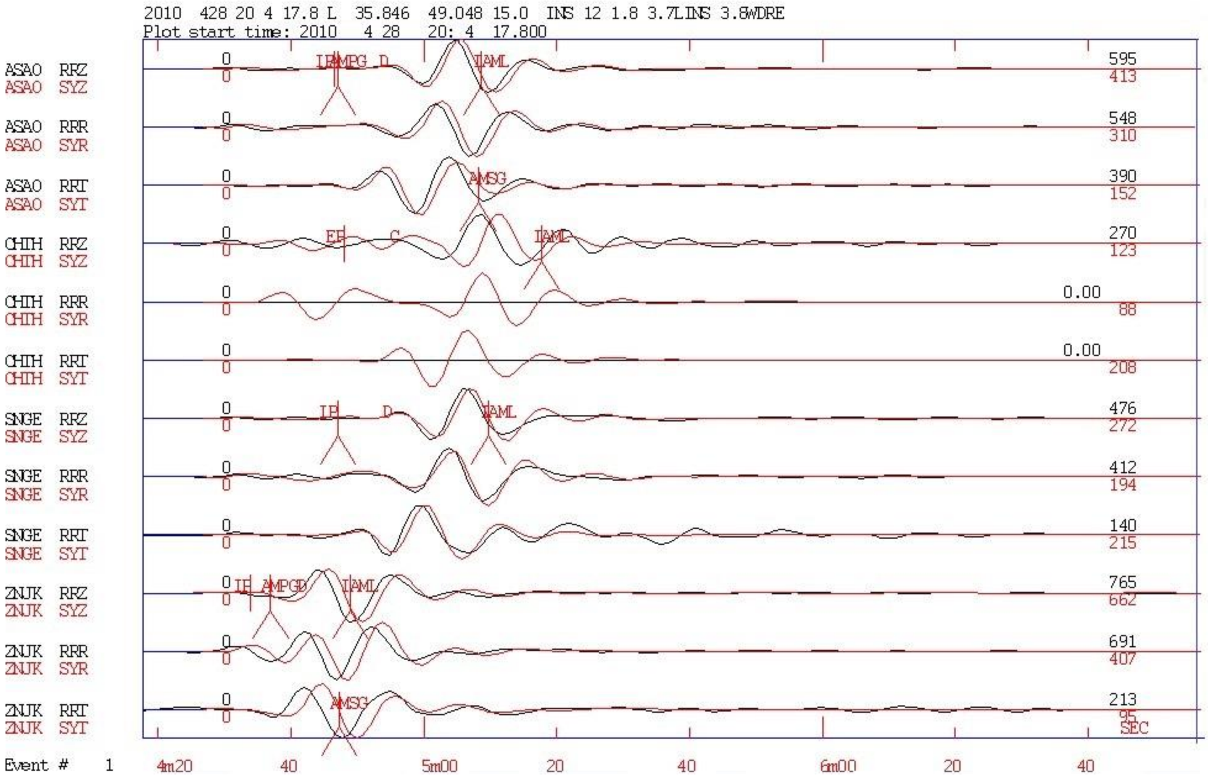

Figure 6-33: Observed (blue) and synthetic (red) waveforms.

Event no.11

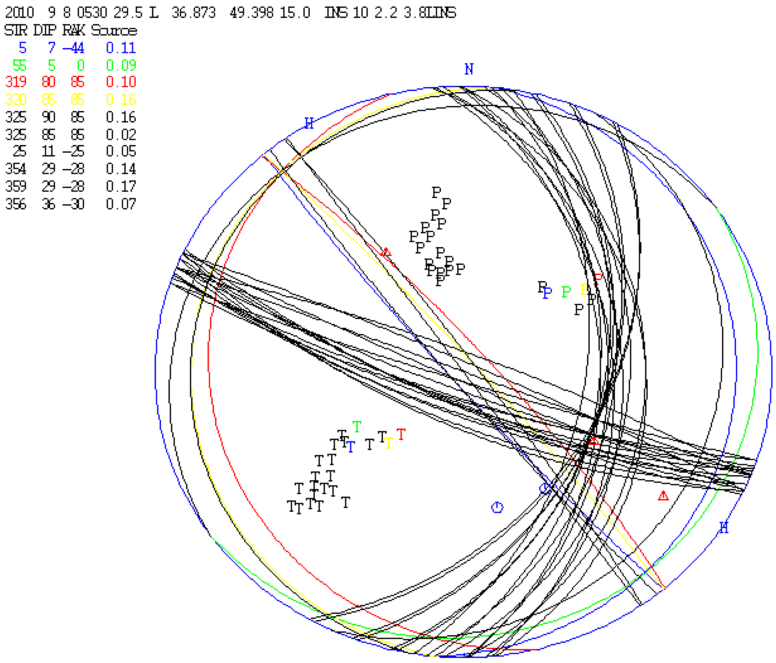

```
2010  9 8 0530 29.5 L  36.873  49.398 15.0  INS 10 2.2 3.8LINS
STR DIP RAK Source
  5   7 -44   0.11
 55   5   0   0.09
319  80  85   0.10
320  85  85   0.16
325  90  85   0.16
325  85  85   0.02
 25  11 -25   0.05
354  29 -28   0.14
359  29 -28   0.17
356  36 -30   0.07
```

Figure 6-34: It shows 23 acceptable solutions suggested by FOCMEC program with 5 degree increments in search.

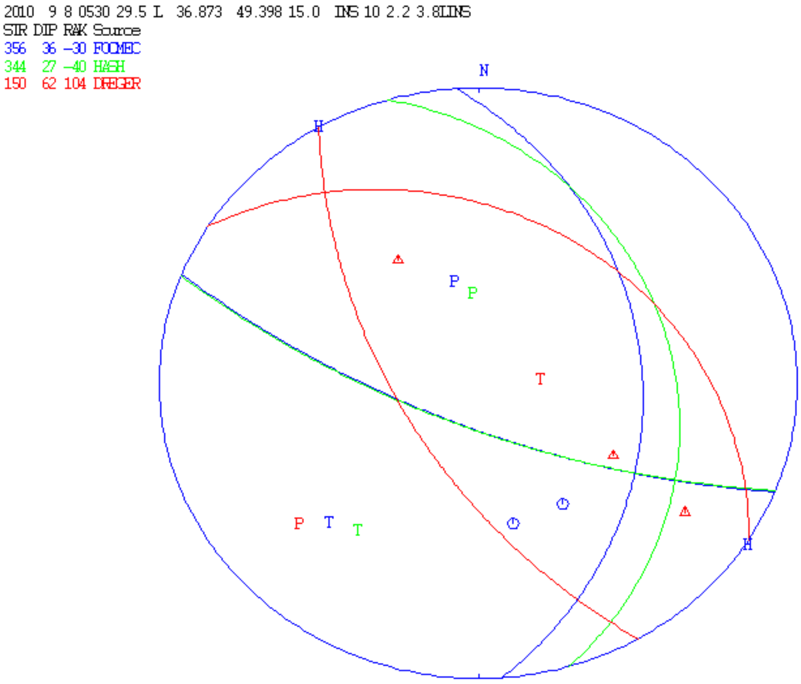

```
2010  9 8 0530 29.5 L  36.873  49.398 15.0  INS 10 2.2 3.8LINS
STR DIP RAK Source
356  36 -30 FOCMEC
344  27 -40 HASH
150  62 104 DREGER
```

Figure 6-35: It shows the most likely solution suggested by HASH program (blue), the solution that I have chosen from solutions suggested by FOCMEC program (green) and the solution suggested by moment tensor inversion (red). Compressional motions are shown with blue circles. Dilatational motions are shown with red triangles.

Event no.12

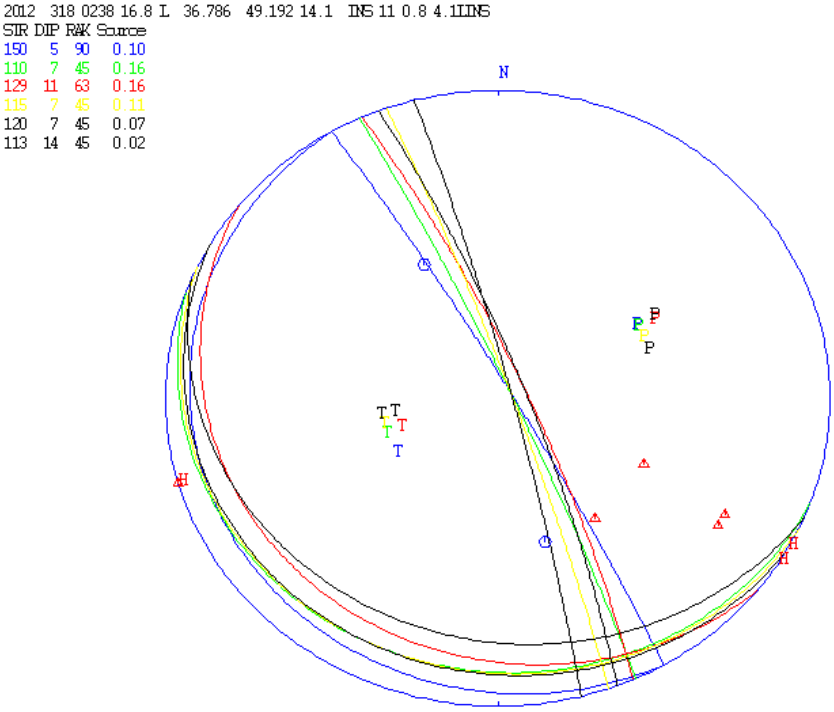

```
2012  318 0238 16.8 L  36.786  49.192 14.1  INS 11 0.8 4.1LINS
STR DIP RAK Source
150   5  90   0.10
110   7  45   0.16
129  11  63   0.16
115   7  45   0.11
120   7  45   0.07
113  14  45   0.02
```

Figure 6-36: It shows 6 acceptable solutions suggested by FOCMEC program with 5 degree increments in search.

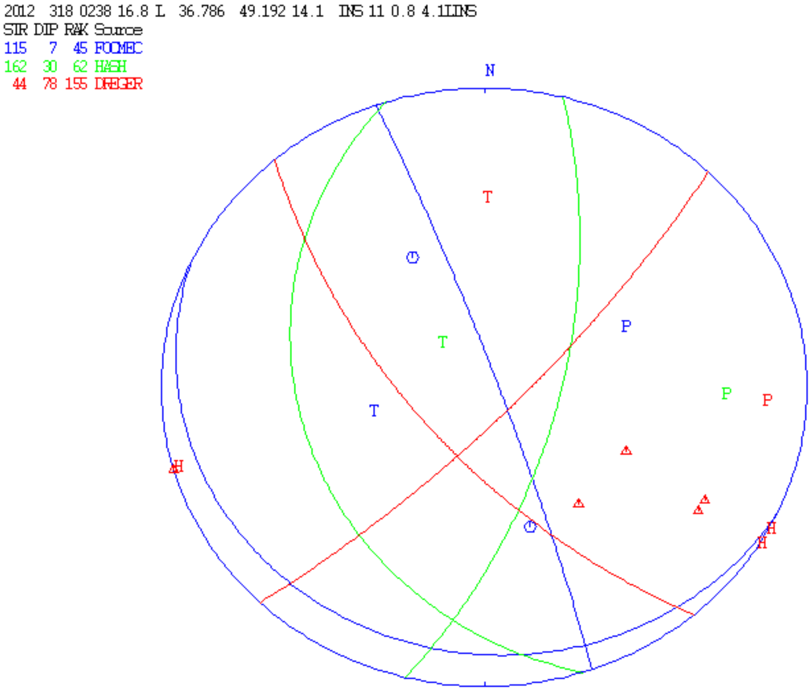

```
2012  318 0238 16.8 L  36.786  49.192 14.1  INS 11 0.8 4.1LINS
STR DIP RAK Source
115   7  45 FOCMEC
162  30  62 HASH
 44  78 155 DREGER
```

Figure 6-37: It shows the most likely solution suggested by HASH program (green), the solution that I have chosen from solutions suggested by FOCMEC program (blue) and the solution suggested by moment tensor inversion (red). Compressional motions are shown with blue circles. Dilatational motions are shown with red triangles.

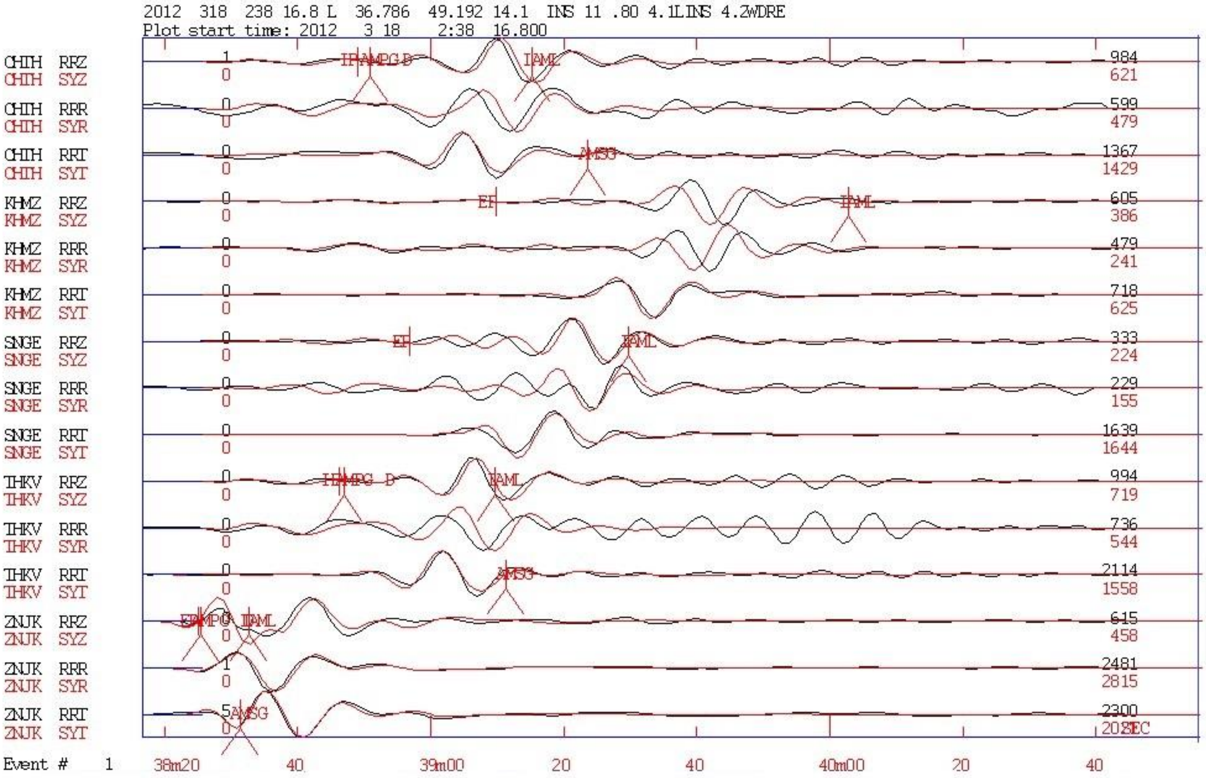

Figure 6-38: Observed (blue) and synthetic (red) waveforms.

Event no.13

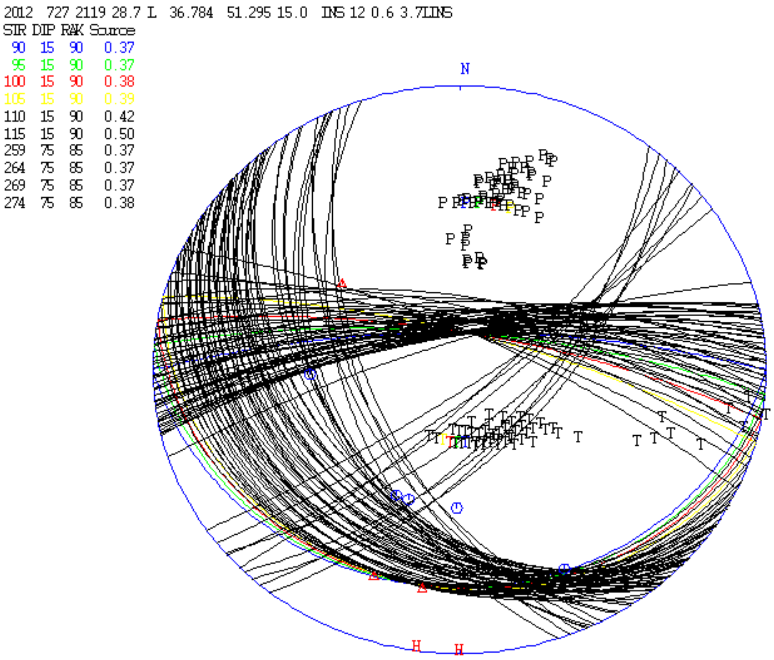

```
2012  727 2119 28.7 L  36.784  51.295 15.0  INS 12 0.6 3.7LINS
STR DIP RAK Source
 90  15  90   0.37
 95  15  90   0.37
100  15  90   0.38
105  15  90   0.39
110  15  90   0.42
115  15  90   0.50
259  75  85   0.37
264  75  85   0.37
269  75  85   0.37
274  75  85   0.38
```

Figure 6-39: It shows 59 acceptable solutions suggested by FOCMEC program with 5 degree increments in search.

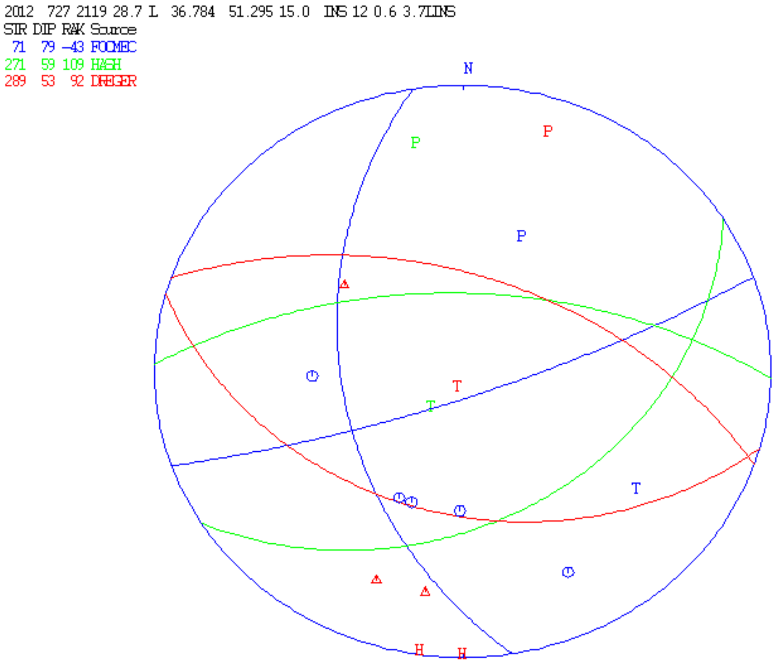

```
2012  727 2119 28.7 L  36.784  51.295 15.0  INS 12 0.6 3.7LINS
STR DIP RAK Source
 71  79 -43 FOCMEC
271  59 109 HASH
289  53  92 DREGER
```

Figure 6-40: It shows the most likely solution suggested by HASH program (green), the solution that I have chosen from solutions suggested by FOCMEC program (blue) and the solution suggested by moment tensor inversion (red). Compressional motions are shown with blue circles. Dilatational motions are shown with red triangles.

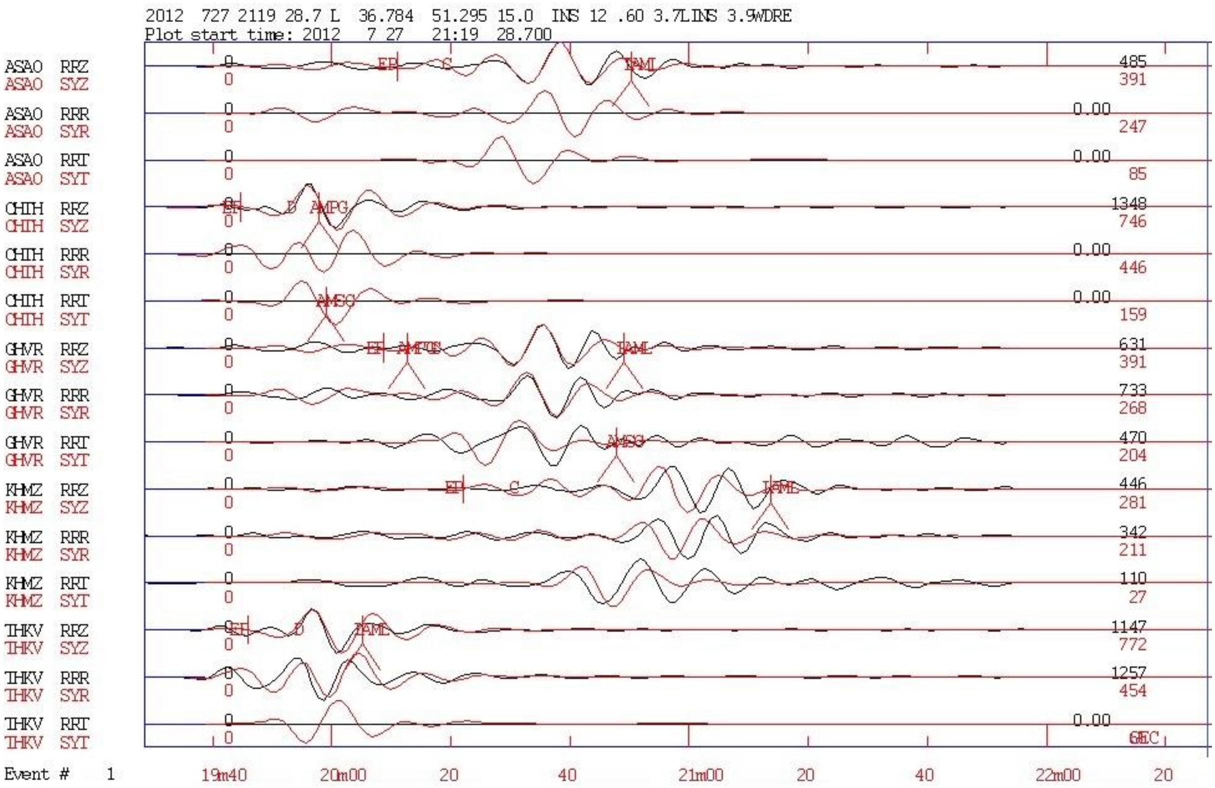

Figure 6-41: Observed (blue) and synthetic (red) waveforms.

Event no.14

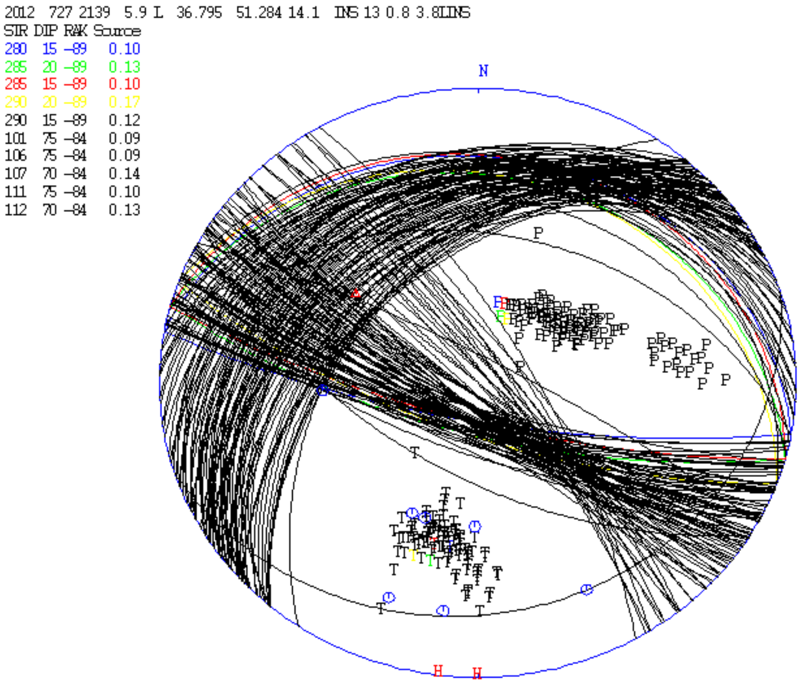

```
2012  727 2139  5.9 L  36.795  51.284 14.1  INS 13 0.8 3.8LINS
STR DIP RAK Source
280  15 -89    0.10
285  20 -89    0.13
285  15 -89    0.10
290  20 -89    0.17
290  15 -89    0.12
101  75 -84    0.09
106  75 -84    0.09
107  70 -84    0.14
111  75 -84    0.10
112  70 -84    0.13
```

Figure 6-42: It shows 98 acceptable solutions suggested by FOCMEC program with 5 degree increments in search.

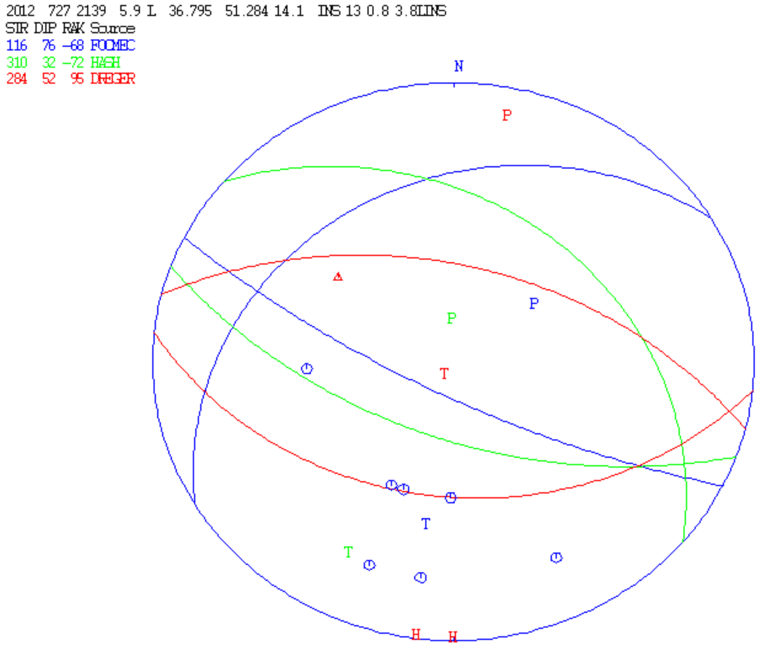

```
2012  727 2139  5.9 L  36.795  51.284 14.1  INS 13 0.8 3.8LINS
STR DIP RAK Source
116  76 -68 FOCMEC
310  32 -72 HASH
284  52  95 DREGER
```

Figure 6-43: It shows the most likely solution suggested by HASH program (green), the solution that I have chosen from solutions suggested by FOCMEC program (blue) and the solution suggested by moment tensor inversion (red). Compressional motions are shown with blue circles. Dilatational motions are shown with red triangles.

7 Discussion

For this thesis I went to Iran for two weeks to get local seismic data in the Alborz Mountains from IIEES. I used seismic data to do a comprehensive study of earthquake activity in the selected area with latitude range 35.5°-37° and longitude range 48°-52°. For this purpose I processed data in a number of steps and I attempted to extract information from my data set as much as possible though the number of stations in the study area and quality of the stations was limited.

7.1 Location of events

I identified the first P-wave and Sg phase on my waveforms to get the locations of events in my data set and used the travel times of the phases to develop velocity models, which should give better location, but also allow comparison of existing models and conclusion on crustal thickness.

7.1.1 Comparison of existing models and conclusion on crustal thickness

To locate the earthquakes in my data set I identified the first P-wave which could be either Pn- or Pg-phase, but identifying the first S-wave was a bit tricky as I could not observe Sn-phase in my waveforms and because of that, I identified S-waves as Sg-phases (Figure 4-2). This observation was consistent with IIEES observations. According to the IIEES at distances less than 200-250 km Sn phases cannot be recorded and it is also very difficult to identify Sn at distances greater than 500 km. However, the computed travel time-distance diagrams using model 1 (from IIEES) will not show that (Figure 4-7).

This would mean that the current IIEES model does not work for S-wave although model 1(from IIEES) together with the model 2 [Abbassi et al., 2010] provide a smaller mean rms value for inversion for single earthquake location method compared to the other two velocity models (model 3 and model 4) (Table 4-6).

The computed travel time-distance diagrams using model 2 [Abbassi et al., 2010] (Figure 4-8) despite other models is more consistent with our observations as it shows that the direct and refracted waves are almost identical until ~ 270 km and Sg-phases are shown where I have identified Sg-phases. Model 2 also gives the lowest mean rms value for inversion for single earthquake location method. This would mean that model 2 describes structures in the Alborz Mountains better compared to other velocity models that were in use. In this model the crust consists of five layers, where the top two layers are sedimentary layers with a thickness of 3 km and 4 km. It also represents the Moho is at a depth of 58±2 km (Table 4-3, Figure 4-4)

7.1.2 Provide new velocity models by improving the existing velocity model

I'selected a data set consisting of 126 earthquakes which could be located with at least 5 P observations, since S observations have not been used as they are likely secondary S arrivals which are not handled properly by the VELEST code.

I used simultaneous inversion to locate data set and improve the four existing initial velocity models by using the travel times of the phases. I would also compare the four new models to see which of the models gives the smallest mean rms value for the entire dataset and present it as a new velocity model for the study area.

Comparison of the RMS residual after this simultaneous inversion shows that the new models provide smaller RMS residual compared to the initial models. To check the results from simultaneous inversion I ran the hypocenter program for the new models to see how the mean rms values (Table 4-6, Table 4-8) for the entire data set are changed. Comparison of mean rms values shows that except for model 2, that initial models have improved and the initial model 2 still works better compared to the three new models. This result was not what was expected; Therefore, I have examined the results a bit more by choosing a smaller and better data set, adding the station correction and exclude S-phases from all datasets as they were not included in the calculation of the new models, but I could not get a clear understanding of the problem. Including S-phases in the inversion would help, but that would require a modification of the code, which was outside the scope of this thesis.

In this thesis I improved the three initial models for location with P-phases only, but without using S in the inversion, cannot introduce a new model that works better for this study area and more work is needed.

7.1.3 Seismicity distribution

We get less error in location of earthquakes if the velocity model used in locating is close to the true model. In addition, in order to locate an event one needs to identify seismic phases on at least three seismic stations [Havskov and Ottemoller, 2010] and use of the even more stations will increase accuracy in earthquake location. As Table 7-1 shows 58 of events are located using the minimum requirement number of station in locating. This means that accuracy of location for these earthquakes is less compared to other earthquakes.

Number of stations	3	4	5	6	7	8	9	10	12	13
Number of events	58	87	91	59	42	36	14	7	2	3

Table 7-1: Overview of the number of stations used for locating of event.

Seismicity map which is a result of locating of my data set shows that the seismic activities are concentrated in four zones: Along coast of the Caspian Sea, along the Rudbar fault, where the earthquake of 1962 September 1 has occurred and the eastern part of Mosha fault which includes 42, 36, 58 and 24 events, respectively (Figure 3-2).

Locating of the events show that the depth of the most of earthquakes (364 events) is in the range between 10 and 20 km (Figure 3-6). This means that the earthquakes are in the upper crust and the lower crust is mostly aseismic. However, we see clustering at depth around a layer interface at 15 km depth.

Most of seismic activities along the Rudbar fault are located in an area between the Kabateh and Zard-Goli segments which was not ruptured during the Rudbar earthquake and at the eastern end of Rudbar fault. Distribution and depth of earthquakes along the Rudbar fault are similar to a microearthquake survey eight years after the Rudbar earthquake (1998) which was over seven weeks [*Berberian and Walker*, 2010]. In this microearthquake survey ~ 400 events were recorded. Most of them were located on Kabateh and Zard-Goli segments with the depth range between 8 and 16 km. These observations are consistent with coulomb stress distribution after the 1990 Rudbar mainshock (Figure 2-4) which shows a positive Coulomb failure stress in those areas where seismicity is higher. This would mean that Rudbar fault is an active left-lateral strike-slip fault and it may continue eastward in future.

In seismicity map I could see that 58 events were clustered in the area where the earthquake of 1962 September 1 with M = 7.2 has occurred [*Ambraseys and Melville*, 2005] (Figure 3-2). I did not have enough information to see what's going on there, but I think this area could be a subject for further studies as density of seismic activity is high where it has experienced an earthquake of large magnitude earlier.

7.2 Magnitude of events

I read amplitudes on vertical- and horizontal components to develop magnitude scale and compute magnitudes; I also made vertical to horizontal comparison before developing a magnitude scale for study area which shows horizontal components are 1.48 larger than amplitudes on vertical components on average.

In calculation of the new M_L scale I used amplitude readings on horizontal components, since they are larger than vertical components. Calculated standard deviation of all magnitudes (Table 5-6) and plotting M_L residuals of events (Figure 5-1) shows that the new M_L scale using horizontal components works slightly better for the study area compared with Hutton and Boore (1987).

The main difference between the new magnitude scale and the Hutton and Boore (1987) magnitude scale is that the new scale includes the station corrections. I have seen that IIEES uses horizontal components for calculating the magnitude of the events and I recommend them to add station correction to get better results.

7.3 Geometry of faults

I selected a data set consisting of 14 earthquakes with ML> 3.5 and I made the required observations such as polarities and amplitude ratios to determine the focal mechanisms for them, using FOCMEC and HASH programs. I also used Moment tensor inversion as the third method for calculating the focal mechanisms where full waveforms were used.

I compared the results of the three methods and I selected the solution that I thought that it is the best suggestion (Figure 6-7, Table 6-3).

The calculated focal mechanism shows normal, reverse and strike slip fault plane solutions in the area. This range of solutions could be because the solutions are not robust. To check the results I attempt to find the focal mechanisms of the selected data at Global CMT Catalog Search, but I did not find my data there; therefore I used focal mechanisms of the Rudbar earthquake aftershocks shown in Figure 2-3 and Ritz et al., 2006 to compare my results.

Ritz et al., 2006 suggest that the movement of the southern Caspian Sea also causes transtension in the internal domain in Alborz. This suggestion is based on observations of three main active left-lateral faults with normal component (Talegan,-eastern Mosha and Firozkuh faults), which are parallel to shear zone inside the central Alborz [*Ritz et al.*, 2006]; therefore it should not be surprising that some of my focal mechanisms have normal fault plane solutions in a transpressional regime. In fact I got a normal focal mechanism in the eastern part of the Mosha fault and one on the west part of Taleghan fault (Figure 6-7) which is consistent with Ritz et al., 2006 observations.

Focal mechanisms of the Rudbar earthquake aftershocks shown in Figure 2-3 show that earthquakes with reverse and strike slip fault plane solutions are normal in this area as some of my reverse and strike slip fault plane solutions.

My focal mechanism show different orientation of the T and P axes, but as Figure 7-1 shows this is not surprising in this area. Figure 7-1is obtained from Ritz et al., 2006. which different papers were used for plotting of this figure. This figure gives an idea about focal mechanisms of some events in this area.

I think that the reason that my focal mechanisms show different solutions in study area is that there is a complicated tectonic activity as a result of movement of the Central Iranian Block towards the South Caspian block and southwest movement of the South Caspian block relative to Iran. In addition the solutions are not robust because I did not get many solutions from moment tensor inversion with a good quality for the most earthquakes and results of FOCMEC and HASH programs depended on how many read polarities I had, how they were spreading and how many of those were showing upward movement or downward movements.

.

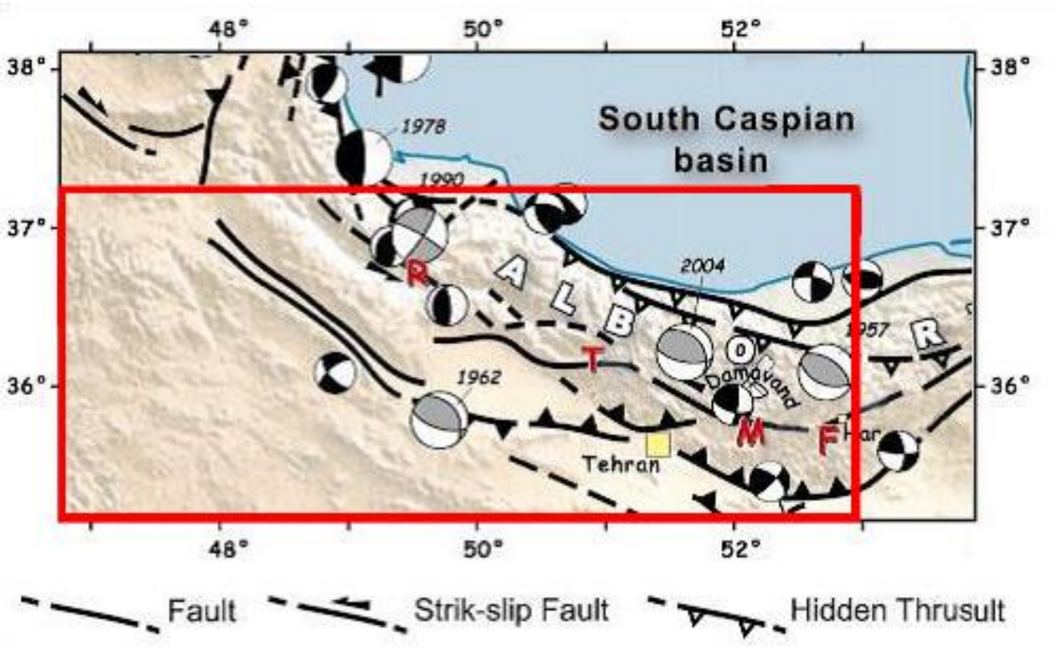

Figure 7-1: The South Caspian Sea and calculated focal mechanisms from different studies in my study area (shown in red)(modified from Ritz et al., 2006). R=Rudbar fault, T=Taleghan fault, M=Mosha fault and F=Firozkuh fault.

8 Conclusion

I got the following results from my data set:

- 1D velocity model 2 [Abbassi et al., 2010] which represents the Moho at a depth of 58±2 km describes structures in the Alborz Mountains better compared to other velocity models that were in use in single earthquake location method and the computed travel time-distance diagrams using this model is more consistent with my observations.

- I improved the three existing velocity models (1, 3 and 4). The new velocity models represent velocity of P-wave in a range between 7.52 and 7.93 km /s for the upper mantle and close to 6 km / s for the upper most crust. I should mention that the initial model 2 still works better when looking at residuals only compared to the new models when including also S-phases.

- Seismic activities along the Rudbar fault are located in an area between the Kabateh and Zard-Goli segments which was not ruptured during the Rudbar earthquake and at the eastern end of Rudbar fault. This means that Rudbar fault is an active left-lateral strike-slip fault and it may continue eastward in future.

- The amplitudes on horizontal components are 1.48 larger than amplitudes on vertical components in average. The calculated M_L scale using horizontal components and station correction gives better results compare to Hutton and Boore (1987) scale. However, the main difference comes from the inclusion of station corrections.

- Movement of the Central Iranian Block towards the South Caspian block and southwest movement of the South Caspian block relative to Iran cause a complicated tectonic activity in Alborz Mountains.

References

- Abbassi, A., A. Nasrabadi, M. Tatar, F. Yaminifard, M. Abbassi, D. Hatzfeld, and K. Priestley (2010), Crustal velocity structure in the southern edge of the Central Alborz (Iran), *Journal of Geodynamics*, *49*(2), 68-78.
- Allen, M., M. Ghassemi, M. Shahrabi, and M. Qorashi (2003), Accommodation of late Cenozoic oblique shortening in the Alborz range, northern Iran, *Journal of structural geology*, *25*(5), 659-672.
- Allen, M. B., S. J. Vincent, G. I. Alsop, A. Ismail-zadeh, and R. Flecker (2003), Late Cenozoic deformation in the South Caspian region: effects of a rigid basement block within a collision zone, *Tectonophysics*, *366*(3), 223-239.
- Aloisi, M., O. Cocina, G. Neri, B. Orecchio, and E. Privitera (2002), Seismic tomography of the crust underneath the Etna volcano, Sicily, *Physics of the Earth and Planetary Interiors*, *134*(3), 139-155.
- Ambraseys, N. N., and C. P. Melville (2005), *A history of Persian earthquakes*, Cambridge university press.
- Ashtari, M., D. Hatzfeld, and N. Kamalian (2005), Microseismicity in the region of Tehran, *Tectonophysics*, *395*(3), 193-208.
- Berberian, M., and R. Walker (2010), The Rudbār Mw 7.3 earthquake of 1990 June 20; seismotectonics, coseismic and geomorphic displacements, and historic earthquakes of the western ‘High-Alborz’, Iran, *Geophysical Journal International*, *182*(3), 1577-1602.
- De Martini, P., K. Hessami, D. Pantosti, G. D'Addezio, H. Alinaghi, and M. Ghafory-Ashtiani (1998), A geologic contribution to the evaluation of the seismic potential of the Kahrizak fault (Tehran, Iran), *Tectonophysics*, *287*(1), 187-199.
- Doloei, J., and R. Roberts (2003), Crust and uppermost mantle structure of Tehran region from analysis of teleseismic P-waveform receiver functions, *Tectonophysics*, *364*(3), 115-133.
- Dreger, D. (2002), Time-domain moment tensor INVerse code (TDMT_INVC) Version 1.1, *Berkeley Seismological Laboratory*, *18*.
- Guest, B., G. J. Axen, P. S. Lam, and J. Hassanzadeh (2006), Late Cenozoic shortening in the west-central Alborz Mountains, northern Iran, by combined conjugate strike-slip and thin-skinned deformation, *Geosphere*, *2*(1), 35-52.

- Hardebeck, J. L., and P. M. Shearer (2008), HASH: A FORTRAN Program for Computing Earthquake First-Motion Focal Mechanisms–v1. 2–January 31, 2008, edited.
- Havskov, J., and L. Ottemoller (2010), *Routine data processing in earthquake seismology*, Springer.
- Hutton, L., and D. M. Boore (1987), The ML scale in southern California, *Bulletin of the Seismological Society of America*, *77*(6), 2074-2094.
- Jackson, J., K. Priestley, M. Allen, and M. Berberian (2002), Active tectonics of the south Caspian basin, *Geophysical Journal International*, *148*(2), 214-245.
- Kissling, E. (1988), Geotomography with local earthquake data, *Reviews of Geophysics*, *26*(4), 659-698.
- Kissling, E., W. Ellsworth, D. Eberhart-Phillips, and U. Kradolfer (1994), Initial reference models in local earthquake tomography, *Journal of Geophysical Research: Solid Earth (1978–2012)*, *99*(B10), 19635-19646.
- Lienert, B. R., and J. Havskov (1995), A computer program for locating earthquakes both locally and globally, *Seismological Research Letters*, *66*(5), 26-36.
- Ottemöller, L., and S. Sargeant (2013), A local magnitude scale ML for the United Kingdom, *Bulletin of the Seismological Society of America*, *103*(5), 2884-2893.
- Ottemöller, L., P. Voss, and J. Havskov (2011), FOR WINDOWS, SOLARIS, LINUX and MACOSX.
- Radjaee, A., D. Rham, M. Mokhtari, M. Tatar, K. Priestley, and D. Hatzfeld (2010), Variation of Moho depth in the central part of the Alborz Mountains, northern Iran, *Geophysical Journal International*, *181*(1), 173-184.
- Reilinger, R., S. McClusky, P. Vernant, S. Lawrence, S. Ergintav, R. Cakmak, H. Ozener, F. Kadirov, I. Guliev, and R. Stepanyan (2006), GPS constraints on continental deformation in the Africa-Arabia-Eurasia continental collision zone and implications for the dynamics of plate interactions, *Journal of Geophysical Research: Solid Earth (1978–2012)*, *111*(B5).
- Richter, C. F. (1935), An instrumental earthquake magnitude scale, *Bull. Seism. Soc. Am*, *25*(1), 1-32.
- Ritz, J.-F., H. Nazari, A. Ghassemi, R. Salamati, A. Shafei, S. Solaymani, and P. Vernant (2006), Active transtension inside central Alborz: A new insight into northern Iran–southern Caspian geodynamics, *Geology*, *34*(6), 477-480.

- Sarkarinejad, K., and S. Ansari (2014), The Coulomb Stress Changes and Seismicity Rate due to the 1990 Mw 7.3 Rudbar Earthquake, *Bulletin of the Seismological Society of America*.
- Snieder, R., and J. Trampert (1999), *Inverse problems in geophysics*, Springer.
- Snoke, J. A. (2003), FOCMEC: focal mechanism determinations, edited, pp. 1629-1630, Academic Press, San Diego.
- Sodoudi, F., X. Yuan, R. Kind, B. Heit, and A. Sadidkhouy (2009), Evidence for a missing crustal root and a thin lithosphere beneath the Central Alborz by receiver function studies, *Geophysical Journal International*, *177*(2), 733-742.
- Stein, S., and M. Wysession (2009), *An introduction to seismology, earthquakes, and earth structure*, John Wiley & Sons.
- Um, J., and C. Thurber (1987), A fast algorithm for two-point seismic ray tracing, *Bulletin of the Seismological Society of America*, *77*(3), 972-986.
- Vernant, P., F. Nilforoushan, J. Chery, R. Bayer, Y. Djamour, F. Masson, H. Nankali, J.-F. Ritz, M. Sedighi, and F. Tavakoli (2004a), Deciphering oblique shortening of central Alborz in Iran using geodetic data, *Earth and Planetary Science Letters*, *223*(1), 177-185.
- Vernant, P., F. Nilforoushan, D. Hatzfeld, M. Abbassi, C. Vigny, F. Masson, H. Nankali, J. Martinod, A. Ashtiani, and R. Bayer (2004b), Present-day crustal deformation and plate kinematics in the Middle East constrained by GPS measurements in Iran and northern Oman, *Geophysical Journal International*, *157*(1), 381-398.
- Waldhauser, F. (2001), hypoDD--A program to compute double-difference hypocenter locations.
- Waldhauser, F., and W. L. Ellsworth (2000), A double-difference earthquake location algorithm: Method and application to the northern Hayward fault, California, *Bulletin of the Seismological Society of America*, *90*(6), 1353-1368.
- Waldhauser, F., and D. P. Schaff (2008), Large-scale relocation of two decades of Northern California seismicity using cross-correlation and double-difference methods, *Journal of Geophysical Research: Solid Earth (1978–2012)*, *113*(B8).
- Wolf, L. W. (2002), Looking Into the Earth, *Eos, Transactions American Geophysical Union*, *83*(33), 361-362.